Mechanical behavior of solid helium: Elasticity, plasticity, and defects

John Beamish*

Department of Physics, University of Alberta, Edmonton, Alberta T6G 2E1, Canada

Sébastien Balibar†

Laboratoire de Physique de l'École normale supérieure, ENS, Université PSL, CNRS, Sorbonne Université, Université Paris–Diderot, Sorbonne Paris Cité, 75231 Paris Cedex 05, France

(published 28 October 2020)

This review addresses experiments on elasticity, plasticity, and flow of solid ^{4}He and ^{3}He, focusing on dislocations and other defects that are responsible for the unusual mechanical behavior of such quantum crystals. Helium's zero point motion prevents it from freezing unless pressure is applied and makes the solid extremely compressible, with elastic constants orders of magnitude smaller than those of conventional solids. Tunneling allows defects to remain mobile at low temperatures, so dislocations have much larger effects on mechanical properties than in conventional solids. At temperatures below 400 mK, dislocations in hexagonal-close-packed (hcp) ^{4}He are essentially undamped and, in the absence of pinning by ^{3}He impurities, glide freely in the basal plane. In this regime, dislocation motion reduces the shear modulus by as much as 90%, an effect that has been referred to as "giant plasticity" although it is reversible and so might be better described as "softening." In this low temperature regime, macroscopic plastic deformation occurs via sudden dislocation avalanches with a wide range of time and length scales. At higher temperatures, dislocation motion is damped, introducing dissipation in elastic measurements, and thermally activated defect motion makes helium crystals extremely ductile, flowing under millibar stresses near melting. During the last decade, most of the properties of the dislocations that are responsible for the elastic effects described in this review have been accurately measured: their orientation, density, and length distributions, the nature of their networks, and their binding to isotopic impurities. Despite this detailed understanding of mobile dislocations, there remain open questions. Much less is known about defects' roles in the elastic and plastic behavior of hcp and bcc ^{3}He crystals and even in hcp ^{4}He, and almost nothing is known about other types of dislocations that are immobile and thus do not affect elastic properties. These might be responsible for recently observed superfluidlike mass flow in ^{4}He at low temperatures, although it is now clear that the apparent mass decoupling seen in torsional oscillator experiments with solid ^{4}He was due to the elastic effects described in this review, not to supersolidity.

DOI: 10.1103/RevModPhys.92.045002

CONTENTS

*jbeamish@ualberta.ca
†sebastien.balibar@lpa.ens.fr

I. INTRODUCTION

Helium is a uniquely quantum material. The most dramatic manifestation of its quantum nature is superfluidity in liquid helium. Atoms of the common isotope ^{4}He are bosons and condense into a superfluid state below the lambda temperature $T_\lambda = 2.176$ K. The rare isotope ^{3}He is a fermion and does not become superfluid until atoms pair at much lower temperatures, around 2 mK, to form complex superfluid phases. Quantum effects are usually less significant in solids. In classical crystals, at zero temperature atoms sit at lattice sites where the potential energy is minimized. Since they are localized, they can be regarded as distinguishable particles and quantum statistics are not important. In solid helium, quantum effects change this picture in two important ways. First, helium's small mass and weak interatomic potential means that atoms have large quantum zero point motion, rather than sitting motionless at lattice sites. Second, tunneling allows helium atoms to exchange, so their Bose or Fermi statistics remain relevant in this quantum solid.

The zero point energy due to localizing an atom within a lattice unit cell can be estimated by considering a point particle in a three-dimensional box. Its ground state energy is $E_0 = 3h^2/8ma^2$, where h is Planck's constant, m is the particle's mass, and a is the size of the box, i.e., the lattice parameter. A more realistic estimate for atoms with a hard core diameter d would be to use $a - d$ rather than a as the distance over which atoms are confined. This quantum mechanical energy is largest for light atoms like helium and can be compared to the potential energy of the solid, set by the depth ε of the interatomic potential well. The "quantumness" of a solid can then be characterized by the de Boer parameter Λ, whose square is essentially the ratio of the zero point energy to the potential energy

$$\Lambda^2 = \frac{h^2}{ma^2\varepsilon}. \tag{1}$$

Even for a weakly interacting inert gas like argon, the zero point energy is a small correction to the classical potential energy $\Lambda^2 \approx 0.03$. For solid ^{4}He, with its light mass and even weaker interactions $\Lambda^2 \approx 7$, so the quantum energy dominates. Neutron scattering measurements (Adams *et al.*, 2007) of solid ^{4}He atoms' zero point kinetic energy give values of around 25 K, substantially larger than the depth of the potential well for helium atoms $\varepsilon \approx 11$ K. Quantum effects are even more important in solid ^{3}He, which has the same potential but a smaller mass.

The solid, liquid, and vapor phases of materials are often displayed in pressure-temperature (P-T) phase diagrams like those in Fig. 1. Figure 1(a) shows the phase diagram for argon, a simple classical material with a spherically symmetric interatomic potential and a close-packed face-centered-cubic (fcc) crystal structure. The solid (red) coexistence line in Fig. 1(a) is the vapor pressure curve, where the liquid and gas phases coexist (or, below the melting point, it is the sublimation curve where solid and gas phases coexist). The vapor pressure curve ends at a critical point, above which argon is fluid but there is no distinction between liquid and gas states.

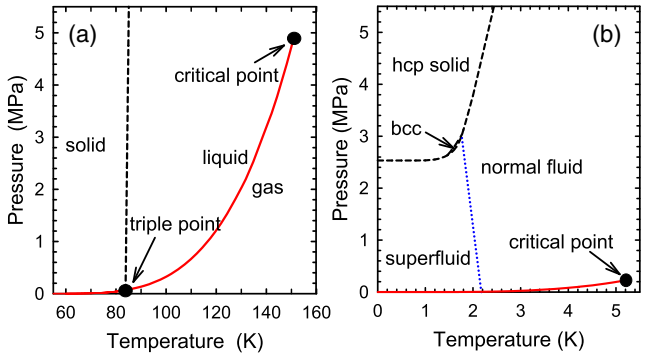

FIG. 1. Pressure-temperature (P-T) phase diagrams for (a) argon and (b) ^{4}He. Melting curves are shown as dashed black lines, and vapor pressure curves are shown as solid red lines. ^{4}He's superfluid transition (the "lambda line") is the dotted blue line.

The dashed (black) line separating the solid and fluid phases is the melting curve, which extends to high pressure with a positive slope (the melting temperature T_m increases slightly with pressure, the normal behavior for materials where the solid phase is denser than the liquid). These lines meet at the triple point, a unique point in the phase diagram where all three phases can coexist. These phases and transitions are familiar from other materials, e.g., water, ice, and steam. For water, the triple point occurs at a temperature T_c of 273.16 K (which was used as a fixed point to define the Kelvin scale temperature) and a pressure of 612 Pa. Water is, however, a complex material with many different solid phases. It is also unusual in that its solid phase, ice, is less dense than liquid water, which results in a melting curve with a negative slope.

The phase diagrams of nearly all materials share these features: coexistence lines between solid, liquid, and gas phases that meet at a triple point. The exception is helium, for which quantum effects dominate in the liquid and solid phases. Figure 1(b) shows the phase diagram of helium (for the common isotope ^{4}He). In contrast to argon, and to all other materials, there is no triple point at which solid, liquid, and gas can coexist. Helium is the only liquid that does not freeze under its own vapor pressure, a consequence of its large zero point energy and its weak interatomic interactions. ^{4}He can be solidified only by applying pressures greater than 2.53 MPa, with the melting curve shown as a dashed black line. At the lowest temperatures it crystallizes in the hcp structure, but there is a small region at around 1.6 K where a body-centered-cubic (bcc) phase, with a more open structure and lower zero point energy, is stable. Even higher pressures are required to solidify the lighter ^{3}He isotope (3.44 MPa at zero temperature), and its bcc phase extends to low temperatures. The solid and gas phases never coexist in helium, so the vapor pressure curve (the solid red line) extends to zero temperature. The existence of a quantum liquid at arbitrarily low temperatures creates the possibility of superfluidity in the Bose isotope ^{4}He. The superfluid state appears below the dotted blue lambda line in Fig. 1(b).

Helium's quantum nature affects its properties in the solid state. The density of low pressure helium crystals is less than half the value predicted for classical crystals with the same potential. Even at the lowest temperatures, helium atoms' zero

point motion extends over a significant fraction of the unit cell (Arms, Shah, and Simmons, 2003; Blackburn *et al.*, 2007), in contrast to classical crystals where thermal fluctuations are the only source of displacements away from lattice sites. Solid helium is also extremely compressible, with a bulk modulus less than a third of the value expected for a classical crystal and about 5 orders of magnitude smaller than that of a typical metal.

In addition to expanding the lattice and softening the crystal, helium's zero point motion allows atoms to exchange by tunneling. This exchange means that, in contrast to other materials, helium atoms' Bose or Fermi statistics remain important in the solid phase. In solid ^{3}He, for example, atomic exchange leads to magnetic ordering of spins at temperatures of around 1 mK. In both ^{3}He and ^{4}He, it allows isotopic impurities to move easily through the lattice, even at zero temperature. One intriguing possibility is that a quantum crystal could have a finite vacancy concentration at zero temperature, creating an "incommensurate solid" with perfect periodicity but fewer atoms than lattice sites. Delocalized "zero point vacancies" (ZPV) would contribute to mass flow and in ^{4}He could even Bose condense to form a "supersolid" with coexisting positional and superfluid order. At present there is no clear evidence for zero point vacancies, but even in their absence exchange could still produce a supersolid in which translational symmetry breaking and superfluidity coexist.

As well as revealing uniquely quantum phenomena in solids, helium has advantages as a model system to study material properties of solids. For example, at low temperatures helium's latent heat of melting disappears, so melting and freezing become purely mechanical processes. This allows the liquid-solid interface to be studied in detail, in contrast to conventional crystals where the latent heat makes it difficult to achieve equilibrium. Many of its unusual properties have been experimentally studied, including its surface tension (Balibar, Edwards, and Laroche, 1979; Keshishev, Parshin, and Babkin, 1979; Gallet, Wolf, and Balibar, 1984; Wolf *et al.*, 1985; Rolley *et al.*, 1989; Edwards, Mukherjee, and Pettersen, 1990; Andreeva and Keshishev, 1991; Babkin *et al.*, 1995; Wagner *et al.*, 1996; Tsepelin *et al.*, 2001), roughening transitions (Keshishev, Parshin, and Babkin, 1979; Landau *et al.*, 1980; Gallet, Wolf, and Balibar, 1984; Rolley, Balibar, and Gallet, 1986; Rolley *et al.*, 1989; Alles *et al.*, 2001; Todoshchenko *et al.*, 2005), melting and freezing waves (Keshishev, Parshin, and Babkin, 1981; Bodensohn, Nicolai, and Leiderer, 1986; Rolley, Guthmann *et al.*, 1995), and wetting behavior. Helium also provides unique opportunities to study fundamental properties of defects like impurities and dislocations, and their roles in elastic and plastic deformation (Balibar and Nozières, 1994; Balibar, Alles, and Parshin, 2005). Helium crystals of extraordinary purity can be prepared since at low temperatures all but isotopic impurities freeze out, and these have low concentrations. ^{3}He concentrations in commercial ^{4}He gas are of the order of 10^{-7} and can be reduced to the 10^{-12} level using a superfluid heat flush technique, or to essentially zero by freezing at extremely low temperatures. High quality single crystals can be grown quickly and their density can be varied over a substantial range with moderate pressures. The complete temperature range is accessible, from essentially zero up to the melting temperature.

In this review, we discuss the current state of understanding of defects in solid helium, particularly their effects on these quantum crystals' elastic and plastic properties. Many of the measurements that we describe were inspired by Kim and Chan's 2004 claim of the discovery of supersolidity in torsional oscillator measurements (Kim and Chan, 2004a, 2004b). These torsional oscillator effects are now understood as a manifestation of the unusual elastic behavior of solid ^{4}He (Day and Beamish, 2007b; Haziot *et al.*, 2013a) rather than as mass decoupling of a supersolid (Maris and Balibar, 2011; Beamish *et al.*, 2012; Maris, 2012; Reppy *et al.*, 2012). However, interest in solid helium's quantum and mechanical properties began much earlier, and many experiments were spurred by predictions of supersolidity and of unusual quantum motion of diffusion of vacancies and impurities (Andreev and Lifshits, 1969; Chester, 1970; Leggett, 1970).

Helium was discovered spectroscopically in the Sun in 1868 and subsequently found on Earth as a product of uranium ore in 1895. It was first liquefied in 1908, but it was not until 1926 that ^{4}He was frozen by applying pressures greater than 2.5 MPa (Keesom, 1942). The crystal structure (hcp) was determined by x-ray diffraction (Keesom and Taconis, 1938) in the same year that the superfluid nature of the He II phase of liquid ^{4}He was discovered. The rare isotope ^{3}He is a decay product of tritium and became available as a byproduct of thermonuclear weapons programs (Osborne, Weinstock, and Abraham, 1949). Osborne, Abraham, and Weinstock (1951) solidified ^{3}He and its bcc and hcp structures were identified by Schuch, Grilly, and Mills (1958). Phase separation of solid ^{3}He-^{4}He mixtures at low temperatures was observed in 1962 (Edwards, McWilliams, and Daunt, 1962).

Ultrasonic measurements on solid helium began with longitudinal waves in bcc ^{3}He (Abel, Anderson, and Wheatley, 1961) and in ^{4}He (Vignos and Fairbank, 1961). The latter measurements led to the discovery of the bcc phase of ^{4}He, which occupies a small region of its phase diagram. Shortly thereafter, transverse ultrasound was propagated in hcp and bcc ^{4}He (Lipschultz and Lee, 1965). During the first half of the 1970s, elastic constants were measured in oriented single crystals of hcp and bcc ^{4}He (Greywall, 1971, 1976) and of bcc ^{3}He (Greywall, 1975). The temperature dependences of sound speeds were measured soon thereafter (Wanner, Mueller, and Fairbank, 1973; Wanner and Mueller, 1974). In 1976, dislocations were identified as the source of low temperature anomalies in ultrasonic velocities (Wanner, Iwasa, and Wales, 1976). Between 1979 and 1983, more complete measurements of the ultrasonic velocity and attenuation were made in hcp ^{4}He (Iwasa, Araki, and Suzuki, 1979; Iwasa and Suzuki, 1980) and in bcc and hcp ^{3}He (Beamish and Franck, 1982, 1983; Iwasa and Suzuki, 1982). These results provided new information about the mobility and pinning of dislocations in solid helium. During the same period, there were a number of plastic deformation experiments on helium, revealing "metallurgical" phenomena like yield drops (Suzuki, 1973, 1977) and plastic flow, at stresses much lower than in conventional crystals (Sanders *et al.*, 1977, 1978).

The study of defects in helium was less active during the 1980s and 1990s, but work included direct x-ray diffraction measurements of vacancy energies and concentrations (Heald,

Baer, and Simmons, 1984; Fraass, Granfors, and Simmons, 1989; Simmons, 1994) and x-ray topography experiments that directly imaged dislocation arrays associated with low angle grain boundaries (Iwasa *et al.*, 1995). The liquid-solid surface tension and wetting behavior of helium were thoroughly studied (Balibar, Edwards, and Laroche, 1979; Balibar and Castaing, 1985). The nonwetting of many substrates by solid helium was shown to suppress freezing in porous materials, which raised the freezing pressure in the nanoscale pores of Vycor glass by more than 1 MPa (Beamish *et al.*, 1983; Adams *et al.*, 1987; Molz and Beamish, 1995).

In 2004, interest in solid ^{4}He was reinvigorated by the apparent discovery of supersolid helium, based on torsional oscillator (TO) measurements. The TO frequency increased below 200 mK, which was interpreted as evidence of a supersolid mass fraction decoupling from the oscillator, in analogy to the classic Andronikashivili experiment that measured the superfluid fraction of liquid ^{4}He (Andronikashivili, 1946). The frequency shifts for solid ^{4}He were suppressed at high oscillation amplitudes, which was taken as evidence of a superfluidlike critical velocity. Other features of the TO data were unexplained, but suggested defects were important. The transition was rounded rather than sharp and was accompanied by a dissipation peak. The amount of decoupling varied by orders of magnitude in different experiments and usually decreased when samples were annealed. The transition temperature was extremely sensitive to ^{3}He impurities, decreasing by a factor of more than 2 when the impurity concentration x_3 was reduced from 3×10^{-7} to 10^{-9}.

In 2007, low frequency measurements of polycrystalline ^{4}He's shear modulus μ showed similar behavior (Day and Beamish, 2007b). The shear modulus increased below 200 mK, with the same dependence on temperature, ^{3}He concentration, and amplitude as the TO frequency change. However, the shear modulus behavior had a natural explanation in terms of mobile dislocations, which softened the crystal at high temperature but were pinned by ^{3}He impurities low temperature. The amplitude dependence was explained as stress-induced breakaway from the weak ^{3}He pinning centers. It was clear that the torsional oscillator and shear modulus behaviors were closely related, but it was difficult to understand how the shear modulus changes would affect different torsional oscillators. In 2012, several papers addressed this question and it became clear that the stiffening of torsional oscillators, due to shear modulus changes in solid helium in the torsion rod (Beamish *et al.*, 2012) or in other parts of the oscillator (Maris, 2012; Reppy *et al.*, 2012), was sufficient to explain the observed TO frequency shifts. Since then, a number of the original TO experiments have been repeated in rigid oscillators designed to minimize the effects of the solid helium's shear modulus. The frequency shifts were essentially eliminated (Kim and Chan, 2012; Choi, Shin, and Kim, 2015), confirming that they were due to elastic changes in the helium, not signatures of mass decoupling in a supersolid.

However, the shear modulus changes themselves were dramatic and unexpected. Further measurements on single crystals showed that mobile dislocations could reduce the shear modulus of hcp ^{4}He's by as much as 90%, orders of magnitude larger than dislocation effects in conventional materials (Thompson and Holmes, 1959; Bauer and Gordon, 1962; Alers and Zimmerman, 1965). This effect was described as "giant plasticity." These experiments identified the mechanism in hcp ^{4}He as basal glide (Haziot *et al.*, 2013a), confirmed that thermal phonon scattering was the source of dislocation damping (Haziot, Fefferman, Beamish, and Balibar, 2013), identified a critical dislocation velocity related to the propagation velocity of ^{3}He impurities (Haziot, Fefferman, Souris *et al.*, 2013), and extracted the dislocation density and length distribution in ^{4}He crystals (Fefferman *et al.*, 2014). Measurements in polycrystalline hcp ^{3}He identified an additional dislocation damping mechanism associated with the ^{3}He spins (Cheng and Beamish, 2017). The effects of dislocations on the elastic behavior of these quantum solids are now well established.

Dislocations are also central to plasticity. Early plastic deformation experiments (Suzuki, 1973, 1977; Sanders *et al.*, 1977, 1978) were done at high temperatures, where thermal processes like vacancy diffusion control the flow behavior. Recent measurements (Cheng and Beamish, 2018b) at much lower temperatures showed a crossover, from thermally activated creep above 400 mK to sudden dislocation avalanches and acoustic emission at lower temperatures.

Other experiments have studied mass flow in response to pressure gradients across solid helium. At high temperatures, flow can occur via motion of vacancies or dislocations (Day and Beamish, 2007a; Suhel and Beamish, 2011; Lisunov *et al.*, 2014, 2015). This defect motion is thermally activated, so flow rates decrease rapidly at low temperatures. Inspired by the search for supersolidity, a number of experiments (Greywall, 1977b; Bonfait, Godfrin, and Castaing, 1989; Day and Beamish, 2006) looked unsuccessfully for evidence of superflow in hcp ^{4}He at low temperatures. More recently, however, a group of experiments revealed nonthermal flow that began around 0.6 K and extended to temperatures below 100 mK (Ray and Hallock, 2008; Vekhov, Mullin, and Hallock, 2014; Cheng and Beamish, 2016; Shin *et al.*, 2017; Hallock, 2019). This may be an example of superflow associated with dislocations, but the flow channels have not been unambiguously identified and some aspects of the experiments are not yet understood.

Our theoretical understanding of quantum solids has also developed in recent decades. Classical calculations, which worked well for heavy inert gas crystals (Beamish, 2001), greatly overestimated the values of solid helium's density, binding energy, and bulk modulus. In fact, the helium atoms sit at local maxima of the interatomic potential, where classical lattice dynamics predicts imaginary phonon frequencies. Early theories of solid helium (Werthamer, 1969; Klein and Horton, 1972; Glyde, 1976) incorporated quantum zero point motion but also had to recognize the correlations between atoms' positions due to their hard core repulsion, leading to effective potentials with renormalized force constants and sound speeds. Phonon dispersion curves were calculated and the normal, albeit slow, propagation of sound waves in solid helium was understood. Around the same time, it was realized that quantum exchange of atoms via tunneling

would have dramatic effects on point defects like vacancies and impurities, allowing them to propagate through a helium crystal, even at low temperatures (Andreev and Lifshits, 1969; Andreev, 1976). Exchange was also recognized as crucial to magnetic order in solid ^{3}He at mK temperatures.

The development of path integral Monte Carlo (PIMC) techniques, combined with advances in computational power, made it possible to do fully quantum mechanical, first principles simulations for condensed helium using accurate interatomic potentials (Ceperley, 1995). These directly confirmed the importance and consequences of quantum zero point motion and exchange in liquid and solid helium. Early PIMC work included computation of the Bose condensate and superfluid fractions, and the transition temperature in liquid ^{4}He (Ceperley and Pollock, 1986; Pollock and Ceperley, 1987). For solid helium, the atomic exchange constants for bcc ^{3}He were determined (Ceperley and Jacucci, 1987), giving nearest neighbor exchange frequencies of the order of 10 MHz and confirming that next nearest neighbor and multiple exchanges are also important. The calculated exchange frequencies for hcp ^{4}He were much smaller (Bernu and Ceperley, 2005), of the order of 100 kHz near the melting density. This is still significant but, given ^{4}He's lack of spin, there is no direct experimental confirmation of the values. More recent PIMC simulations involved defects in solid helium, including studies of vacancies and interstitials in hcp ^{4}He (Boninsegni *et al.*, 2006; Clark and Ceperley, 2008). Following the development of a new PIMC worm algorithm (Boninsegni, Prokofev, and Svistunov, 2006), simulations were expanded to larger particle numbers, allowing extended defects like grain boundaries (Pollet *et al.*, 2007) and dislocations (Boninsegni *et al.*, 2007) to be studied.

The properties of helium, including its solid phases, were comprehensively reviewed in the late 1960s by Wilks (1967) and Keller (1969). A more recent overview of ^{3}He was given by Dobbs (2000). Other reviews have focused on specific aspects of solid helium. These include theoretical and experimental aspects of exchange and the diffusion of defects (Guyer, Richardson, and Zane, 1971; Andreev, 1982; Grigorev, 1997), vacancies in ^{4}He (Burns and Goodkind, 1994), the surface of helium crystals Balibar, Alles, and Parshin (2005), and magnetic phases in ^{3}He (Bennemann and Ketterson, 1976; Osheroff, 1992; Adams, 2004). Two recent papers discussed aspects of plasticity (Beamish, 2019) and superflow (Hallock, 2019) in solid helium. This review focuses on the mechanical properties of solid helium, which have not been comprehensively described since the 1972 review by Trickey, Kirk, and Adams (1972), written at a time when ultrasonic measurements were just beginning and the effects of defects on helium's elastic and plastic behavior had not been explored.

II. STRUCTURE, PHASE DIAGRAMS, AND CRYSTAL GROWTH

The phase diagrams of ^{4}He and ^{3}He include multiple crystal structures at easily accessible pressures, and high quality single crystals can be rapidly grown at low temperatures. This provides unique opportunities to study defects and to distinguish between quantum and structural effects on their behavior. However, as for other materials, the quality of helium crystals depends on their preparation.

A. Phase diagrams

Helium does not freeze under its own vapor pressure, so its phase diagram has no triple point and the solid never coexists with low density gas. At zero temperature, a pressure of about 2.53 MPa (25.3 bar) is required to freeze ^{4}He. For ^{3}He, with its larger zero point motion, the minimum freezing pressure is 2.93 MPa (29.3 bar) at 315 mK, and an even higher pressure 3.44 MPa is needed at zero temperature. The melting pressures increase at higher temperatures. For example, at 2 K the melting curve pressures are about 38 bar for ^{4}He and 77 bar for ^{3}He. Figure 2 shows the *P-T* phase diagrams for ^{4}He (Vignos and Fairbank, 1961; Grilly and Mills, 1962; Straty and Adams, 1966a; Grilly, 1973; Hoffer *et al.*, 1976) and ^{3}He (Straty and Adams, 1966b; Grilly, 1971), at temperatures up to 4.2 K and pressures up to 20 MPa (200 bar). For both isotopes, there are stable bcc and hcp phases. The bcc region is small for ^{4}He (inset of Fig. 2), and at zero temperature solid ^{4}He is in the close-packed hcp phase. The larger zero point motion of ^{3}He favors the more open bcc phase, which occupies a much larger region extending down to zero temperature. Not shown in Fig. 2 are the close-packed fcc phases found in both ^{4}He and ^{3}He at much higher pressures and temperatures above 100 MPa and 15 K.

Figures 3 and 4 show the low pressure regions of the phase diagrams for ^{4}He and ^{3}He, respectively. The *P-T* diagrams (upper panels of the figures) show the melting curves separating liquid and solid, as well as the hcp-bcc coexistence line and the lambda line separating the normal (He I) and superfluid (He II) phases of ^{4}He. The lower panels show the corresponding molar volume versus temperature (*V-T*) diagrams, with the different phases and their coexistence regions.

The large compressibility of solid helium means that measurements are usually made at constant volume and density since the pressure cells in which the solid is grown are much more rigid than the helium. It also means that helium can be frozen at constant mole number since increasing the

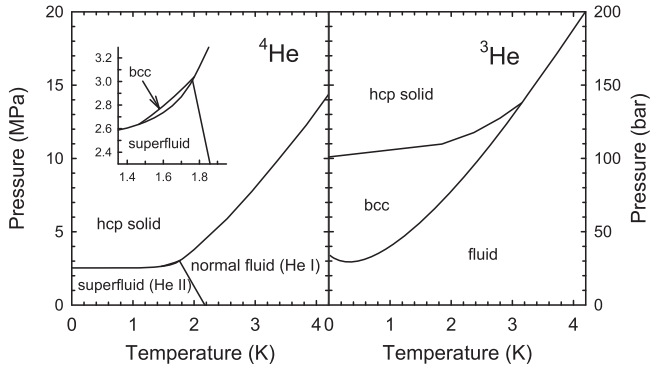

FIG. 2. *P-T* phase diagrams for ^{4}He (left panel) and ^{3}He (right panel). Inset: enlargement of the bcc region for ^{4}He. The pressure scales are the same for ^{3}He and ^{4}He but are labeled in MPa (on the left axis) and bar (on the right axis).

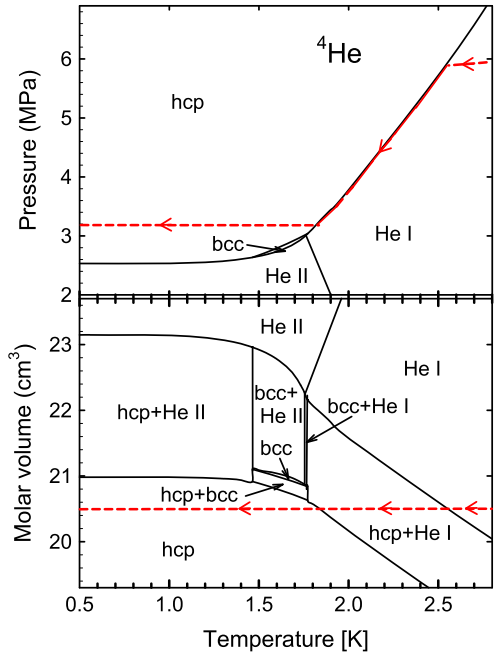

FIG. 3. *P-T* (upper panel) and *V-T* (lower panel) phase diagrams for ^{4}He. The dashed red lines and arrows indicate the path followed during blocked capillary freezing at a molar volume of 20.5 cm^3.

pressure by about 20 bar compresses the liquid to solid densities. If a cell containing high density liquid is cooled without adding or removing helium, e.g., by blocking the fill capillary, the liquid begins to freeze when the temperature reaches the melting curve. It then follows the melting curve

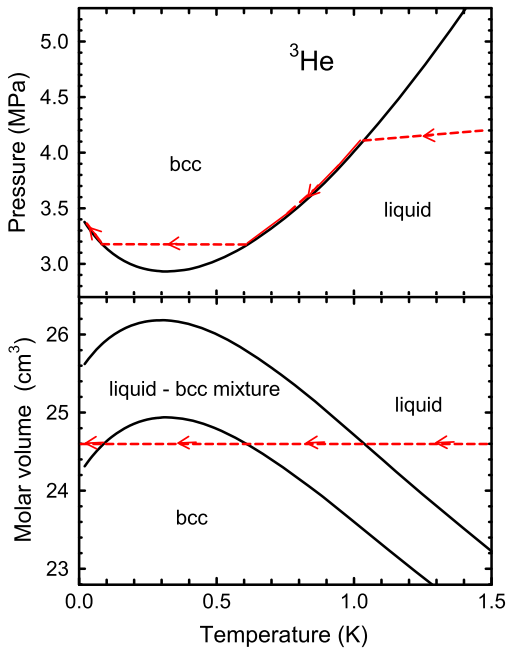

FIG. 4. *P-T* (upper panel) and *V-T* (lower panel) phase diagrams for ^{3}He. The dashed red lines and arrows indicate the path followed during blocked capillary freezing at a molar volume of 24.6 cm^3.

until all the helium is frozen at a lower pressure. The solid then cools at nearly constant pressure. Examples of such "blocked capillary" freezing paths are shown as horizontal (constant volume) dashed red lines in the lower *V-T* diagrams of Figs. 3 and 4. The upper panels show the corresponding *P-T* paths. Depending on the starting density, the system may pass through several phases and coexistence regions during cooling. For example, for a starting pressure of 5.1 MPa, the molar volume of liquid ^{4}He is 20.9 cm^3. At this density, the liquid begins to freeze into the hcp phase at around 2.35 K. Upon cooling, the liquid-hcp mixture transforms to a hcp-bcc mixture at the upper triple point of the bcc phase (1.772 K) and then follows the hcp-bcc coexistence curve until the bcc phase disappears at around 1.50 K. The hcp solid then cools at a nearly constant pressure of about 2.7 MPa. Samples at higher densities go directly from liquid to hcp, for example, the freezing path for a molar volume of 20.5 cm^3, shown as a dashed red curve in Fig. 3. At low densities (molar volumes larger than 21.0 cm^3, corresponding to starting pressures below 49 bar) ^{4}He remains partially liquid at low temperatures, and the solid portion transforms from hcp to bcc and then back to hcp again.

Helium crystals can also be grown at constant pressure by keeping the fill capillary open and adding helium as the liquid freezes. This corresponds to vertical paths in the *V-T* diagrams of Figs. 3 and 4. This method avoids hcp-bcc crystallographic transformations and the crystals experience much smaller stresses than during blocked capillary growth, where there are large pressure and temperature changes.

The minimum in the ^{3}He melting curve shown in Fig. 4 ($P_{\min} = 2.931$ MPa at $T_{\min} = 315$ mK) is due to ^{3}He's spin. Below 315 mK, the spin entropy of the solid is larger than the total entropy of the liquid. This unusual situation means that the slope of the melting curve is negative below 315 mK and low density ^{3}He crystals partially remelt when cooled at constant volume, as indicated by the dashed red lines in Fig. 4, which show a blocked capillary path at a molar volume of 24.6 cm^3.

B. Crystal growth and quality

Since the discovery of solid ^{4}He by Keesom (1942), helium has been solidified using different methods that produce either polycrystals or single crystals. The orientations of single crystals can be determined using diffraction or optical techniques. Keesom and Taconis (1938) were the first to apply x-ray diffraction to helium, using Laue diffraction to determine the crystal structure of hcp ^{4}He. As discussed by Greywall (1971), this technique has been used to find the orientation of crystals in some experiments, while others have used inelastic neutron scattering. Optical birefringence can also be used to orient hcp helium crystals, as shown by Heybey and Lee (1967). The facets that are visible during crystal growth provide a more general way to orient crystals if optical access is available.

For their study of sound propagation in hcp ^{4}He crystals, Crepeau *et al.* (1971) grew single crystals by filling a cell that was kept at constant temperature *T*. They observed that below 1.45 K this led to single crystals whose crystal orientations

they determined using optical birefringence. For his ultrasonic measurements of elastic constants, Greywall (1971) used a constant pressure growth method, which had been introduced by Shal'nikov (1962) and improved by Mezhov-Deglin (1966). Freezing slowly in a temperature gradient allowed Greywall to grow single crystals at various pressures P, and orientations were determined using Laue x-ray diffraction.

The blocked capillary method used to grow helium crystals at constant volume was shown by Sasaki, Caupin, and Balibar (2008) to produce polycrystals because many different crystallites nucleate on favorable sites on the cell walls. Growing crystals from the superfluid liquid at constant temperature, on the other hand, usually produces a single crystal, or a few large crystals, at or close to the liquid-solid equilibrium pressure. When grown below ~1 K, the crystals have facets with edges that can easily be analyzed to determine the crystal orientation (Sasaki, Caupin, and Balibar, 2008; Haziot *et al.*, 2013a).

1. Polycrystals

For low temperature measurements, the experimental cell is usually attached to the lowest temperature stage of a dilution refrigerator and the solid helium has to be grown from the liquid phase inside a closed cell. For blocked capillary growth, the first step is to admit helium through a thin capillary until the cell is filled with normal liquid ^{4}He at high pressure (greater than about 4.8 MPa). This is typically done at ~3 K to ensure that the helium is liquid everywhere along the fill line. To cool down, one usually starts by pumping on the refrigerator's ^{4}He pot, which rapidly cools to about 1 K. Since the fill capillary is thermally anchored to this "1 K pot," a plug of solid helium quickly forms there, isolating the mass of helium inside the cell from the external helium supply. Assuming that this plug does not move and blocks all flow of helium, the amount of helium in the cell is essentially constant when the cell is cooled and the helium freezes. If the fill line volume is negligible compared to the cell volume, freezing occurs along an isochore that first meets the melting curve at a temperature T_i and leaves it when the helium is completely frozen at a lower temperature T_f.

Figure 5 shows examples of optical images of ^{4}He crystals obtained by Sasaki, Caupin, and Balibar (2008) for various growth methods. The crystals were grown in an optical cell between two transparent glass windows closing an 11 × 11 mm hole through the body of the cell (3–10 mm thickness). The windows were sealed with indium O rings. The crystal shapes and the quality of the solid samples depended on the growth method. For example,Fig. 5(a) shows the result of rapid pressurization (over a time 140 ms in this example) of normal liquid helium (here at 1.8 K). This produces irregular "snowflakes" and a highly disordered solid.

Figure 6 shows blocked capillary growth paths on the P-T diagram of ^{4}He. The images in Figs. 5(b) and 5(c) correspond to slow crystallization (typically over 3 h) for path B of Fig. 6, starting with liquid at 5.1 MPa. When the cell reaches 2.36 K, freezing begins on the walls, which are colder than the center of the cell, producing the disordered hcp crystal visible in Fig. 5(b). The network of lines in the center part of the image corresponds to defects in a thin solid layer covering the front and back windows. At 1.77 K, the upper triple point of the bcc-hcp transition, the bcc phase appears between the hcp solid on the walls and the liquid in the center of the cell, as shown in Fig. 5(c). Here again the network of lines in the central part corresponds to grain boundaries in a thin layer covering the glass windows. Upon further cooling, the bcc region expands and the liquid region shrinks. The last liquid disappears at 1.66 K. The bcc region in the center then shrinks and disappears completely by 1.59 K, leaving only hcp solid. Note that this behavior differs slightly from that expected based on ^{4}He's V-T phase diagram (the lower panel of Fig. 3). The initial pressure (5.1 MPa) corresponds to a liquid molar volume of 20.9 cm^3. At this density, all of the liquid should freeze at a fixed temperature of 1.772 K since the three phases (liquid, bcc, and hcp) can coexist only at a triple point. Their coexistence over a range of temperatures (between 1.77 and 1.66 K) indicates that there are temperature and/or pressure gradients in the cell during blocked capillary growth.

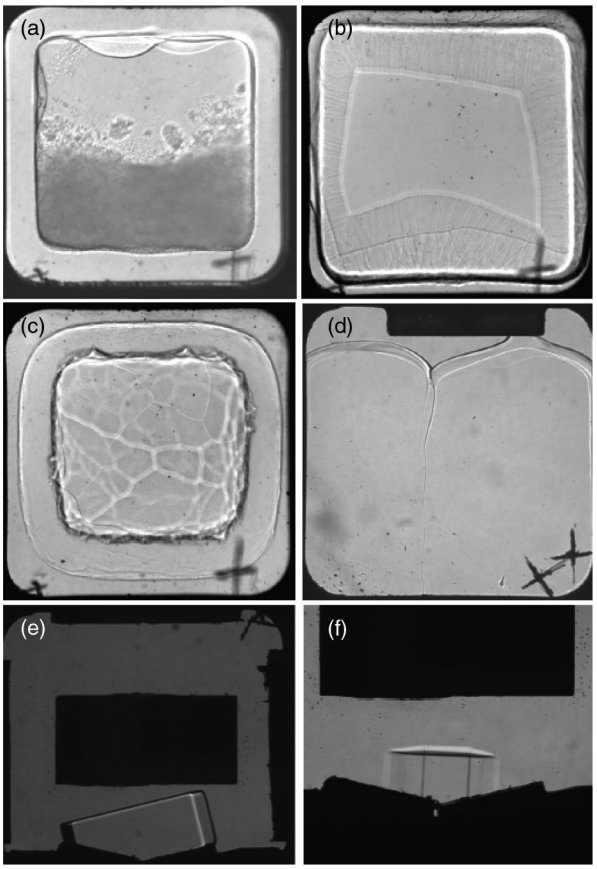

FIG. 5. Images of ^{4}He crystals, obtained in a transparent cell when using different growth methods. Crosses visible in the lower right corner of the images were carved on the windows to help adjust the focusing. From Sasaki, Caupin, and Balibar, 2008.

Solidification along the A or C isochores led to similar images. The highest pressure sample (path A) started with liquid at 6.2 MPa and began freezing at $T_i = 2.58$ K. Freezing was complete at $T_f \approx 1.95$ K, at a pressure of around 3.6 MPa in the hcp phase. According to Fig. 3, there should still be some liquid in the cell at 1.95 K, suggesting that additional helium has entered the cell despite the solid plug in the capillary. The lowest pressure sample (path C) starts at a pressure of 4.63 MPa and freezing into the hcp phase begins at

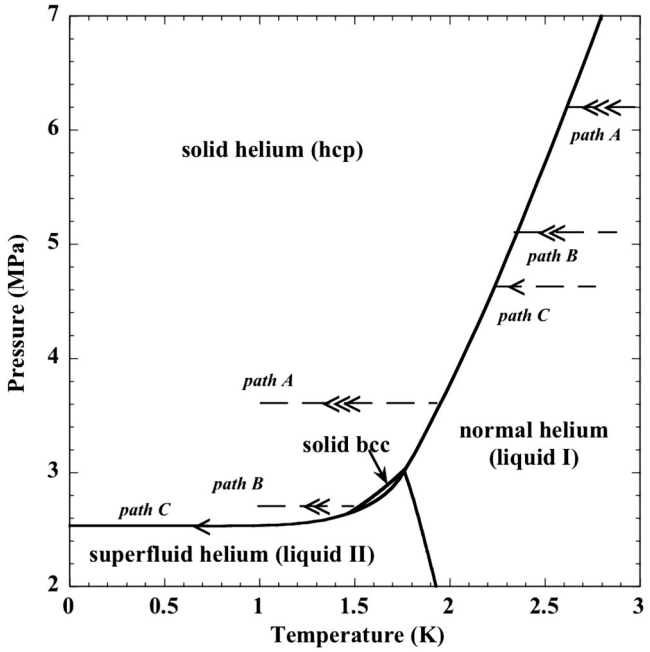

FIG. 6. Paths followed when ^{4}He is solidified using the blocked capillary method. The paths shown correspond to isochores for different starting pressures: path A (starting pressure 6.2 MPa), path B (5.1 MPa), and path C (4.63 MPa).

$T_i = 2.19$ K. As the sample cools along the melting curve, some hcp solid converts to bcc near the triple point, but the three phases again appear together until the hcp phase disappears at 1.70 K. On further cooling, the remaining liquid freezes, leaving only bcc solid by 1.56 K. At 1.46 K, the lower bcc-hcp triple point, the bcc solid suddenly converts to the denser hcp phase and some liquid reappears. The liquid region shrinks during further cooling along the melting curve, but some remains even at 35 mK.

In all three cases, solidification begins from the normal liquid and, in the absence of a controlled thermal gradient, it is difficult to obtain good quality single crystals. For paths A and B, the phase transitions between the hcp and bcc phases introduce additional stresses and disorder. To grow high quality single crystals such as those shown in Figs. 5(d)–5(f), a different growth method is required.

2. Single crystals

By pressurizing liquid ^{4}He at constant temperature in the superfluid phase, one can obtain single crystals (Pantalei *et al.*, 2010). This can be done by slowly injecting helium from an external source into a cell at a regulated temperature. The pressure in the cell rises until it reaches the crystallization pressure, where it remains until the cell is full of solid and the fill line spontaneously blocks. It is surprising that this can be done even at temperatures below 0.775 K, where there is a shallow minimum in the ^{4}He melting curve (Straty and Adams, 1966a; Grilly, 1973). One would expect the helium to crystallize in the fill line at that temperature, preventing more liquid from reaching the cell. However, helium remains in a metastable liquid state, crystallizing only at pressures about 10 mbar above the liquid-solid equilibrium curve (Grilly, 1973; Balibar, Castaing, and Laroche, 1980; Tsymbalenko, 1992; Ruutu *et al.*, 1996; Balibar, Mizusaki, and Sasaki, 2000; Pantalei *et al.*, 2010) so that crystallization begins in the cell, not in the fill line. If the capillary is large enough and the helium is injected sufficiently slowly, typically over a few hours, the pressure in the fill line does not increase enough to nucleate solid and it remains open until the helium in the cell is frozen.

Using this method, one usually obtains a single crystal in equilibrium with the superfluid liquid (Balibar, Alles, and Parshin, 2005). More than one crystal may nucleate on different favorable defects of the cell walls, but the largest crystal grows at the expense of the smaller ones due to the smaller curvature of its liquid-solid interface. Because the temperature inside a superfluid is homogeneous, gravity is relevant, and when this single crystal grows to a size larger than the capillary length $l_c \approx 1$ mm, it usually falls to the bottom of the cell. This fall may damage the crystal quality, but it can be melted down to a much smaller size and the crystal can then be regrown from the small seed crystal at the bottom of the cell. By regrowing the crystal slowly, the cell can be filled with a large high quality single crystal like those shown in Figs. 5(e) and 5(f). This procedure is possible only if the cell has optical access, so the crystal size can be controlled. Furthermore, the moving liquid-solid interface has a tendency to stick to defects on the walls, especially at points where a facet touches the wall. In this case, crystal growth proceeds by successive jumps, which creates defects.

Ruutu, Hakonen, and Babkin (1998) were able to grow freestanding single crystals with no screw dislocations. Their study showed the importance of screw dislocations in crystal growth, with drastic differences between the growth rates of faceted crystals with or without emerging screw dislocations. In an attempt to grow perfect crystals, Souris *et al.* (2015) grew crystals slowly in a carefully machined and polished cell with a completely open geometry. However, even at growth velocities as low as 270 nm/s, they found it impossible to grow crystals with fewer than 10^4 dislocations per cm^2. Their crystals, as well as those studied by Haziot, Fefferman, Beamish, and Balibar (2013) and Fefferman *et al.* (2014), typically had dislocation densities of the order of 10^5 to 10^6 per cm^2. However, those dislocation densities were determined from elastic measurements that are sensitive only to the samples' mobile edge dislocations, not screw dislocations like those measured by Ruutu, Hakonen, and Babkin (1998).

For many types of experiment it is important to realize that liquid regions can remain, even when a cell appears to be full of solid. A grain boundary can create a liquid channel, with a triangular cross section where it meets a wall. These are sometimes visible, as in Fig. 5(d) (Sasaki, Caupin, and Balibar, 2008), and provide channels for superfluid flow. The size of such channels decreases with increasing pressure, but some liquid remains as long as the pressure is within about 10 bar of the liquid-solid equilibrium pressure $P_{\rm eq}$. Liquid channels have also been seen at grain boundaries in high pressure fcc ^{4}He crystals growing on sapphire windows (Franck, Kornelsen, and Manuel, 1983). The image in Fig. 5(d) also shows that the solid phase does not wet the cell walls. The contact angle of the liquid-solid interface,

which is near 135°, depends on the wall material and shows hysteresis, as usual for rough walls (Sasaki, Caupin, and Balibar, 2008). A consequence of this nonwetting is that the solid phase does not enter corners nor fill narrow cavities or sharp grooves in the cell walls unless the pressure is significantly higher than P_{eq}. It can also allow a liquid layer to form between a helium crystal and the cell wall (Dash and Wettlaufer, 2005) at low pressures.

The previously described procedure produces nearly random crystal orientations, but it would be useful for many experiments if the orientation could be controlled. Two methods have been used to obtain oriented single crystals of helium. Both work if the temperature is low enough for the crystals to be faceted during growth (Balibar, Alles, and Parshin, 2005). When a faceted crystal falls to the bottom of a cell, it often has a flat shape, like a coin whose faces are perpendicular to the c axis of the crystal structure. In that case, it often lands on a c facet, i.e., on a hexagonal plane of the crystal. By trying this procedure a few times, one can obtain a crystal with its sixfold-symmetry axis (c axis) vertical, as was done by Rolley *et al.* (1994) for their study of the properties of stepped surfaces of helium crystals. To nucleate and force the first seed to fall down freely to the bottom of the cell, they used a local electric field on top, a method that was used by Keshishev, Parshin, and Babkin (1979) and Tsymbalenko (1995).

One can also grow oriented helium crystals by epitaxy on a graphite surface (Balibar, Castaing, and Laroche, 1980; Eckstein *et al.*, 1980; Ramesh *et al.*, 1984; Sasaki, Caupin, and Balibar, 2008). This can work if the graphite surface has been sufficiently well cleaned (Sasaki, Caupin, and Balibar, 2008), but it is not always successful. Figure 5(e) shows a faceted helium crystal that nucleates on the right side of the V-shaped graphite piece at the bottom of the cell, and that is consequently oriented parallel to it. Figure 5(f), however, shows a crystal that nucleates somewhere else in the same cell and, when it falls down, it is misoriented with respect to the graphite.

Even if crystal orientations cannot be controlled, direct optical observation of growth shapes allows the orientation to be determined rather easily. For refrigerators with optical access through sets of windows, temperatures are limited to about 10 mK due to the absorption of light and rf radiation from the outer world. To image crystals in the submillikelvin range, groups in Leiden (Wagner *et al.*, 1996) and Helsinki (Manninen *et al.*, 1992) used CCD cameras working at 65 K inside the refrigerator.

3. ^{3}He crystals

As with ^{4}He, it is possible to freeze ^{3}He using the blocked capillary method. However, the deep minimum in the ^{3}He melting curve at $T_{min} = 315$ mK means that low density ^{3}He crystals partially remelt when cooled at constant volume, as indicated by the dashed red lines in Fig. 4 for a molar volume of 24.6 cm^3. To ensure that ^{3}He is completely frozen at low temperatures, initial liquid pressures greater than about 4.5 MPa are required when using this technique. Growing ^{3}He crystals directly into the high pressure hcp phase (not shown in Fig. 4) requires starting pressures above 18 MPa.

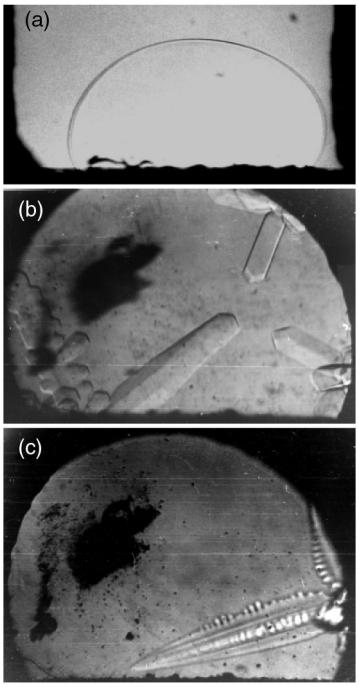

FIG. 7. ^{3}He crystal shapes obtained by Rolley, Balibar, and Gallet (1986) and Rolley, Balibar, and Graner (1994). (a) Equilibrium shape at $T = 320$ mK. (b) (110) facets on a growth shape of a bcc ^{3}He crystal at 70 mK. (c) Dendritic growth obtained with high growth rates (30 μm/s) at 100 mK.

The minimum in the melting curve also means that it is not possible to grow single crystals of ^{3}He by injecting mass through a fill line since the fill line blocks near T_{min}. Instead, one has to use a cell with a deformable membrane so that the liquid can be compressed. Using this method, Rolley, Balibar, and Gallet (1986) grew ^{3}He crystals at temperatures as low as 60 mK. Figure 7 shows images of these crystals coexisting with liquid ^{3}He. Figure 7(a) shows a crystal at the minimum of the melting curve minimum $T = 0.32$ K. This is above the roughening transitions in ^{3}He and the rounded equilibrium shape due to gravity and surface tension was analyzed by Rolley *et al.* to measure the surface tension of ^{3}He or, more precisely, the liquid-solid interfacial tension (Rolley *et al.*, 1989). During slow crystal growth at 70 mK, they also observed (110) facets of these crystals, shown in Fig. 7(b). At much lower temperature, additional facets were discovered by Wagner *et al.* (1996), Alles *et al.* (2001), and Tsepelin *et al.* (2002).

III. DEFECTS IN SOLID HELIUM

Some defects in solids can exist in thermal equilibrium; others are produced during crystal growth or by subsequent deformation. They can be classified as point defects (vacancies, interstitials, and impurities), one-dimensional defects (dislocations), or two-dimensional defects (grain boundaries and stacking faults). As in other materials, these defects affect many of the crystals' properties. In particular, dislocations and their interactions with other defects dominate the mechanical behavior of crystals. Quantum effects in helium crystals can

make defects highly mobile at low temperatures, which results in unique behavior.

A. Vacancies

Creating a vacancy corresponds to moving an atom from an interior lattice site to the crystal's surface. This increases the energy, entropy, and volume (or the pressure, in the case of solid helium, where the solid is held at constant volume). The equilibrium vacancy concentration at temperature T and pressure P is

$$x_v(T) = e^{s_v/k_B} e^{-[(E_v+Pv_v)/k_BT]}, \quad (2)$$

where E_v, v_v, and s_v are the vacancy formation energy, volume, and nonconfigurational entropy. The vacancy concentration increases with temperature and decreases under pressure. Since a crystal lattice is not perfectly rigid, neighboring atoms relax inward when an atom is removed and the vacancy formation volume v_v is smaller than the atomic volume v_a in a perfect crystal, typically $v_v \approx (0.5\text{–}0.7)v_a$ (Cai and Nix, 2016). In classical crystals, the formation energy, which reflects the energy of broken bonds with atoms adjacent to a vacancy, can be roughly estimated from the solid-liquid interfacial energy σ_{LS} (Balibar and Castaing, 1985; Andreeva, Keshishev, and Osip'yan, 1989; Edwards, Pettersen, and Baddar, 1991; Keshishev and Andreeva, 1991) and the surface area of the removed atom. The formation entropy, which is separate from the configurational entropy of the vacancy, is associated with local changes in vibrational frequencies and is of the order of k_B.

The most direct way to determine the vacancy formation energy is to measure the temperature dependence of x_v by comparing changes in the density of lattice sites (measured by x-ray diffraction) to changes in the density of atoms (from thermal expansion measurements). In the case of helium crystals confined in a rigid cell, the number of atoms and total volume are fixed, so the vacancy formation energy and entropy can be determined from the temperature dependence of the lattice parameters. The lattice parameter changes are substantial since vacancy concentrations in solid helium are as large as ~0.3% near melting. Such x-ray measurements have been made for the bcc and hcp phases of both ^{3}He and ^{4}He (Heald, Baer, and Simmons, 1983, 1984; Granfors, Fraass, and Simmons, 1987; Fraass, Granfors, and Simmons, 1989; Simmons, 1994). Formation energies in ^{3}He vary from 2.3 K for the bcc phase at low density (molar volume $V_m = 24.86$ cm^3, pressure $P = 2.98$ MPa) to 21.4 K in the hcp phase at $V_m = 18.8$ cm^3 ($P = 13.8$ MPa). For ^{4}He, measurements have been made over a narrower density range, with comparable formation energies, e.g., 9.6 K in the hcp phase at $V_m = 20.68$ cm^3 ($P = 3.14$ MPa). The bcc phase of ^{4}He exists only over a narrow temperature range, so the formation energy (~9 K) is less precise.

Vacancy formation energies can also be extracted from their effects on properties like the pressure or heat capacity, but this requires that the contributions of phonons or other thermal excitations are accurately known. An analysis of heat capacity data in bcc ^{3}He (Greywall, 1977c) gave vacancy energies similar to x-ray values. There is no clear evidence of a similar vacancy contribution to the specific heat of hcp ^{4}He, although it should be substantial (Gardner, Hoffer, and Phillips, 1973), perhaps reflecting a wide vacancy bandwidth with a small density of states at low energies (Fraass, Granfors, and Simmons, 1989).

The motion of vacancies also contributes to diffusion in helium crystals, dominating at high temperatures. NMR can be used to probe the motion of atoms with spin and has been used extensively to study diffusion of ^{3}He in helium crystals (Allen, Richards, and Schratter, 1982; Grigorev, 1997; Kim *et al.*, 2013). In solid ^{3}He, self-diffusion activation energies have been measured with NMR. They agree quite well with the direct x-ray values for vacancies in bcc ^{3}He but are significantly larger in hcp ^{3}He (Heald, Baer, and Simmons, 1984). The activation energy for vacancy diffusion can be larger than that for formation if vacancies have to overcome an energy barrier in order to move. The agreement between the two energies for bcc ^{3}He suggests that vacancies move by tunneling. The higher diffusion activation energy in hcp ^{3}He indicates that tunneling is less effective and that diffusion is largely due to classical activation over an energy barrier of about 12 K.

Since ^{4}He atoms do not have spin, NMR cannot be used to study self-diffusion in solid ^{4}He, but it can be used to study the diffusion of ^{3}He impurities in ^{4}He crystals. At high temperatures, the diffusion is thermally activated with activation energies similar to vacancy formation energies from x-ray measurements, although there is large scatter between activation energies from different NMR measurements (Fraass, Granfors, and Simmons, 1989).

Motion of vacancies can also be studied through the associated mass transport since moving a vacancy by one lattice site is equivalent to moving a helium atom the same distance in the opposite direction. Because of the pressure dependence of x_v in Eq. (2), a pressure gradient in a crystal produces a corresponding vacancy concentration gradient. Thermal vacancies diffuse from high to low concentration (low to high pressure), so mass flows in the opposite direction, reducing the pressure gradient. The deformation associated with such vacancy diffusion flow is, for example, a limiting factor in metals for high temperature turbine applications. For helium, vacancy diffusion flow has been shown to explain the frequency-dependent ultrasonic relaxation for solid ^{4}He confined in the nanoscale pores of Vycor glass, giving vacancy activation energies similar to other techniques (Beamish *et al.*, 1991). Recent experiments studied the pressure-induced flow of solid ^{3}He (Lisunov *et al.*, 2015, 2016) and ^{4}He (Lisunov *et al.*, 2014) along $6-8$ μm diameter channels through a 10 μm thick membrane. At high temperatures the flow is thermally activated with the activation energies of vacancies. Although vacancy diffusion can also relax pressure gradients in larger samples, diffusion time constants scale with the square of the sample dimensions. In macroscopic crystals, vacancy diffusion is an effective annealing mechanism only at temperatures close to melting. In addition, since vacancy activation energies increase with density, the vacancy concentration at a particular temperature decreases rapidly at high pressures and diffusion becomes much slower.

The quantum nature of helium crystals has important consequences for vacancies. The small energy barrier for exchange of a vacancy and a neighboring atom means that quantum tunneling is rapid, and vacancies can diffuse through helium crystals even at low temperatures. In the periodic lattice potential of ^{4}He crystals they can propagate as quasiparticles known as "vacancions" (Andreev and Lifshits, 1969; Burns and Goodkind, 1994; Grigorev, 1997). Vacancies in solid ^{3}He are also delocalized but, in contrast to ^{4}He, are not expected to propagate coherently. At temperatures above a few millikelvins, ^{3}He is in a paramagnetic state with disordered spins. Exchange of a vacancy and a ^{3}He atom changes the local spin configuration, so the lattice potential through which a vacancy moves is random, not periodic, and the vacancy motion is diffusive (Bernier and Hetherington, 1989).

Exchange in helium crystals gives vacancies a bandwidth that, if sufficiently large, creates an intriguing possibility that some vacancies in helium crystals could have negative energies. This would lead to a finite vacancy concentration at zero temperatures, i.e., an incommensurate solid with perfect periodicity but fewer atoms than lattice sites. In ^{4}He crystals, these ZPV propagate and contribute to mass flow. They could even Bose condense to form a "vacancy supersolid" with coexisting positional and superfluid order. This mechanism was initially suggested as an explanation of apparent mass decoupling seen in torsional oscillator measurements on solid ^{4}He (Kim and Chan, 2004a, 2004b), but it is now clear that the apparent mass decoupling was caused by the extraordinary elastic effects described later in this review, rather than being evidence of supersolidity (Beamish *et al.*, 2012; Maris, 2012; Reppy *et al.*, 2012). At present, there is no convincing experimental evidence for ZPV or for supersolidity in perfect crystals of ^{4}He. This conclusion is supported by PIMC simulations on hcp ^{4}He (Prokofev and Svistunov, 2005; Boninsegni *et al.*, 2006) that find a vacancy activation energy of 13 K, which is consistent with experimentally measured values. The vacancies cluster and phase separate at low temperatures, leaving a defect-free solid with no zero point vacancies or evidence of superfluidity. However, PIMC simulations suggest that the vacancy activation energy in ^{4}He may drop to zero in the presence of large strains (Pollet *et al.*, 2008), such as those near dislocations or grain boundaries.

B. Impurities

Because of the low temperatures at which helium crystals are studied, most impurities present in helium gas freeze to the walls, leaving only isotopic impurities (^{3}He impurities in ^{4}He or ^{4}He impurities in ^{3}He). These are chemically identical to the atoms of the host crystal but have different effective sizes. The lighter ^{3}He atoms occupy larger volumes in a ^{4}He lattice because of their greater zero point motion, while ^{4}He impurities are smaller than the host atoms in a ^{3}He crystal. The isotopic impurities sit at lattice sites as substitutional impurities since interstitials are high energy defects in helium (Boninsegni *et al.*, 2006).

Commercial helium gas has a ^{3}He concentration x_3 of about 10^{-7} (100 ppb). However, this varies from about 25 to 300 ppb, depending on the source of the gas (Oxburgh, O'Nions, and Hill, 1986; Souris *et al.*, 2014). Lower ^{3}He concentrations can be achieved by distillation (~1 ppb) or by a superfluid heat flush technique ($x_3 \lesssim 10^{-12}$) (Hendry and McClintock, 1987). It is, however, challenging to measure such low concentrations. This is most commonly done using dedicated helium mass spectrometers, which have resolution limits for x_3 of about 1 ppb (Amidon and Farley, 2010), although this can be extended to measure ^{3}He concentrations in the 10^{-12} range. Accelerator mass spectroscopy has been used for measurements at even lower concentrations, down to 10^{-14} (Mumm *et al.*, 2016). The rarer and more expensive isotope ^{3}He is harder to purify since distillation is not straightforward and the superfluid heat flush technique is not available. Impurity concentrations as low as $x_4 \approx 10^{-6}$ are possible, although not widely available.

Much purer ^{4}He crystals can be produced *in situ* if they are in contact with liquid ^{4}He at low temperatures since ^{3}He impurities are more tightly bound in the liquid. The difference in binding energies is 1.36 K (Edwards and Balibar, 1989), so the equilibrium ^{3}He concentrations are significantly different at the low temperatures of many experiments, e.g., a ratio greater than 10^{20} at 20 mK (Pantalei *et al.*, 2010). However, defects in the solid provide sites where ^{3}He impurities may be preferentially bound. Shear modulus measurements (Syshchenko, Day, and Beamish, 2010; Haziot, Fefferman, Souris *et al.*, 2013) on hcp ^{4}He show that edge dislocations are immobilized at low temperatures by ^{3}He impurities, which bind to them with an energy $E_B \approx 0.7$ K. Since this is smaller than ^{3}He's binding energy in liquid ^{4}He, ^{3}He impurities still migrate to the liquid at low temperatures, but the binding sites in the solid may make it difficult to achieve equilibrium between the ^{3}He concentrations in the solid and liquid. There may also be other locations in the crystal with even larger binding energies, e.g., nodes where dislocations meet or grain boundaries, so some ^{3}He may remain attached to defects at low temperatures. However, ^{4}He crystals can be grown from the superfluid at temperatures as low as 20 mK, where all the ^{3}He impurities remain in the liquid. This produces ^{4}He crystals containing essentially no ^{3}He (Pantalei *et al.*, 2010), although ^{3}He impurities do accumulate at the ^{4}He liquid-solid interface, with a binding energy estimated at 3 to 4 K (Wang and Agnolet, 1992; Treiner, 1993; Rolley, Balibar *et al.*, 1995).

At high temperatures, the motion of impurities is dominated by thermally activated vacancies since the barrier for vacancy-impurity exchange is small. However, direct exchange with host atoms allows impurities to move, even in the absence of vacancies. At low temperatures this quantum tunneling allows ^{3}He atoms to propagate as "impuritons" in the periodic ^{4}He lattice. These quasiparticles have a bandwidth zJ_{34} and group velocity $v_3 = zaJ_{34}$, where z is the number of nearest neighbors (12 for hcp crystals) and a is the atomic spacing. NMR measurements give a ^{3}He-^{4}He exchange frequency $J_{34}/2\pi \approx 0.8$ MHz (Kim *et al.*, 2013), which implies that ^{3}He atoms in solid ^{4}He are highly mobile at low temperature, with velocities of the order of cm/s. Their bandwidth $\Delta = zJ_{34}$

is ≈0.5 mK, so ^{3}He impuritons are narrow band quasiparticles. This bandwidth is much smaller than the potential wells or barriers produced by elastic strains around dislocations or other ^{3}He atoms, which results in large elastic scattering cross sections for such defects (Guyer, Richardson, and Zane, 1971; Andreev, 1982). The ballistic motion of ^{3}He impurities is limited by ^{3}He-^{3}He scattering, giving a mean free path inversely proportional to the ^{3}He concentration (Grigorev, 1997), of the order of 100 nm at the lowest concentrations studied $x_3 \approx 60$ ppm.

Less is known about the motion of ^{4}He impurities in solid ^{3}He since, being spinless, their diffusion cannot be studied directly with NMR techniques and, unlike vacancies, impurities do not contribute significantly to mass flow. The ^{4}He impurities must be delocalized, with exchange rates comparable to those of ^{3}He atoms in ^{4}He crystals, but, as for vacancies, spin disorder in solid ^{3}He prevents them from propagating coherently.

C. Dislocations

Dislocations are one-dimensional structural defects (Hull and Bacon, 2011) that can have edge or screw character, as illustrated in Fig. 8. The edge dislocation on the left is simplest to describe and can be thought of as the result of inserting a vertical half plane of atoms into the lattice. The bottom boundary of the half plane, the solid blue line in Fig. 8, is the edge dislocation. In the core region close to the dislocation the crystal is highly distorted, but far away the lattice deformations are small and can be described by linear elasticity. A dislocation is characterized by its Burgers vector $\vec{b}$, the lattice vector defined by the gap in a path that makes a circuit around the dislocation that would close in a perfect crystal. For an edge dislocation, the Burgers vector (shown as a short black line above the diagram) is perpendicular to the dislocation line and to the added half plane that created it, i.e., horizontal in Fig. 8. A screw dislocation, illustrated on the right in Fig. 8, can be thought of as the result of cutting a slit partway through a crystal and shifting the atoms on one side in the direction parallel to the border of the slit. For a screw dislocation, the Burgers vector (the short black line below the diagram) is parallel to the dislocation line (the edge of the slit, i.e., the solid blue line near the center of the diagram).

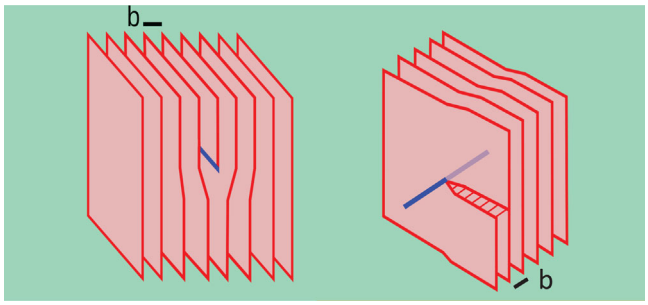

FIG. 8. Deformations around edge (left) and screw (right) dislocations. The dislocations are the lines near the centers of each diagram (shown in blue). The short black lines at the top (bottom) of the left (right) diagrams are their corresponding Burgers vectors **b**.

If a shear stress σ is applied to a crystal containing a dislocation, the dislocation experiences a force proportional to the stress and can move via a process known as glide. An edge dislocation moves in the glide plane defined by the dislocation line and its Burgers vector. If the dislocation moves horizontally through a crystal, the top half of the crystal is displaced with respect to the bottom half over the slipped region, by an amount equal to the Burgers vector. This is illustrated in the left panel of Fig. 9. The dislocation shear strain $\epsilon_{\rm dis}$ adds to the elastic strain $\epsilon_{\rm el}$ that the shear stress would produce in a perfect crystal, increasing the total strain ϵ and therefore reducing the solid's effective shear modulus $\mu = \sigma/\epsilon$. Since glide involves only local rearrangements of atoms near the core of a dislocation, plastic deformation can occur at much smaller stresses than would be needed to displace the entire plane of atoms in a perfect crystal.

The energy of a dislocation depends on its position, so it moves in a "Peierls potential" with the periodicity of the lattice (Friedel, 1964; Suzuki, Takeuchi, and Yoshinaga, 2013). The height of the energy barrier between neighboring minima is the Peierls energy per unit length E_P, and the minimum stress required to move a dislocation over this barrier is the Peierls stress $\sigma_P = (2\pi/b^2)E_P$. The Peierls stress depends on the crystal structure and the glide direction and is usually smallest for glide in close-packed crystal directions. It also depends on the detailed structure of the dislocation core, decreasing exponentially with increasing dislocation width (Hull and Bacon, 2011), and is difficult to calculate accurately, although there are general trends. In hcp and fcc materials, the dominant glide directions are usually in the close-packed planes. This leads to anisotropic slip behavior in hcp crystals where the slip occurs in the basal plane. General plastic deformations require slip in multiple directions, so the stress at which they begin may be controlled by the largest Peierls barrier, not by the easy slip direction.

For dislocations that lie along crystallographic directions, the previously described glide corresponds to moving the entire dislocation line from its low energy configuration along a lattice direction, over the Peierls barrier to the next lattice row. In fact, dislocations are not usually perfectly aligned with a lattice direction, which introduces "grown-in" or "geometric" kinks, i.e., locations at which the dislocation line crosses between neighboring minima of the Peierls potential, as illustrated in the left diagram of Fig. 9. If such a kink moves along the full length of the dislocation, the entire line is displaced by one lattice constant. The one-dimensional periodic potential seen by a kink moving along the dislocation is generally smaller than the Peierls potential for moving an entire dislocation line, so glide may proceed by motion of kinks along dislocations. Even in the absence of geometric kinks, kink-antikink pairs can be thermally excited at high temperature, and dislocations can glide when these pairs separate and the kinks and antikinks move in different directions along the dislocation. In a quantum solid like helium, it is possible that these pairs could be created by tunneling, which would effectively eliminate the Peierls barrier and delocalize the dislocation.

In a hcp crystal, the primitive unit cell has a basis of two atoms. A perfect edge dislocation in the basal plane

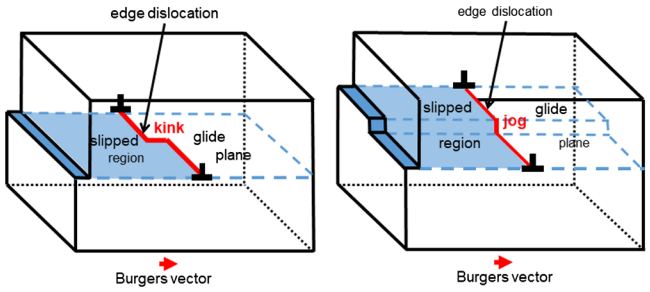

FIG. 9. Kinks (left panel) and jogs (right panel) on edge dislocations. An edge dislocation (the solid red line) corresponds to the edge of a vertical half plane inserted into the lattice. Its Burgers vector, indicated by the red arrow at the bottom of each diagram, is perpendicular to the dislocation line. The dislocation line and its Burgers vector define the horizontal glide plane, outlined by the dashed blue lines. The shaded regions of the glide plane are the portions of the crystal where slip has occurred. The kink (left panel) is a horizontal step in the dislocation line, in the direction of the Burgers vector. The jog (right panel) is a vertical step in the dislocation line, perpendicular to the Burgers vector.

corresponds to inserting the vertical planes corresponding to both sets of atoms and has a Burgers vector b equal to the lattice spacing in the basal plane. Inserting a single plane involves less lattice distortion, but the corresponding displacement is not a lattice vector of the hcp crystal. Instead it creates a "partial dislocation" with a Burgers vector $b_p = b/\sqrt{3}$ at an angle $\pm 30°$ with respect to the perfect dislocation. The perfect dislocation could split into two such partials that, being of the same sign, repel each other elastically. Since the elastic energy of a dislocation is proportional to the square of its Burgers vector, splitting into two widely separated partials lowers the total elastic energy by a third. However, this creates a stacking fault in the two-dimensional region between the two partial dislocations (Hull and Bacon, 2011). The energy of this stacking fault is proportional to its area, i.e., to the separation D between the partials, so there is an attractive force between them. The balance between these forces determines the equilibrium separation D of the partials, roughly proportional to $\mu a^2/\gamma$, where γ is the stacking fault energy per unit area. For the edge dislocation that glides in the basal plane of the hcp crystals, the stacking fault corresponds to a layer of fcc structure. The hcp and fcc structures have the same number of nearest neighbors and similar energies, so γ is small and this dislocation is expected to split into widely separated partials. In hcp crystals there are no stable stacking faults in other directions, so edge dislocations with, for example, Burgers vectors along the c axis do not split into partials.

In addition to glide, which does not require mass transport within the crystal, an edge dislocation can move in a direction perpendicular to its Burgers vector (vertically in Fig. 8) via a process known as climb. This involves adding or removing atoms at the edge of the inserted half plane and thus requires mass flow to or from the dislocation. At high temperatures this can occur via diffusion of thermal vacancies. Dislocations do not climb as a straight line but instead form vertical jogs, as shown in the right-hand diagram of Fig. 9. The jogs move along the dislocation when atoms are removed, allowing the dislocation to climb vertically. Jogs are essentially short sections of dislocations with a perpendicular orientation. If, as often happens, the Peierls stress in that direction is large, jogs may pin the dislocations and prevent them from gliding.

For an edge dislocation like that shown in Fig. 8, the lattice is compressed above the dislocation and expanded below it. For screw dislocations, there is no compression, only shear distortions. Within the cores of dislocations, atomic displacements are large and depend on details of interatomic interactions, but at distances larger than a few lattice constants the deformations can be described as elastic strain fields. The energy per unit dislocation length associated with this elastic field can be computed by integrating the strain energy from the radius r_0 of the dislocation core region to a cutoff distance R that is roughly the separation between dislocations (Hirth and Lothe, 1982; Hull and Bacon, 2011), giving

$$E_{\text{edge}} = \frac{\mu b^2}{4\pi(1-\nu)} \ln \frac{R}{r_0}, \qquad E_{\text{screw}} = \frac{\mu b^2}{4\pi} \ln \frac{R}{r_0} \tag{3}$$

for edge and screw dislocations, where μ and ν are the crystal's shear modulus and Poisson ratio (the crystal is assumed to be elastically isotropic). The dislocation's total energy includes the core energy, which is difficult to estimate but is usually small compared to the elastic energy.

Dislocations cannot simply end within a crystal, but two dislocations can join to form a third dislocation as long as the total Burgers vector is preserved. Dislocations form a network of connected dislocations, characterized by the dislocation density Λ (total length of dislocations per unit volume) and the average distance between nodes, known as the network length L_N. These parameters are not independent: when the dislocation density is high, the probability of intersecting is larger and the network length is smaller. If dislocations form a perfect cubic network of intersecting dislocations, they are related by $\Lambda L^2 = 3$. Networks in real crystals are disordered, of course, with a distribution of network lengths. In addition, if dislocations are somehow aligned to avoid crossing, e.g., parallel dislocations in a low angle grain boundary or nonintersecting 2D networks, then ΛL^2 can be much larger, as we later see for helium.

Defects like dislocations and impurities interact elastically through their strain fields. For example, two parallel dislocations of the same sign (Burgers vectors in the same direction) repel each other, while dislocations of opposite sign attract. Similarly, an impurity with a radius $(1+\delta)r_a$ that is larger than r_a of the host atoms (e.g., a ^{3}He atom in a ^{4}He crystal) is attracted to the expanded region on one side of an edge dislocation. A smaller impurity (e.g., a ^{4}He atom in a ^{3}He crystal) is attracted to the opposite side, where the lattice is compressed. The binding energy can be estimated as $E_B \sim \mu\delta v_a$, where δ is the misfit parameter and μ is the solid's shear modulus. The small value of μ for helium results in small estimates of binding energies for isotopic impurities, e.g., $E_B \sim 0.6$ K for hcp ^{4}He (Iwasa and Suzuki, 1980), similar to the binding energy inferred from elastic measurements $\sim 0.7 \pm 0.1$ K (Syshchenko, Day, and Beamish, 2010; Fefferman *et al.*, 2014). Using PIMC techniques, Corboz *et al.*

(2008) computed a binding energy of 0.8 K for a ^{3}He atom on a screw dislocation in hcp ^{4}He, but this has not been experimentally confirmed. The calculations require modifications of standard PIMC techniques, and the origin of impurity binding is not obvious since there are only shear deformations around screw dislocations.

An impurity bound to a dislocation acts as a pinning center since impurities normally can move through the lattice only via diffusion. However, individual impurities are relatively weak pinning centers and dislocations break away from them at large stresses, leaving only the much stronger network pinning at nodes where dislocations meet. The impurity pinning length is inversely proportional to the concentration of impurities bound to the dislocation $x_i^{\rm dis} = x_i e^{E_B/k_B T}$, and in contrast to conventional solids where impurity motion freezes out during cooling, impurities in helium remain mobile at low temperature, so the dislocation and bulk impurity concentrations can quickly reach equilibrium. At low temperatures, $x_i^{\rm dis}$ can be much larger than the bulk impurity concentration x_{i0}, by a factor of more than 10^8 at 50 mK for $E_B = 1$ K. When $L_i = a/x_i^{\rm dis}$ becomes comparable to the network length L_N, impurity pinning reduces the dislocations' mobility. At lower temperatures, impurities can saturate dislocation lines ($L_i \sim a$), completely immobilizing them.

The effects of gliding dislocations on a solid's elastic behavior were analyzed by Granato and Lücke (1956) to interpret measurements of ultrasonic velocities and attenuation in metals. They treated dislocations as mobile strings of length L, the distance between pinning points. The elastic energy per unit length in Eq. (3) acts as a line tension C. When a stress is applied to the crystal, a dislocation loop experiences a force per unit length $F = \sigma b$, where σ is the component of the shear stress in the dislocation's glide plane, in the direction of its Burgers vector. It moves in response to this force, bowing out between pinning points. For a static stress, the average displacement (Granato and Lücke, 1956) of the dislocation is $\xi_0 = (16b/\pi^5 C)\sigma L^2$. Over the area swept out by the dislocation line $\xi_0 L$, the crystal has slipped a distance b. The strain produced by a density Λ of dislocations of length L is $\epsilon_{\rm dis} = \Lambda b \xi_0$. The total strain is the sum of this dislocation strain and the elastic strain $\epsilon_{\rm el}$ that would occur in a dislocation-free crystal. The resulting shear modulus $\mu = \sigma/(\epsilon_{\rm el} + \epsilon_{\rm dis})$ is reduced from its intrinsic value in a perfect crystal $\mu_0 = \sigma/\epsilon_{\rm el}$, i.e., dislocation motion softens the crystal. Its shear modulus is reduced by a factor proportional to ΛL^2, so a few long dislocations can have the same effect as many short ones.

To extend this model to the high frequencies used in ultrasonic measurements, the inertia and damping of dislocations had to be considered. A dislocation gliding through a crystal at speed v_d carries with it a strain field that accelerates nearby atoms, giving the dislocation an effective mass per unit length $\pi\rho b^2$. The moving dislocation is damped by the scattering of thermal phonons or other excitations, which gives a resistive force (per unit length) proportional to its velocity $F_d = -Bv_d$. Phonon scattering from a dislocation's static strain field gives a damping $B \propto T^5$. However, the absorption and reemission of phonons by mobile dislocations is a more effective scattering mechanism at low temperatures. The damping coefficient for this "fluttering" mechanism has been calculated (Ninomiya, 1974) as

$$B = \frac{14.4 k_B^3}{\pi^3 \hbar^2 c^3} T^3, \tag{4}$$

where c is the Debye sound speed of the solid.

The Granato-Lücke equation of motion for the displacement $\xi(x,t)$ at time t and position x along a dislocation line driven by a stress $\sigma(t)$ is

$$A\ddot{\xi} + B\dot{\xi} - C\frac{\partial^2 \xi}{\partial x^2} = b\sigma, \tag{5}$$

where $A = \pi\rho b^2$ is the effective mass and C is the line tension from Eq. (3). In acoustic applications, the stress is periodic $\sigma_0 e^{i\omega t}$. For small damping, e.g., at low temperatures, a dislocation loop of length L has a sharp resonance at an angular frequency

$$\omega_0 = 2\pi f_0 = \sqrt{\frac{2}{1-\nu}}\frac{v_t}{L}, \tag{6}$$

where $v_t = \sqrt{\mu/\rho}$ is the shear sound speed in the solid. For a 10 μm long dislocation in solid ^{4}He, this occurs at $f_0 \sim 10$ MHz. At acoustic frequencies well below f_0, the dislocation motion and associated strain $\epsilon_{\rm dis}$ are in phase with the applied stress, so the shear modulus is reduced from its purely elastic value. At frequencies above f_0, the dislocation's inertia dominates and the dislocation strain is out of phase with the applied stress, increasing the shear modulus. If the crossover frequency can be measured, the loop length between pinning points can be determined.

Of course, the Granato-Lücke model of dislocations contains a number of assumptions. It assumes that the dislocations move freely like strings, i.e., that they are not affected by the lattice Peierls potential. This is plausible for dislocations with easy glide directions, e.g., in the basal plane of hcp crystals. It assumes that pinning points are static, but ^{3}He impurities are highly mobile in solid ^{4}He and may not be effective pinning centers. It also oversimplifies a number of aspects of the dislocations' response to stresses. Some are easily fixed, e.g., by including an orientation factor R to account for the component of the applied stress in the dislocation's glide plane. Others are more complicated, e.g., writing the dislocation's properties in terms of the crystal's elastic constants C_{ij} rather than using a shear modulus and Poisson ratio for an isotropic medium. However, the effects of including elastic anisotropy are modest compared to other approximations in the model.

An important limitation when using this model to extract dislocation densities from ultrasonic or acoustic data is that dislocation loops in real crystals are not all the same length. Although it may be reasonable to assume an exponential distribution of lengths L_i for random impurity pinning, the dislocation network itself is disordered, with an unknown distribution of network lengths L_N. Integrating over an assumed distribution of loop lengths affects the calculated dislocation densities, particularly in the case of short loops

that contribute little to elastic properties. It is important to remember that not all dislocations are mobile, e.g., edge or screw dislocations in glide planes with large Peierls barriers do not respond to small shear stresses and will not be detected in acoustic measurements.

D. Grain boundaries and stacking faults

As shown in Fig. 5, freezing can nucleate at more than one location, producing multiple helium crystals with different orientations. Samples grown by rapid injection or using the blocked capillary technique have smaller crystallites and more grain boundaries. These grain boundaries can affect a solid's mechanical behavior, for example, by acting as sources and sinks for dislocations and vacancies. They may also include disordered or liquidlike layers where superflow could occur in solid ^{4}He samples, as suggested by PIMC studies that identified some grain boundaries in ^{4}He as superfluid (Pollet *et al.*, 2007). Close to the melting curve, thicker superfluid films can appear at grain boundaries and superfluid channels appear where three grain boundaries meet, or where grain boundaries meet a wall (Franck, Kornelsen, and Manuel, 1983; Sasaki, Caupin, and Balibar, 2007).

When crystals with similar orientations meet, the resulting grain boundary is essentially an array of edge dislocations with spacing inversely proportional to the angle between the crystals. Such low angle grain boundaries can be detected via the line broadening ("mosaic spread") they produce in diffraction measurements. Synchrotron x-ray measurements on hcp ^{4}He crystals grown at constant pressure (Burns *et al.*, 2008) showed single crystals of centimeter dimensions, although faster freezing produced multiple crystals with sizes of a few millimeters. However, the mosaic angle (typically about 6.5×10^{-4} rad) within these large crystals indicated that they contained low angle grain boundaries corresponding to arrays of dislocations separated by about $1500b$. At high temperatures (above $0.7T_m$), these boundaries were not fixed. Their motion appeared to be driven by stress gradients and increased with temperature. Earlier neutron diffraction experiments (Pelleg *et al.*, 2006) showed a similar motion of low angle boundaries in bcc ^{4}He, but not in the hcp phase. Subboundaries have been directly imaged in x-ray topography imaging studies on ^{4}He single crystals (Iwasa *et al.*, 1987, 1995; Iwasa, 2002), although individual dislocations could not be resolved.

Another type of two-dimensional defect can be produced during crystal growth or by vacancies and dislocations. A stacking fault (Hull and Bacon, 2011) occurs where the sequence of atomic planes of a perfect crystal is disrupted. For example, a fcc crystal is made up of close-packed planes arranged in an *ABCABCABC* order, while a hcp crystal consists of the same close-packed atomic planes alternating in the order *ABABABAB*. If the regular sequence is disrupted, for example, a crystal with stacking sequence *ABABCBCB*, two hcp regions are separated by a stacking fault that is essentially a layer of fcc structure. The hcp and fcc structures have the same coordination number and configuration of nearest neighbors. They differ only in the arrangement of atoms at larger distances, so their energies are similar.

In helium, the hcp-fcc energy difference and the corresponding stacking fault energy per unit area γ are extremely small. For ^{4}He, γ can be roughly estimated using the measured latent heat for the hcp-fcc transition at 113 MPa (Franck, 1980), which gives a value of about $\gamma \approx 10^{-5}$ J/m^2. However, γ is expected to be much smaller at pressures of around 2.5 MPa, where most measurements on solid ^{4}He have been made and stacking fault energies $\gamma \sim 2 \times 10^{-6}$ J/m^2 were computed by Borda, Cai, and Koning (2016) using PIMC methods. Stacking fault energies are much larger in conventional materials, typically around 0.1 J/m^2, and even for an inert gas crystal like krypton (Keyse and Venables, 1985) they are about 3 orders of magnitude larger than in solid helium.

Stacking faults can be created during thermal quenching, when vacancies condense and create voids that then collapse, leaving prismatic dislocation loops. They are also created when a perfect dislocation separates into two partial dislocations. Whether or not a particular dislocation splits, and the spacing D between the partials, depends on the stacking fault energy. The small value of γ leads to large splitting of edge dislocations in the basal plane of hcp ^{4}He. Borda, Cai, and Koning (2016) estimated an elastic splitting of about 43 nm, i.e., more than $100b$. Their PIMC simulations confirmed that these dislocations are split by at least $11b$, a lower limit set by the size of the simulation box.

IV. ELASTIC PROPERTIES OF SOLID ^{4}He AND ^{3}He

A. Sound modes and elastic constants C_{ij}

Inert gases interact via weak, spherically symmetric van der Waals potentials and form simple crystal structures at low temperatures, making them an attractive testing ground for calculations of elastic properties. Classical lattice dynamics gives a good description of the heaviest gases, but the behavior of helium is dominated by quantum effects. Nonetheless, sound propagates normally in solid helium crystals and their elastic constants are determined from ultrasonic and inelastic neutron scattering measurements of sound speeds.

Single crystals are anisotropic and their full set of elastic constants is needed to calculate sound speeds and polarizations in different crystallographic directions. When appropriately averaged, these give the shear and bulk moduli for polycrystalline samples (Maris and Balibar, 2010). Elastic constants have been measured near the melting temperatures for all three crystallographic phases of ^{4}He (bcc, hcp, and fcc), but only for the bcc phase of ^{3}He. Cubic crystals (e.g., bcc and fcc) have three independent elastic constants (C_{11}, C_{12}, and C_{44}). Under hydrostatic pressure they compress isotropically, with a bulk modulus $B = (1/3)(C_{11} + 2C_{12})$. Hexagonal crystals (e.g., hcp) have five independent elastic constants (C_{11}, C_{12}, C_{13}, C_{33}, and C_{44}). Their elastic properties are isotropic about the c axis, but under hydrostatic pressure the strain parallel to the c axis can differ from that in perpendicular directions, so the expression for the bulk modulus is more complicated. However, in hcp ^{4}He the c/a ratio, which is close to the 1.633 value for ideal close packing, is known to be essentially independent of pressure (Franck and Wanner, 1970). This implies that $C_{11} + 2C_{12} \approx C_{33} + 2C_{13}$, which gives a

TABLE I. Elastic constants of solid helium in its various crystallographic phases: bcc (top panel), fcc (middle panel), and hcp (lower panel). The first three columns give the isotope (^{4}He or ^{3}He), the molar volume, and the pressure. For the bcc and fcc phases, the other columns give the three elastic constants of cubic crystals, the bulk modulus B, and the anisotropy A. For the hcp phases they give the five hexagonal crystal elastic constants. Data are from ultrasonic velocity measurements (Crepeau *et al.*, 1971; Greywall, 1971, 1975, 1976, 1977a) or, for pressures above 20 MPa, from inelastic neutron scattering measurements (Reese *et al.*, 1971; Eckert, Thomlinson, and Shirane, 1978; Thomlinson, Eckert, and Shirane, 1978). The hcp ^{3}He elastic constants in square brackets are calculated values (Schoffel and Muser, 2001) since there have been no experimental measurements for the hexagonal ^{3}He phase.

Isotope (bcc)	V_m (cm^3)	P (MPa)	C_{11} (MPa)	C_{12} (MPa)	C_{44} (MPa)	B (MPa)	A
^{4}He	21.00	2.8	31.1 ± .7	28.1 ± .6	21.7 ± .2	29.1 ± .6	14 ± 6
^{3}He	24.45	3.3	20.16 ± .2	16.73 ± .4	9.29 ± .1	18.0 ± .3	5.3 ± 1
^{3}He	21.66	6.5	38.0 ± .5	34.5 ± .8	19.8 ± .3	35.9 ± .7	11 ± 4

Isotope (fcc)	V_m (cm^3)	P (MPa)	C_{11} (GPa)	C_{12} (GPa)	C_{44} (GPa)	B (GPa)	A
^{4}He	9.97	292	1.56 ± .07	1.06 ± .07	0.79 ± .02	1.23 ± .07	3.2 ± 1
^{4}He	9.43	380	2.17 ± .02	1.62 ± .03	1.00 ± .02	1.80 ± .03	3.6 ± 0.4
^{4}He	9.03	453	3.13 ± .23	2.24 ± .23	1.19 ± .05	2.54 ± .23	2.7 ± 1.5

Isotope (hcp)	V_m (cm^3)	P (MPa)	C_{11} (MPa)	C_{33} (MPa)	C_{12} (MPa)	C_{13} (MPa)	C_{44} (MPa)
^{4}He	20.97	2.6	40.5 ± .4	55.4 ± 2	21.2 ± .4	10.5 ± 1	12.4 ± .2.2
^{4}He	20.55	3.2	46.6 ± .2	60.4 ± 4	26.1 ± .4	⋯	⋯
^{4}He	20.32	3.6	55 ± 2	71 ± 3	29 ± 1	13.1 ± 1	14.0 ± 1
^{4}He	19.5	5.3	64.1 ± 4	87.3 ± 6	34.9 ± .3	⋯	⋯
^{4}He	19.28	5.8	76 ± 3	98 ± 4	42 ± 2	19.8 ± 1	19.6 ± 1
^{4}He	16.00	21.4	170 ± 30	240 ± 20	95 ± 20	⋯	50 ± 10
^{4}He	11.61	160	1130 ± 70	1260 ± 40	⋯	⋯	240 ± 10
^{4}He	9.41	370	2820 ± 80	3200 ± 60	⋯	⋯	5660 ± 10
^{3}He	18.77	15.0	[135 ± 14]	[156 ± 16]	[43 ± 4]	[39 ± 4]	[36 ± 4]

simplified expression for hcp ^{4}He's bulk modulus $B \approx (1/3)(C_{33} + 2C_{13})$.

Table I gives measured values of the elastic constants of solid helium. In ^{4}He, the bcc phase exists only over a narrow range around a molar volume of 21.0 cm^3. This corresponds to the pressure 2.8 MPa at which its bcc elastic constants are listed in Table I (Greywall, 1976). The ultrasonic measurements (Greywall, 1971, 1977a) for hcp ^{4}He extend over a molar volume range from 20.97 to 19.28 cm^3/mol (pressures from 2.6 to 5.8 MPa). Recent quantum mechanical calculations of the zero temperature elastic constants of hcp ^{4}He (Cazorla, Lutsyshyn, and Boronat, 2012; Pessoa, de Koning, and Vitiello, 2012) are in good agreement with the experimental values. Inelastic neutron scattering measurements (Reese *et al.*, 1971; Eckert, Thomlinson, and Shirane, 1977, 1978; Thomlinson, Eckert, and Shirane, 1978) also provided some information on elastic constants of hcp ^{4}He at pressures of up to 370 MPa (molar volume 9.41 cm^3) and of fcc ^{4}He at a pressure of 493 MPa (molar volume 9.03 cm^3).

The bcc phase is stable over a wider range in ^{3}He from 24.9 to 18.9 cm^3/mol (pressures from 2.93 to 13.7 MPa) and extends to zero temperature. Its elastic constants are measured at densities between 21.66 and 24.45 cm^3/mol (Greywall, 1975). The elastic constants of hcp ^{3}He are not measured, but Table I includes calculated values for a molar volume of 18.77 cm^3/mol, computed using path integral techniques (Schoffel and Muser, 2001). These hcp elastic constants are expected to be quite accurate since the corresponding elastic constants computed for the bcc phase of ^{3}He agree well with experimental values.

The ultrasonically determined elastic constants in Table I were measured near the crystals' melting points. The neutron scattering measurements are made at temperatures between 4.2 and 10 K (for hcp ^{4}He) and between 19 and 22 K (for fcc ^{4}He). At pressures below 20 MPa, the variations of the elastic constants with temperature are smaller than their experimental uncertainties. For the highest pressure fcc ^{4}He sample, with a melting temperature of 38.5 K, the elastic constants decrease by more than 10% at the melting point.

At low pressures, solid helium has extremely small elastic constants, for example, a bulk modulus that is about 35 and 140 times smaller than those of neon and xenon, respectively (Beamish, 2001). Although some of this difference is attributable to helium's weak interatomic attraction, much of it is the result of its large zero point motion. This expands solid helium's lattice and makes it about 25 times more compressible than a classical crystal with the same interatomic potential. Its large compressibility means that applying the maximum pressure shown in Table I (453 MPa) changes ^{4}He's density by a factor of 2.3, which increases its elastic constants by a factor of 100. Helium's small elastic constants also mean that sound propagates slowly, at speeds as low as 75 m/s for transverse waves at low pressures.

Figures 10 and 11 show the density dependences of the elastic constants of the bcc and hcp phases of helium. The shear elastic constants C_{44} of bcc ^{3}He and ^{4}He fall on a common curve, in contrast to C_{11}, C_{12}, and the bulk modulus $B = (1/3)(C_{11} + 2C_{12})$, which are significantly lower for ^{4}He. This is not surprising since the zero point energy is larger for ^{3}He, which increases its pressure and bulk modulus compared to ^{4}He at the same density. Zero point motion also

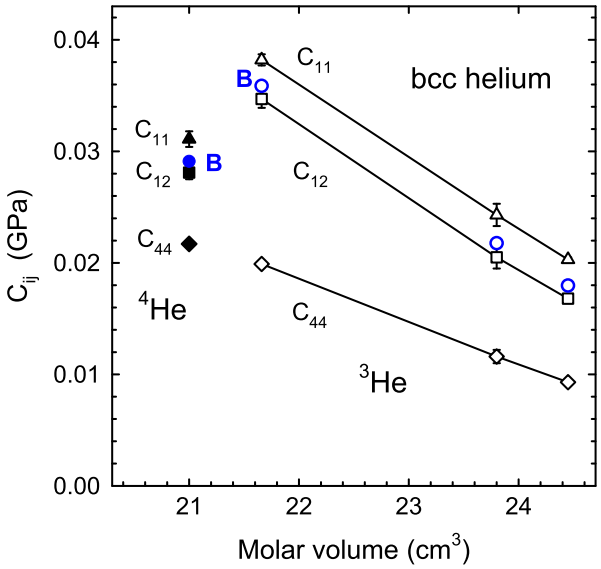

FIG. 10. Elastic constants and bulk modulus of bcc helium from ultrasonic measurements (Greywall, 1971, 1975, 1976). C_{44} (diamonds), C_{12} (squares), C_{11} (triangles), and bulk modulus B (circles) for bcc ^{3}He (open symbols) and ^{4}He (solid symbols at left).

affects helium's elastic constants in other ways. Compared to crystals of the other inert gases (which have the fcc structure), the anisotropy parameter $A = 2C_{44}/(C_{11} - C_{12})$ is unusually large for bcc helium (Beamish, 2001). This results in ultrasonic beam deviations as large as 60° and consequent difficulties in observing the transverse modes in some crystallographic directions (Wanner, 1971). In bcc and fcc crystals, where atoms sit at centers of inversion symmetry, the elastic constants should obey the Cauchy relation $C_{12} - P = C_{44} + P$, where P is the pressure, provided that thermal and quantum motion can be neglected. Despite the importance of zero point motion in helium, this relationship holds as well in bcc and fcc helium as in the fcc crystals of the heavier inert gases (Beamish, 2001).

In hcp crystals, atoms do not sit at centers of inversion symmetry, so there are no equivalent Cauchy relations. The empirical relation $C_{11} + 2C_{12} \approx C_{33} + 2C_{13}$, which follows from the constant c/a ratio of hcp ^{4}He, holds within the uncertainty of the measurements, so the bulk modulus is accurately given by $B \approx (1/3)(C_{33} + 2C_{13})$. This bulk modulus is plotted in Fig. 11 as circles.

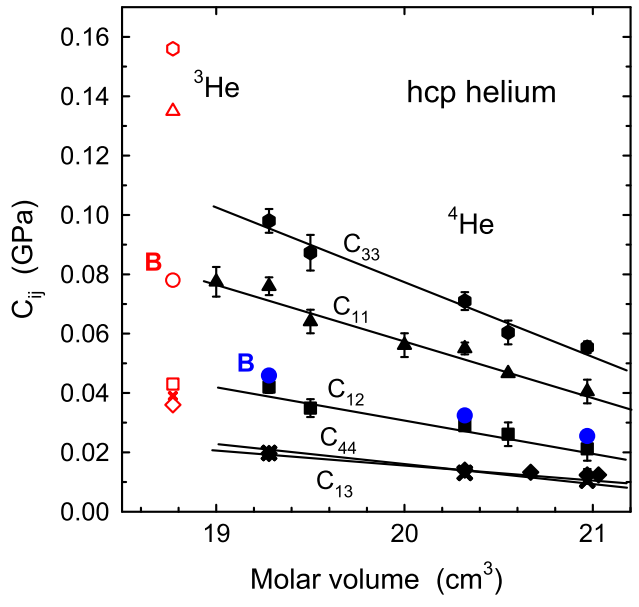

FIG. 11. Elastic constants and bulk modulus of hcp ^{4}He (solid symbols) from ultrasonic measurements (Crepeau *et al.*, 1971; Greywall, 1971, 1977a), and of hcp ^{3}He (open symbols) from path integral simulations (Schoffel and Muser, 2001). C_{44}, diamonds; C_{12}, squares; C_{11}, triangles; C_{13}, crosses; C_{33}, hexagons; bulk modulus B, circles.

B. Intrinsic temperature dependence

Even in defect-free crystals, elastic constants and dissipation depend on temperature because of the anharmonicity of the lattice. The anharmonicity is also responsible for thermal expansion or, in the case of helium crystals that are confined in a rigid cell at constant volume, the temperature dependence of the pressure. This intrinsic temperature dependence is related to $u(T)$, the crystal's internal thermal energy per unit volume, by a Gruneisen equation $P(T) = P_0 + \gamma u(T)$. The Gruneisen constant γ is often nearly independent of temperature so that at low temperatures the thermodynamic pressure increase in a dielectric crystal due to thermal phonons is proportional to T^4. The elastic constants C_{ij} have a similar temperature dependence (McGreer and Franck, 1990)

$$C_{ij}(T) = C_{0ij} - \Gamma_{ij} u(T), \tag{7}$$

where Γ_{ij} are related to the crystal's generalized Gruneisen constants. Elastic constants and sound speeds are therefore expected to decrease as the temperature increases, by amounts proportional to u. The Debye temperatures of helium crystals are much higher than their melting temperatures (Trickey, Kirk, and Adams, 1972), so the decreases are expected to be roughly proportional to T^4.

Figure 12 shows the transverse mode elastic constant $\hat{C}_0 = \rho v_t^2$ that McGreer and Franck (1990) calculated from ultrasonic measurements of the speed v_t of 3 MHz shear waves in single crystals of hcp ^{4}He. This crystal was grown at high pressure (15 MPa) and the measurements were made between 7 and 15 K. As expected, the decrease in this elastic constant was linearly related to the crystal's total thermal energy $u(T)$.

A T^4 variation of sound speeds is also seen in helium crystals at lower pressures, at temperatures near melting. However, as described in Sec. IV.C, dislocations in helium become mobile and make additional contributions to the sound speeds at low temperatures. These dislocations can be pinned by impurities, immobilizing them and restoring the crystal's intrinsic temperature dependence. The expected frequency-independent T^4 variation was seen in longitudinal sound velocity measurements on hcp ^{4}He crystals containing 1% of ^{3}He impurities (Iwasa and Suzuki, 1980). The top panel of Fig. 13 shows data at 10, 30, and 50 MHz; the solid lines are the expected T^4 dependence. Similar behavior has been seen

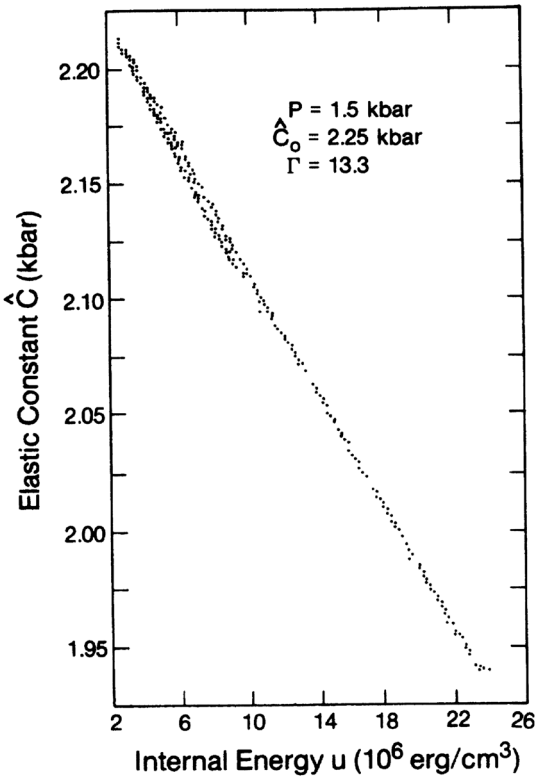

FIG. 12. Effective elastic constant $\hat{C}_0$ for transverse ultrasound in hcp ^{4}He at high pressure (15 MPa) vs total internal energy u. From McGreer and Franck, 1990.

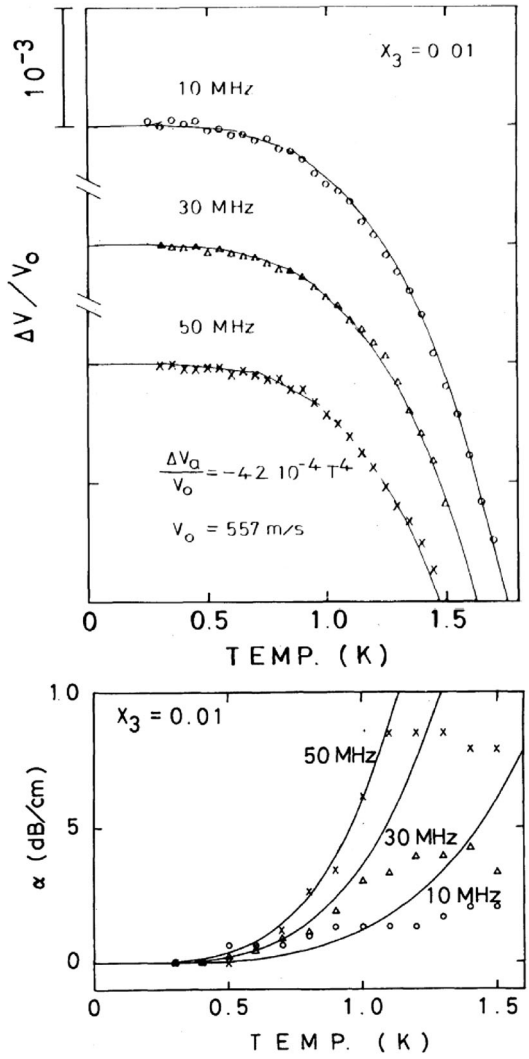

FIG. 13. Longitudinal sound velocity (upper panel) and attenuation (lower panel) in a hcp ^{4}He single crystal containing 1% of ^{3}He (Iwasa and Suzuki, 1980). The sound frequencies are 10 (circles), 30 (triangles), and 50 MHz (crosses). Solid lines are fits of the velocity data to the expected thermal phonon dependence $V_0 - AT^4$ and of the attenuation to the ωT^4 dependence expected for "zero sound" at low temperature (Maris, 1971).

in ^{3}He crystals (Beamish and Franck, 1983). Figure 14 shows the variation of the longitudinal sound speed in a hcp ^{3}He crystal containing 0.5% ^{4}He, with the expected dependence due to thermal phonons.

Note that the intrinsic sound velocity changes in the hcp crystals of Figs. 13 and 14 are small, corresponding to elastic constant decreases of less than 1% at the melting temperature. In low density bcc ^{3}He crystals, the changes are even smaller but include contributions from thermally excited vacancies as well as phonons (Iwasa and Suzuki, 1982). The 12% changes in the high pressure ^{4}He crystal of Fig. 12 reflect the much higher temperatures in those measurements. The maximum temperature in the measurements of Fig. 12 correspond to about 15% of the crystal's Debye temperature $\Theta \approx 100$ K (Trickey, Kirk, and Adams, 1972). This can be compared to the maximum temperatures in Figs. 13 and 14, which are only about 6% of the crystals' Debye temperatures (around 30 and 40 K, respectively), with correspondingly smaller changes in elastic constants. For comparison, the elastic constants of the heavier inert gas crystals (Ar, Kr, Xe) decrease by more than 30% at their melting temperatures (Beamish, 2001).

The lower panel of Fig. 13 shows the ultrasonic attenuation at 10, 30, and 50 MHz. It is roughly proportional to ωT^4 below 1 K, the attenuation expected from three-phonon scattering processes in dielectric crystals (Maris, 1971). At high temperatures, the phonon scattering time τ decreases, giving approximately constant attenuations in the regime above 1 K where $\omega\tau < 1$. A T^4 dependence was also observed at gigahertz frequencies in Brillouin scattering measurements on hcp ^{4}He crystals (Berberich, Leiderer, and Hunklinger, 1976). In purer crystals, dislocations are mobile at low temperatures and add to the attenuation, overwhelming this intrinsic behavior.

At temperatures below 100 mK, the heat capacity of low density ^{3}He is dominated by spin exchange, and the internal energy has the $1/T$ dependence characteristic of a paramagnet. The corresponding low temperature decrease in sound speed was observed by Fartash and Goodkind (1986), who made measurements on a 24.1 cm^3/mol bcc ^{3}He crystal at temperatures as low as 12 mK, which is still well above bcc ^{3}He's magnetic ordering temperature $T_N = 0.93$ mK. In the magnetically ordered state below T_N, the thermal excitations are spin waves with extremely low velocities (7.8 cm/s), so the spin wave energy $u(T) = (\pi^2\hbar/15c^3)(k_BT/\hbar)^4$ and the corresponding sound velocity changes are large. This large T^4 dependence has been measured in bcc ^{3}He crystals at

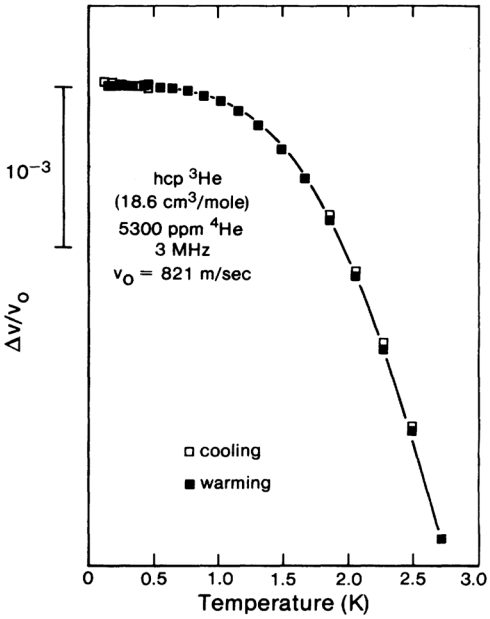

FIG. 14. Temperature dependence of the longitudinal sound speed in a hcp ^{3}He single crystal containing 0.53% ^{4}He impurities. The solid line is a fit to the intrinsic thermal phonon dependence. From Beamish and Franck, 1983.

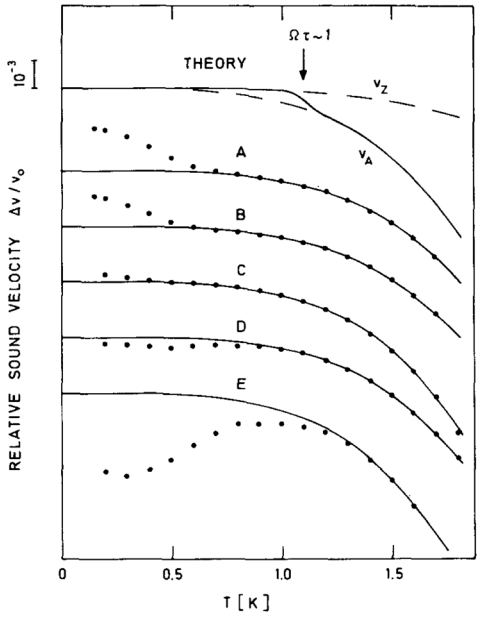

FIG. 16. Ultrasonic velocities in hcp ^{4}He single crystals at 3.6 MPa. The curves labeled *A* (top) through *E* (bottom) correspond to different crystals grown under the same conditions. Solid lines are fits to the high temperature intrinsic behavior. From Wanner, Iwasa, and Wales, 1976.

temperatures below 1 mK (Nomura *et al.*, 2000), as shown in Fig. 15. The velocity change below 0.93 mK is more than 0.01%, comparable to the total velocity changes below 1 K in Figs. 13 and 14.

C. Dislocation effects

Dislocations affect the elastic properties and sound speeds if they move in response to stresses. This occurs in helium crystals, where mobile dislocations often dominate the temperature dependence of sound velocities. This first becomes clear when ultrasonic measurements on hcp ^{4}He single crystals are extended to low temperatures. Figure 16 shows data for five different single crystals (curves *A*–*E*) grown at the same pressure. Below about half the melting temperature

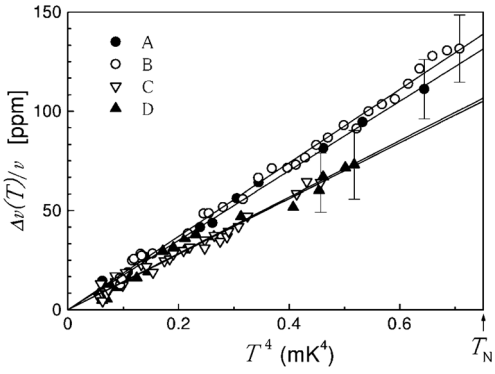

FIG. 15. Sound velocity (11 MHz longitudinal ultrasound) in magnetically ordered bcc ^{3}He single crystals in coexistence with liquid ^{3}He along the melting curve (3.44 MPa). The different symbols correspond to crystals with different orientations. From Nomura *et al.*, 2000.

($T_M \approx 1.9$ K), the longitudinal sound speeds deviate from the intrinsic T^4 dependence that described the data at higher temperatures (Wanner, Iwasa, and Wales, 1976). The deviations are smooth, with magnitudes as large as 0.3%, comparable to the intrinsic velocity changes. The size and sign of the velocity anomaly varies from crystal to crystal, consistent with the random variations expected for dislocation networks produced during crystal growth.

Although dislocations are usually thought of as softening crystals, the velocity anomalies in Fig. 16 are positive in more than half of the samples. As discussed in Sec. III.C, mobile dislocations act as vibrating strings, pinned at nodes where they intersect with other dislocations. If the damping is not too large, these strings have a resonance at a frequency f_0 given by Eq. (6). For sound frequencies below f_0, dislocations move in phase with the applied sound stress and the dislocation strain adds to the elastic strain, softening the crystal and reducing the ultrasound velocity. However, at frequencies above the dislocations' resonant frequencies the dislocation motion is out of phase with the sound stress, stiffening the crystal and increasing the sound speed. In Fig. 16, the longitudinal sound speeds are measured at 8 MHz for crystals D and E, which show negative velocity deviations at low temperatures, and at 12 MHz for the other three crystals, which show positive deviations. This suggests that the anomalies are due to dislocation loops with resonance frequencies around 10 MHz, corresponding to lengths between pinning points of about 10 μm. Wanner, Iwasa, and Wales noted that real crystals would have a distribution of loop lengths and showed that the velocity anomalies could be explained by considering just two different loop lengths.

Although the Granato-Lücke model could describe the velocity at a single frequency, the dislocation densities derived

from the fits vary from crystal to crystal, from $0.7 \times 10^5/\mathrm{cm}^2$ to $4.3 \times 10^5/\mathrm{cm}^2$, and the average loop lengths vary between 6 and 11 μm. A more stringent test of the model requires measurements at multiple frequencies. Such measurements were first made by Iwasa, Araki, and Suzuki (1979). Figure 17 shows longitudinal sound speeds at frequencies of 10, 30, and 50 MHz in a hcp ^{4}He crystal grown from natural purity helium gas (less than 1 ppm of ^{3}He impurities). The velocity anomaly is positive and, as expected, depends strongly on frequency, confirming the resonant nature of the dislocation interaction. Similar measurements were soon made on hcp and bcc single crystals of ^{3}He (Beamish and Franck, 1982). The velocity anomalies, after subtracting the high temperature intrinsic

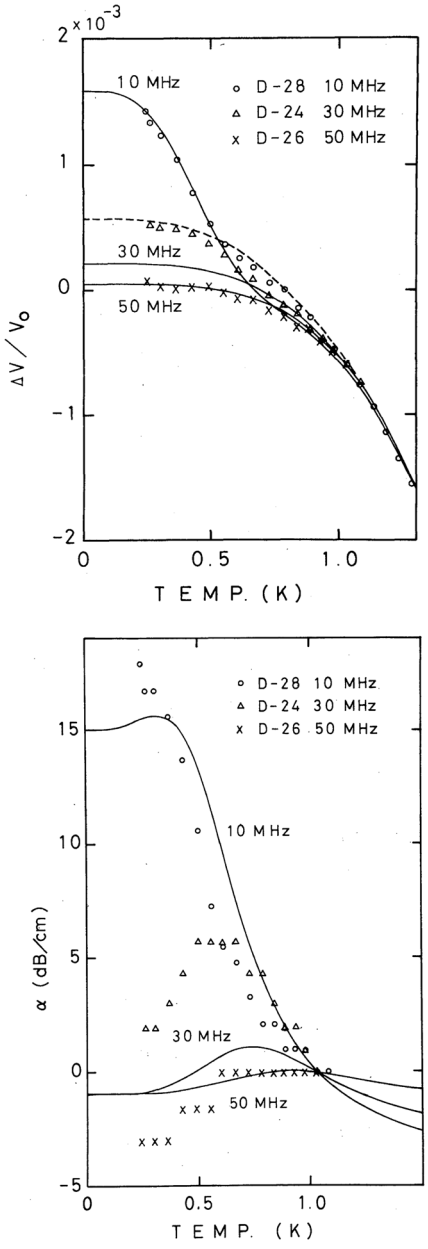

FIG. 17. Dislocation fit of the frequency-dependent longitudinal sound velocity (upper panel) and attenuation (lower panel) in hcp ^{4}He. The sound frequencies are 10 (circles), 30 (triangles), and 50 MHz (crosses). From Iwasa, Araki, and Suzuki, 1979.

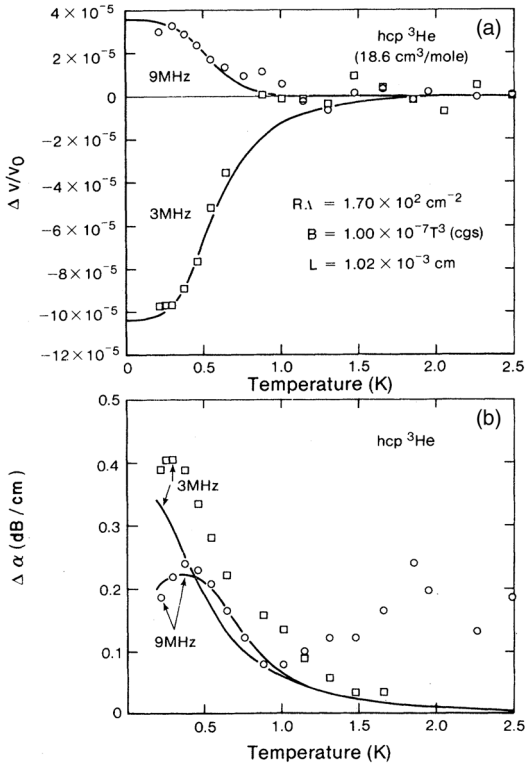

FIG. 18. Dislocation fit of the frequency-dependent longitudinal sound velocity (upper panel) and attenuation (lower panel) in hcp ^{3}He. The sound frequencies are 3 (squares) and 9 MHz (circles). From Beamish and Franck, 1982.

dependence, are shown in Fig. 18. By using lower frequencies, these measurements unambiguously show the crossover from low frequency softening at 3 MHz to high frequency stiffening at 9 MHz, convincing evidence of a resonance between 3 and 9 MHz. This is consistent with the ^{4}He measurements of Fig. 17, where the positive anomaly indicates a dislocation resonance frequency below 10 MHz.

To describe the frequency and temperature dependence of the sound velocities and of the accompanying sound attenuation (shown in the lower panels of Figs. 17 and 18), a distribution of dislocation loop lengths is needed. In the Granato-Lücke model, the contributions to the sound velocity and attenuation from a unit density of loops with length l (resonance frequency ω_0) are

$$\frac{\Delta v(l)}{v_0} = -\frac{4v_0^2}{\pi^3}\frac{\omega_0^2-\omega^2}{(\omega_0^2-\omega^2)^2+(B\omega/A)^2} \tag{8}$$

and

$$\alpha(l) = -\frac{4v_0}{\pi^3}\frac{\omega_0^2 B/A}{(\omega_0^2-\omega^2)^2+(B\omega/A)^2}. \tag{9}$$

For a distribution of loop lengths $N(l)$, the total velocity change and attenuation are

$$\frac{\Delta v}{v_0} = R\int \frac{\Delta v(l)}{v_0} l N(l) dl \tag{10}$$

and

$$\alpha = R \int \alpha(l) l N(l) dl, \tag{11}$$

where R is a numerical factor of order 0.1 that depends on the orientation of the crystal with respect to the sound polarization. Since the crystal orientations are not known in these ultrasonic experiments, only the combination $R\Lambda$ can be determined for each crystal, not the dislocation density Λ itself. Both Iwasa, Araki, and Suzuki (1979) and Beamish and Franck (1982) assumed exponential distributions of loop lengths with average length L and dislocation density Λ

$$N(l) = \frac{\Lambda}{L^2} e^{-l/L}. \tag{12}$$

The temperature dependence in these equations comes from the damping parameter B. In an insulating crystal like helium, the main damping source is thermal phonons, via the fluttering mechanism described by Ninomiya (1974). This has a characteristic $B = gT^3$ temperature dependence, with g given in Eq. (4). At the megahertz frequencies of ultrasonic measurements, the damping term $B\omega/A$ in Eqs. (8) and (9) is large near melting. At high temperatures the dislocations' motion is heavily damped and their contributions to the sound velocity and attenuation are small, as seen in Figs. 17 and 18. This means that elastic constants measured near samples' melting points, such as those listed in Table I, are the intrinsic values.

Dislocation parameters extracted from fits to the ultrasound velocities and attenuations are similar in hcp ^{4}He and ^{3}He and in bcc ^{3}He. In most crystals the average loop lengths L are between 3 and 12 μm, while the dislocation densities Λ (assuming $R = 0.1$) range from 2×10^3 to 10^6 per cm^2. Lengua and Goodkind (1990) found similar dislocation densities in hcp ^{4}He crystals grown at low pressures, but with longer loops. A range of dislocation densities and lengths in different experiments is expected, given the inevitable variations in crystal quality. Higher dislocation densities would be expected in polycrystals grown with the blocked capillary technique. However, the large sound scattering and attenuation makes ultrasonic measurements difficult in polycrystals, and there have been no comparable measurements of their dislocation parameters.

Although dislocation effects are small at high temperatures, Tsuruoka and Hiki (1979) tried to extract dislocation densities from ultrasonic attenuation measurements in hcp ^{4}He crystals near their melting temperatures. Their calculated dislocation densities were orders of magnitude larger than in other ultrasonic measurements, up to $6 \times 10^9/\text{cm}^2$. However, they used a much different method to analyze their attenuation data, and subsequent reanalysis by Paalanen, Bishop, and Dail (1981) showed that their attenuation values were consistent with the much smaller dislocation densities found in other experiments.

Although the temperature dependence of the sound velocity and attenuation anomalies is due to the thermal damping of dislocation motion, the resonance and strong frequency dependence at ultrasonic frequencies makes it impossible to confirm the phonon fluttering prediction of Ninomiya (1974) by directly measuring the temperature dependence of the damping B. However, it is clear from the ultrasonic measurements that the damping increases with temperature and the temperature dependence is consistent with a temperature dependence $B = gT^n$, with n between 2 and 4, and with a value of g similar to that predicted by Eq. (4).

When high concentrations of isotopic impurities are added to helium crystals, as in Figs. 13 and 14, the dislocation anomalies are eliminated since impurities bind to edge dislocations at low temperatures, pinning them and eliminating their contributions to the ultrasound velocity and attenuation (Iwasa and Suzuki, 1980; Beamish and Franck, 1983). As expected, the effects of impurities are strongly amplitude dependent, since stress-induced breakaway from impurity pinning sites allows dislocations to move at large ultrasonic amplitudes. Analysis of the amplitude and temperature dependence of this unpinning provided estimates (Iwasa and Suzuki, 1980) of the impurity binding energies ($\sim$0.3 K) and the forces required to detach such an impurity from a dislocation ($\sim 10^{-14}$ N). Given their weak binding to dislocations, isotopic impurity atoms are effective pinning sites only at low temperatures and for small stress amplitudes.

The impurity concentrations for the crystals of Figs. 17 and 18 (< 1 ppm ^{3}He and 1.35 ppm ^{4}He, respectively) are not sufficient to pin the dislocations, even at the lowest temperatures of these measurements. However, recent ultrasonic measurements did observe pinning below 200 mK in hcp ^{4}He crystals containing 0.3 ppm of ^{3}He mK (Iwasa and Kojima, 2017). As described later, measurements at low frequencies show qualitatively similar behavior, but the modulus changes are much larger and imply longer dislocation loops and stronger ^{3}He impurity binding. Recent low frequency measurements like those on single crystals described in Sec. V.C are much more direct and straightforward to interpret and allow dislocation parameters to be determined more reliably than from ultrasonic measurements.

V. LOW FREQUENCY ELASTIC MODULUS AND DISSIPATION

The effects of dislocations on ultrasound propagation are complicated since dislocations' inertia, string tension, and damping are all important at megahertz frequencies. Measuring the resulting frequency dependence is difficult since most ultrasonic measurements are limited to a few frequencies, multiples of the fundamental resonance of the transducers. In addition, crystals are anisotropic, with longitudinal and transverse modes, so the directions of the stresses acting on dislocations are often unknown. Even if a crystal's orientation is independently determined, ultrasonic stress amplitudes are difficult to estimate and are seldom accurately known.

At low frequencies, well below the resonance frequency of Eq. (6), dislocation effects are much simpler to interpret. The inertial term in Eq. (5) can be neglected, and the damping term is small. The elastic changes due to dislocations can be much larger than at ultrasonic frequencies since all the dislocations

move in phase with the applied stress and contribute to the softening of the crystal. In the static (zero frequency) limit, the dislocations reduce the intrinsic shear modulus μ_0 by an amount

$$\frac{\delta\mu}{\mu_0} = \frac{\alpha\Lambda L^2}{1+\alpha\Lambda L^2}. \tag{13}$$

Here α is a numerical factor ($\sim$0.05) that includes the orientation factor R to account for the component of the stress in the dislocations' glide directions and the logarithmic term in Eq. (3), which depends on the dislocations' core size and separation. Long dislocations have a larger effect than short ones, but the dislocation density Λ and the pinning length L cannot be separately determined from Eq. (13). Only the combination ΛL^2, which reflects the geometry of the dislocation network, can be found from low frequency modulus measurements. For example, a simple cubic network of dislocations with $\Lambda L^2 = 3$ would reduce the low frequency shear modulus by more than 10%. Additional pinning by impurities or jogs reduces the effective dislocation loop length and, consequently, the magnitude of shear modulus softening.

At finite frequencies, dislocation damping produces elastic dissipation. For frequencies ω well below the dislocation lines' resonance, the inertial term in Eq. (5) can still be neglected, but the damping term introduces a relaxation time $\tau = BL^2/\pi^2 C$. For $\omega\tau \ll 1$, the shear modulus is still given by Eq. (13), but the dissipation becomes

$$\frac{1}{Q} = \frac{\delta\mu}{\mu_0}\omega\tau = \frac{\delta\mu}{\mu_0}\omega\frac{BL^2}{\pi^2 C}. \tag{14}$$

The dissipation $1/Q$ depends on L more strongly than the modulus change. If both can be measured and the damping coefficient B is known, then L and Λ can be separately determined.

A. Early measurements

A number of experiments used frequencies in the kilohertz range to study the elastic modulus and dissipation in helium crystals. Tsymbalenko (1978, 1979, 1984, 1986) used quartz resonators embedded in solid helium to measure its shear modulus and internal friction. Typical results, measured at 80 kHz, are shown in Fig. 19 for four different hcp ^{4}He single crystals grown at 3.5 MPa (dotted and dashed curves labeled 1, 3, 4, and 5). Dislocations are the only defects that can explain the large shear modulus changes, up to 30%, which correspond to $\Lambda L^2 \sim 5$. The solid lines in Fig. 19 are a fit of the dislocation model described by Eqs. (8)–(11) to the data for crystal 4. The measured modulus changes are orders of magnitude larger than the changes observed in ultrasonic measurements, so longer loops ($L \sim 100$ μm) are needed to fit the modulus and dissipation data. The shear modulus (left panel) and the decrement (right panel) both decrease below 1 K, confirming that dislocations are more mobile and less damped at low temperatures. The temperature dependence is consistent with a damping $B = gT^n$, with an exponent n close

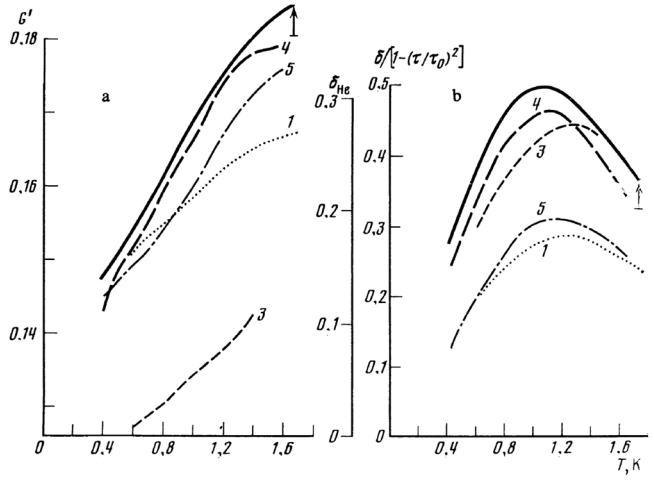

FIG. 19. Shear modulus G (left panel) and decrement $\delta_{\mathrm{He}} \propto 1/Q$ (right panel) for hcp ^{4}He single crystals grown at 3.5 MPa. The dotted and dashed curves (labeled 1, 3, 4, and 5) are data for four different crystals grown under the same conditions. The solid curves are dislocation fits to the data of crystal 4. From Tsymbalenko, 1984.

to 3, but to get satisfactory fits it is necessary to include the inertial term in Eq. (5).

Paalanen, Bishop, and Dail (1981) studied helium's elastic properties at an even lower frequency (331 Hz) using a torsional oscillator technique. In contrast to torsional oscillators used to search for supersolidity, this oscillator's inertial element did not contain helium. The torsion rod, however, was filled with solid helium, whose shear modulus and dissipation were determined from the frequency and quality factor of the torsional oscillator. As shown in the top panel of Fig. 20, the

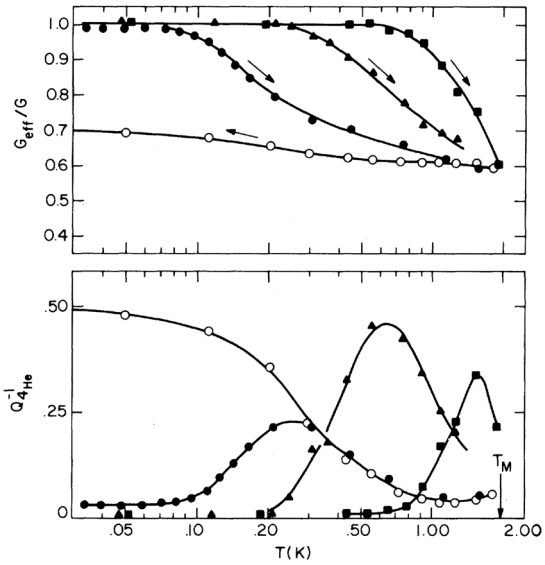

FIG. 20. Torsional oscillator measurements of the normalized shear modulus (upper panel) and dissipation (lower panel) in a hcp ^{4}He polycrystal at 3.7 MPa. The measurement frequency is 331 Hz and the data are taken at strain amplitudes $\epsilon = 10^{-7}$ (squares), $\epsilon = 6\times10^{-7}$ (triangles), and $\epsilon = 10^{-5}$ (circles). From Paalanen, Bishop, and Dail, 1981.

shear modulus changes by up to 40% when the solid was cooled, from which they inferred that $\Lambda L^2 = 2$. However, the modulus *increased* at low temperatures, implying that dislocations were less mobile at low temperatures, in contrast to the 30% *decrease* in the 80 kHz measurements of Tsymbalenko (1984). The changes in shear modulus were accompanied by dissipation peaks (lower panel of Fig. 20). Both the modulus and dissipation depend strongly on the strain amplitude and the ^{3}He concentration. The low temperature stiffening in Fig. 20 is consistent with impurity pinning, with an amplitude dependence and hysteresis due to stress-induced breakaway of dislocations. From the temperature dependence of the breakaway amplitude, Paalanen, Bishop, and Dail (1981) deduced an impurity binding energy $E_B = 0.7$ K.

There was some uncertainty in the ^{3}He impurity concentration in the sample of Fig. 20. It was described as "commercial ^{4}He," but its unpinning temperatures are higher than in other samples, suggesting larger impurity concentrations. Paalanen, Bishop, and Dail described it as having ^{3}He concentrations "probably less than 3 ppm," about 10 times larger than is usually found in commercial helium gas. In their samples with extremely low ^{3}He concentrations ($x_3 = 2.4 \times 10^{-9}$) the shear modulus, shown in the upper panel of Fig. 21, was independent of temperature, as expected if there is no impurity pinning. The dissipation in the isotopically pure samples, shown in the lower panel of Fig. 21, was relatively small, without the impurity breakaway peaks of Fig. 20. In the sample whose data are shown as solid symbols, the shear modulus was small, indicating that the dislocations were mobile. The corresponding dissipation

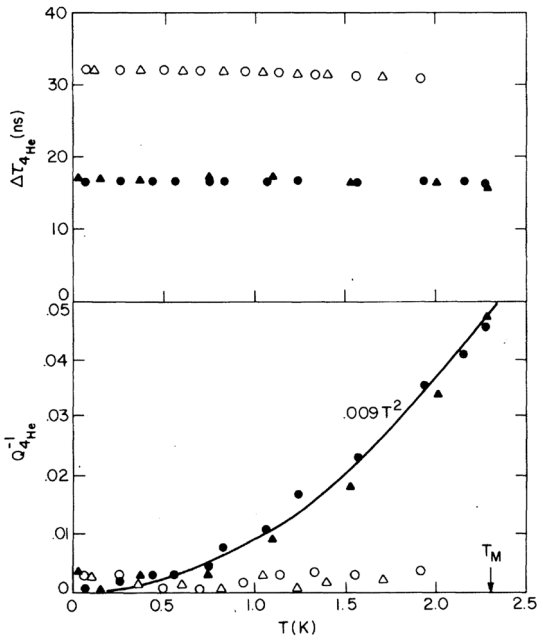

FIG. 21. Torsional oscillator measurements of the period shift, proportional to the shear modulus change (upper panel) and dissipation (lower panel) for isotopically pure ($x_3 = 2.4$ ppb) hcp ^{4}He crytals at 4.8 MPa. Open and closed symbols correspond to two samples with different orientations. The measurement frequency is 331 Hz and the data are taken at strain amplitudes $\epsilon = 6 \times 10^{-7}$ (triangles) and $\epsilon = 10^{-5}$ (circles). From Paalanen, Bishop, and Dail, 1981.

increases roughly as T^2, weaker than the T^3 dependence noted by Tsymbalenko, but the fits to the dissipation were made over different temperature ranges. The other high purity sample, corresponding to the open symbols, has a larger shear modulus and negligible dissipation, indicating that dislocation effects are much smaller in this sample, likely because of its orientation. Paalanen, Bishop, and Dail (1981) showed that their high temperature dissipation values at 331 Hz were consistent with those from earlier work by Tsymbalenko (1978) at 15 kHz and by Tsuruoka and Hiki (1979) at megahertz ultrasonics frequencies, with no need for the large dislocation densities assumed in the latter paper.

The low frequency measurements were consistent with many features observed in ultrasonic experiments. They confirm that dislocations can soften the shear modulus, are thermally damped at high frequencies and temperatures, and are pinned by ^{3}He impurities at low temperatures and stresses. There are, however, significant differences between the low and high frequency results. Modulus changes are much larger in the low frequency measurements, up to 40%, compared to less than 1% in ultrasonic measurements. Some of this difference is due to the inertial effects that limit dislocation motion at megahertz frequencies. However, the values extracted for the dislocation network parameter ΛL^2 were much smaller in the ultrasonic measurements (between ~0.001 and 0.1) than in the low frequency measurements of Paalanen, Bishop, and Dail (1981) and Tsymbalenko (1984) (between ~2 and 6). The extracted dislocation densities Λ were comparable in the ultrasonic measurements and the 80 kHz measurements of Tsymbalenko (1984) (~10^4 to $10^5/\text{cm}^2$ and ~$10^4/\text{cm}^2$, respectively) but the pinning lengths were significantly different, ~5 μm in the ultrasonic measurements versus ~100 μm in the measurements of Tsymbalenko (1984). Some discrepancies are expected since the crystal qualities may be different in the various experiments, but the large differences in ΛL^2 and L are puzzling. In addition, although the thermal damping in all the experiments appears to be proportional to T^n, with n between 2 and 4, the magnitude of the damping B was about 2 orders of magnitude larger in the measurements of Tsymbalenko (1984). This is surprising since B is an intrinsic property of individual dislocations and should not depend on their density or lengths. More direct and detailed recent measurements of damping in single crystals, described in Sec. V.C, show similar large modulus changes but are not consistent with the B values of Tsymbalenko (1984), instead confirming the expected phonon scattering damping B.

This torsional oscillator technique has also been used to study dislocation effects in bcc ^{3}He. Miura *et al.* (1998, 2000) and Miura, Mori, and Mamiya (2000) observed a dissipation proportional to T^3 and shear modulus decreases as large as 60% at high temperature, suggesting that ΛL^2 was at least as large as in hcp ^{4}He. However, they were not able to determine the dislocation densities or lengths separately.

B. Shear modulus measurements in polycrystals

To resolve discrepancies between the dislocation parameters determined by the high and low frequency measurements,

unambiguous measurements of the thermal damping coefficient B were needed. As noted by Tsymbalenko (1978), this requires measurements over a wide range of frequencies. However, this is not practical with resonant techniques like torsional oscillators and quartz resonators, nor with ultrasonic methods. Nonresonant techniques allow the frequency to be varied continuously but are usually less sensitive. However, with modern electronics that takes advantage of the reduced noise levels at low temperatures, extremely sensitive nonresonant measurements can be made on solid helium.

The low frequency shear modulus of polycrystalline hcp ^{4}He was measured by Day and Beamish (2007b) using such techniques. Helium crystals were grown in a narrow gap ($D = 180$ μm) between two parallel shear piezoelectric transducers. A voltage V applied to one transducer generates a shear displacement δx and a uniform shear strain $\epsilon = \delta x/D$ in the helium. This produces a shear stress σ and a corresponding charge q on the opposite transducer, allowing the shear modulus of the solid helium $\mu = \sigma/\epsilon$ to be calculated. To determine absolute rather than relative values, the transducers were calibrated at the low temperatures of the measurements (Bukhari *et al.*, 2014; Islam and Beamish, 2019). For ac measurements of the shear modulus, a lock-in amplifier also gave the dissipation in the helium, which is related to the measured phase lag ϕ between the stress and strain $1/Q = \tan\phi$. With this technique, the measurement frequency could be varied continuously up to 16 kHz, limited only by mechanical resonances of the pressure cell and acoustic resonances of the solid helium inside it. The lower frequency limit, of the order of 1 Hz, was set by noise in the stress measurements. Using this technique, which has a stress resolution of 2×10^{-6} Pa at the highest frequencies, solid helium's shear modulus was measured at frequencies from 0.5 Hz to 16 kHz (Syshchenko, Day, and Beamish, 2010; Haziot, Fefferman, Souris *et al.*, 2013), and at strains as low as 2×10^{-11} (Haziot *et al.*, 2013a).

Figure 22(a) shows the changes in the shear modulus of a hcp ^{4}He sample with a nominal ^{3}He impurity concentration of 300 ppb (300×10^{-9}). The polycrystalline solid was grown using the blocked capillary technique, with a final pressure of 3.33 MPa (Day and Beamish, 2007b). The shear modulus was essentially constant between the melting temperature (1.86 K) and 200 mK, then increased at lower temperatures, reaching the solid's intrinsic value at the lowest temperatures (Day, Syshchenko, and Beamish, 2009). The total change, about 8%, is somewhat smaller than the dislocation softening seen in some earlier low frequency measurements on helium single crystals and corresponds to a network with $\alpha\Lambda L^2 \approx 0.09$; see Eq. (13). The temperature at which the softening occurs depends on the measurement frequency, as shown in Fig. 22(a) for frequencies of 20, 200, and 2000 Hz. It was also extremely sensitive to the ^{3}He impurity concentration, as shown in Fig. 22(b) for 3.3 MPa crystals with $x_3 = 1, 85$, and 300 ppb. The measurements in Figs. 22(a) and 22(b) were made at extremely small shear strains ($\epsilon = 3 \times 10^{-9}$, corresponding to stress $\sigma \approx 0.05$ Pa). As shown in Fig. 22(c), the low temperature shear stiffening was reduced at strains above 2×10^{-8}. However, the shear modulus above 200 mK was essentially independent of the strain amplitude.

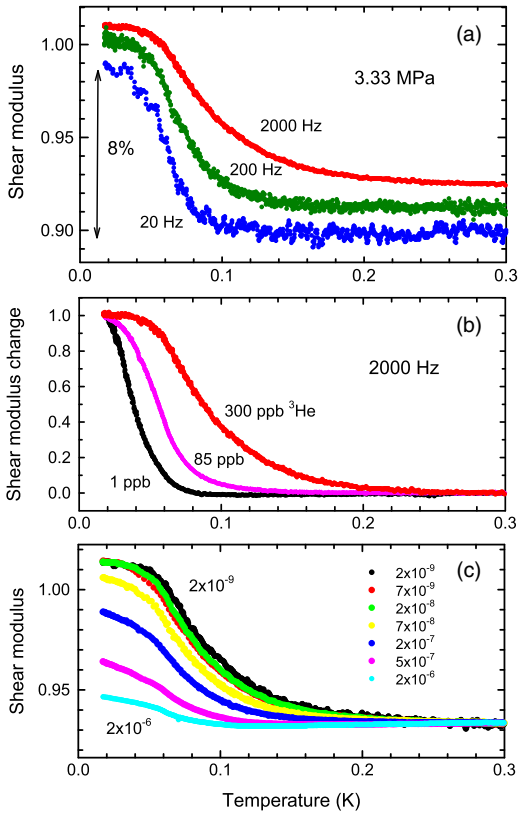

FIG. 22. Shear modulus in a hcp ^{4}He polycrystal at 3.33 MPa. (a) Normalized modulus at low strain $\epsilon = 3 \times 10^{-9}$ for frequencies of 20, 200, and 2000 Hz (b) Shear modulus changes at low strain for samples with different ^{3}He impurity concentrations, normalized to the total changes from low to high temperature for each sample. (c) Amplitude dependence of the shear modulus at 2000 Hz for strains (from top to bottom) between 2×10^{-9} (top curve, black symbols) and 2×10^{-6} (bottom curve, cyan symbols).

This is the behavior expected for a network of dislocations that are pinned by weakly bound ^{3}He impurities at low temperatures. For a binding energy E_B, the equilibrium concentration of ^{3}He atoms along the dislocation is $x_3^{\rm dis} = x_3 e^{E_B/k_B T}$. At high temperature, the ^{3}He atoms unbind and the impurity pinning length L_i, which is inversely proportional to $x_3^{\rm dis}$, increases. When L_i becomes comparable to the network length L_N, the dislocations are able to move and reduce the crystal's intrinsic shear modulus. In Fig. 22(a) this occurs at around 200 mK, but the pinning length, and hence the softening temperature, depends on the sample's ^{3}He concentration, as shown in Fig. 22(b). Assuming that the three samples had similar network lengths, this allows the ^{3}He binding energy to be estimated as $E_B \approx 0.7$ K, which is consistent with the value from Paalanen, Bishop, and Dail (1981). The amplitude dependence in Fig. 22(c) reflects dislocations breaking away from ^{3}He pinning sites when the force exerted by the applied stress exceeds a threshold. In the high temperature regime, where impurity pinning can be neglected, the shear modulus is independent of the stress amplitude because the network pinning is much stronger.

The frequency dependence of the softening shown in Fig. 22(a) can be well described by a thermally activated

relaxation process. The activation energy 0.7 K is essentially the same as expected if the dislocation unpinning rate is controlled by thermally activated unbinding of the impurities. Alternatively, bound impurities might move with dislocations and produce a damping force proportional to their density, giving the same activation energy.

The behavior is similar in ^{3}He (West *et al.*, 2009). Figure 23 shows the normalized shear modulus for a hcp ^{3}He polycrystal at a pressure of 11.9 MPa. The temperature at which the modulus softens was higher than in hcp ^{4}He, which is expected given the larger impurity concentration in the ^{3}He sample ($x_4 = 1.35$ ppm). As for ^{4}He, the stiffening shifted to lower temperature and disappears at large strains, with a similar threshold for breakaway. Neither the dependence on frequency nor that on impurity concentration was measured in these experiments, so the ^{4}He impurity binding energy could not be determined, but ultrasonic experiments extracted similar isotopic impurity binding energies in hcp ^{3}He and ^{4}He crystals. For the bcc phase of ^{3}He, dislocation effects were not obvious but were seen more clearly in subsequent experiments (Cheng, Souris, and Beamish, 2016).

The origin of the modulus changes in solid helium was confirmed by the effects of annealing, which is expected to reduce the density of defects like dislocations. Figure 24 shows the shear modulus changes for hcp ^{4}He (upper pair of curves) and hcp ^{3}He (lower pair of curves). Samples were frozen using the blocked capillary technique, which produces samples with many grain boundaries and dislocations. The lower (black) set of data in each pair of curves in Fig. 24 is measured when the samples were first cooled, immediately after freezing. The modulus changes were similar in the 3.33 MPa ^{4}He sample and the 11.9 MPa ^{3}He sample, about 8% in each case (Day, Syshchenko, and Beamish, 2009). When the samples were annealed for several hours near their melting temperatures, their shear moduli increased by 1%–2%. However, when an annealed sample was subsequently cooled (upper red set of data in each pair of curves), its shear modulus returned to the preannealing value at the lowest temperature, as expected when dislocations are completely pinned by impurities. This confirmed that the values at the lowest temperatures reflect the intrinsic shear moduli of perfect crystals, unaffected by the now immobile dislocations. The changes in the dislocation network during annealing reduced the high temperature softening by about 20%. However, this is not a direct measure of dislocation densities since the modulus change is proportional to ΛL^2. A decrease in density Λ is usually accompanied by an increase in the network length L, which reduces the modulus change due to annealing or can even change its sign (Day, Syshchenko, and Beamish, 2009).

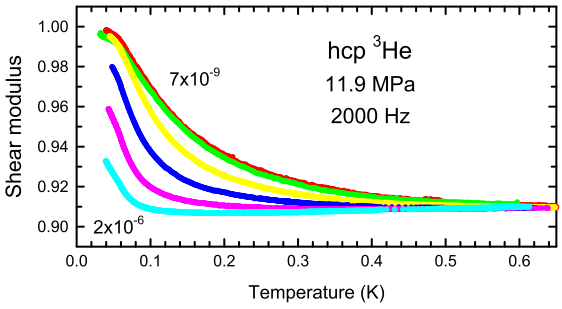

FIG. 23. Amplitude dependence of the shear modulus in a hcp ^{3}He polycrystal at 11.9 MPa measured at 2000 Hz. The modulus is normalized to the value at the lowest temperature and strain. Strain amplitudes for the different curves vary (from top to bottom) from 7×10^{-9} (top curve, red symbols) to 2×10^{-6} (bottom curve, cyan symbols) with the same strain values as the corresponding curves in Fig. 22.

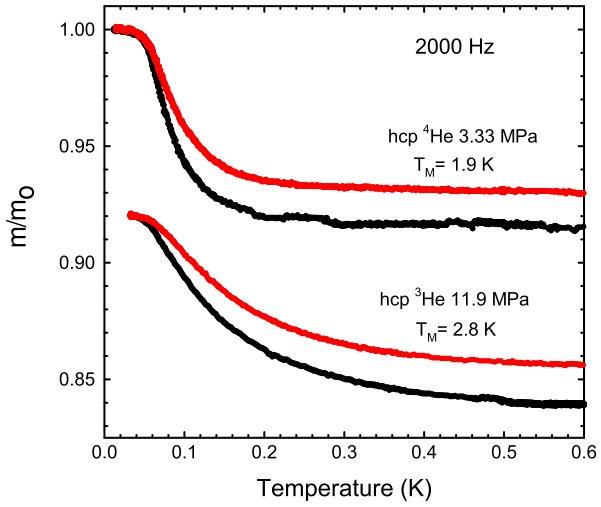

FIG. 24. Effect of annealing on the shear modulus softening in helium polycrystals. The upper pair of curves show the normalized modulus at 2000 Hz for hcp ^{4}He containing 0.3 ppm ^{3}He impurities at a pressure of 3.33 MPa (33.3 bar). The lower pair of curves are for hcp ^{3}He containing 1.35 ppm ^{4}He impurities at 11.9 MPa (119 bar). For each sample, the lower (black) data are before annealing; the upper (red) data are after annealing. From Day, Syshchenko, and Beamish, 2009.

Large stresses can also change the dislocation network (Day, Syshchenko, and Beamish, 2009; Cheng and Beamish, 2018b). Figure 25 compares the shear moduli of hcp ^{4}He samples with ^{3}He impurity concentrations of 300 ppb (upper pair of curves) and 1 ppb (lower set of three curves). As for the helium crystals of Fig. 24, the initial shear modulus of the high purity (1 ppb ^{3}He) sample (lowest curve, black symbols) increases after annealing (middle of the three curves, red symbols) but returns to the same intrinsic value at the lowest temperature. When large acoustic strains ($\epsilon \sim 10^{-4}$) are applied to the annealed sample at low temperatures, the shear modulus does not change. However, when the stressed sample is then warmed (uppermost of the three curves, blue symbols) the modulus behavior is different: it is clear that the large stresses affect the dislocation network. The upper pair of curves show the same effect in a sample with a higher ^{3}He concentration. Counterintuitively, applying the large stresses reduces the softening due to dislocations. This suggests that the effect of the low temperature stresses is to partially pin existing dislocations rather than create new ones. Warming above 0.5 K reverses the effects of the acoustic stress and repeating the process gives reproducible hysteresis loops. The ease with which the stress effects are annealed suggests that

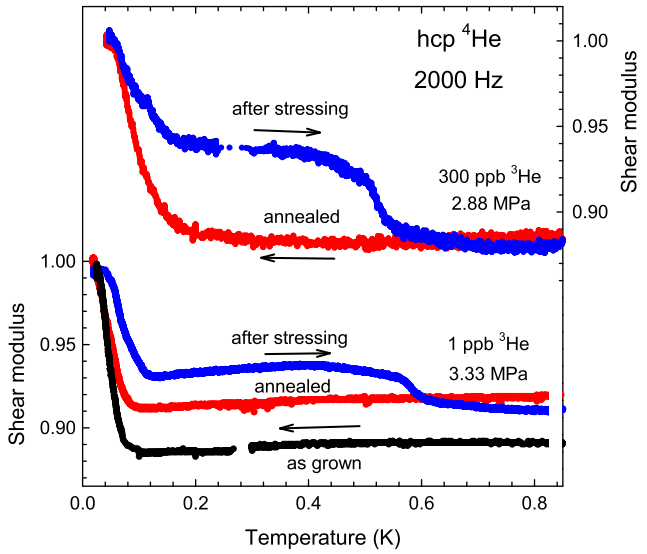

FIG. 25. Effects of stressing and annealing on the shear modulus of hcp ^{4}He with 300 ppb ^{3}He (2.88 MPa, upper pair of curves) and with 1 ppb ^{3}He (3.33 MPa, lower set of three curves). For each sample, the modulus is normalized to the value at the lowest temperature. The various curves are discussed in the text (Day, Syshchenko, and Beamish, 2009).

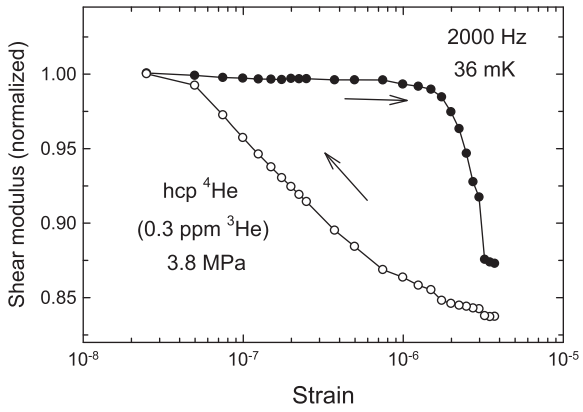

FIG. 26. Low temperature hysteresis due to impurity pinning and unpinning in hcp ^{4}He at 3.8 MPa. Open symbols show the shear modulus measured while decreasing the strain; solid symbols are data taken while increasing the strain. From Day, Syshchenko, and Beamish, 2010.

the new pinning sites may be jogs, which can be removed by dislocation climb when thermal vacancies are available (Hull and Bacon, 2011).

Even at lower stresses, where new dislocations and jogs are not created, stress-induced breakaway from impurity pinning sites leads to hysteresis when the strain amplitude is cycled (Granato and Lücke, 1981). Figure 26 shows a hysteresis loop for hcp ^{4}He at 36 mK (Day, Syshchenko, and Beamish, 2010). The open symbols show the increase in normalized shear modulus when the strain amplitude ϵ was reduced from 4×10^{-6} (where dislocations have broken away from ^{3}He impurities) to 2×10^{-8} (where they are pinned). When the strain amplitude was then increased (solid symbols), the shear modulus remained at its large intrinsic value up to strains of about 10^{-6}, then dropped rapidly. This type of hysteresis arises because the force pulling a dislocation away from an impurity increases with the distance between pinning points, as well as with the applied stress (Iwasa, 2013; Kang, Yoon, and Kim, 2015). At sufficiently high stress, dislocations are free of bound ^{3}He, so this loop length is that between nodes of the dislocation network. If the stress amplitude is gradually reduced below the critical value, ^{3}He atoms can bind to dislocations, beginning with the shortest loops. This reduces the distance between pinning sites, which allows more ^{3}He atoms to bind and quickly immobilizes this dislocation loop. As the strain amplitude is reduced, successively longer loops are pinned and the distribution of network lengths can be inferred from the amplitude dependence of the shear modulus (the open circles in Fig. 26). The hysteresis arises because when one begins at low strain, the bound impurities are closely spaced and do not break away unless much larger stresses are applied. A lower limit on the time required to pin dislocations at low temperature can be inferred from the fact that the impurities do not pin the dislocations during the part of the ac cycle when the stress goes through zero. The pinning time must be longer than this millisecond scale.

At higher temperatures, where the unpinning from impurities is thermally assisted (Lücke, Granato, and Teutonico, 1968), Kang *et al.* (2013) showed that the hysteresis decreases rapidly, disappearing at around 70 mK. The combination of amplitude and temperature dependence produces complicated elastic behavior that Kang *et al.* (2013) summarized in the stress-temperature "hysteresis map" for polycrystalline hcp ^{4}He shown in Fig. 27.

Similar behavior was seen in torsional oscillator measurements (Pratt *et al.*, 2011), where the amplitude dependence was interpreted as a velocity dependence rather than a stress dependence. However, it is now clear that these and other torsional oscillator experiments were actually probing the shear modulus of solid helium, not inertial effects that might signal supersolidity (Beamish *et al.*, 2012). The connection between a torsional oscillator's frequency and damping and helium's elastic properties has been directly confirmed in

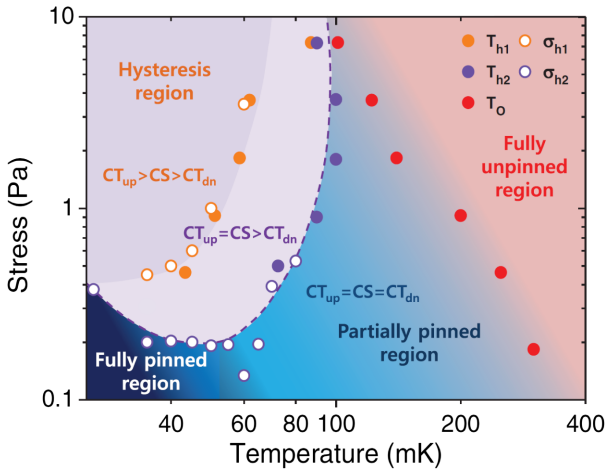

FIG. 27. Stress-temperature map of solid ^{4}He from shear modulus measurement. From Kang *et al.*, 2013.

experiments in which the solid helium's shear modulus was measured simultaneously using piezoelectric transducers inside the torsional oscillator (Kim *et al.*, 2011; Shin *et al.*, 2016).

The frequency dependence of the shear modulus seen in Fig. 22(a) is mirrored in the corresponding dissipation $1/Q$. Figure 28 shows the low amplitude shear modulus and dissipation for a hcp ^{4}He polycrystal, measured at frequencies between 2 and 2000 Hz (Syshchenko, Day, and Beamish, 2010). The open circles in Fig. 28 mark the midpoints of the modulus change and the positions of the accompanying dissipation peaks. The dissipation peaks coincide with the midpoints of the modulus softening, as expected for a Debye relaxation process. They shift to higher temperatures with increasing frequency, suggesting that the relaxation process is thermally activated. This is confirmed by the Arrhenius plots of Fig. 29, where the softening midpoint and dissipation peak positions are shown for the samples of Figs. 22(a) and 28. The slopes, shown by solid lines, correspond to activation energies of approximately 0.7 K, which is consistent with the binding energy estimated from the ^{3}He impurity concentration dependence.

For a Debye process with relaxation time τ and a small relaxation strength $\delta\mu/\mu_0 \ll 1$, the modulus and dissipation are given by (Nowick and Berry, 1972)

$$\frac{\mu}{\mu_0} = 1 - \frac{\delta\mu}{\mu_0}\frac{1}{1+(\omega\tau)^2}, \tag{15}$$

$$\frac{1}{Q} = \frac{\delta\mu}{\mu_0}\frac{\omega\tau}{1+(\omega\tau)^2}, \tag{16}$$

where μ_0 is the "unrelaxed modulus" ($\omega\tau \gg 1$) and $\mu_0 - \delta\mu$ is the "relaxed modulus" ($\omega\tau \ll 1$). For dislocations the relaxation time could be the one associated with their damping by thermal phonons $\tau = BL^2/\pi^2 C$. Other relaxation processes could be thermally activated, with $\tau(E) = \tau_0 e^{E/T}$, where E is the activation energy. The midpoint of the modulus crossover and the dissipation maximum occur at the temperature where $\omega\tau = 1$. However, a Debye relaxation with a single activation energy (0.73 K) and an attempt time τ_0 (25 ns), the values suggested by Fig. 29, gives a shear modulus crossover and dissipation peak (dashed blue lines) much narrower than were observed, as shown in Fig. 30 (Syshchenko, Day, and Beamish, 2010). The measured dissipation peak was also much smaller than the expected Debye value $(1/Q)_{\text{peak}} = (1/2)(\delta\mu/\mu_0)$. However, the broadening of the shear modulus crossover and dissipation could be explained if the relaxation process involved a distribution of activation energies rather than a single value. The solid red lines in Fig. 30 show a fit to the data with a distribution of activation energies with width $W = 0.45$ around an average value of 0.73 K. Mukharsky, Penzev, and Varoquaux (2009) and Mukharsky and Penzev (2012) observed similar behavior in measurements of uniaxial compression of polycrystalline ^{4}He between 10 Hz and 4 kHz. The temperature and frequency dependences were similar to those of the shear modulus, as were the activation parameters ($E \approx 0.62$ K, $W \approx 0.71$). This is expected since uniaxial compression involves shear deformations and thus is affected by dislocation motion in the same way.

Kang, Yoon, and Kim (2015) showed that the complete temperature and stress dependence, including the hysteresis when the stress amplitude is cycled, could be quantitatively reproduced with a Granato-Lücke dislocation model that includes impurity pinning and a distribution of network lengths. The lower panels of Fig. 31 show their measured shear modulus and dissipation in hcp ^{4}He at a frequency of 1000 Hz. The calculated values shown in the upper panels

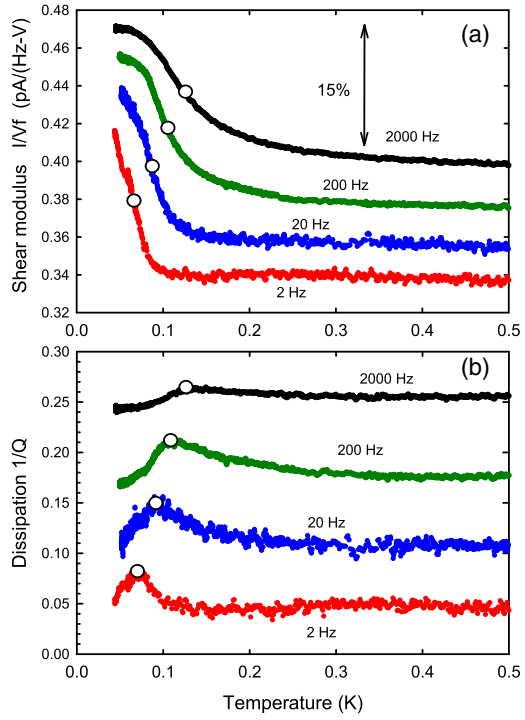

FIG. 28. (a) Shear modulus in a hcp ^{4}He polycrystal at 3.8 MPa for frequencies between 2 and 2000 Hz. Circles mark the midpoints of the modulus softening. (b) Corresponding dissipation, with circles marking the peak values. Curves are vertically shifted for clarity. From Syshchenko, Day, and Beamish, 2010.

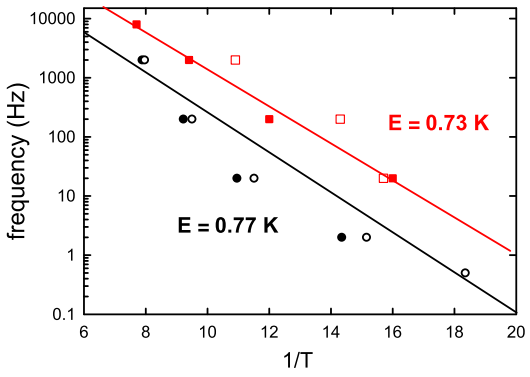

FIG. 29. Arrhenius plot of the crossover temperatures for the 3.8 MPa sample of Fig. 28 (lower black symbols and line) and the 3.3 MPa sample of Fig. 22(a) (upper red symbols and line). Open symbols are the midpoints of the shear modulus softening; solid symbols are the dissipation peak maxima. From Syshchenko, Day, and Beamish, 2010.

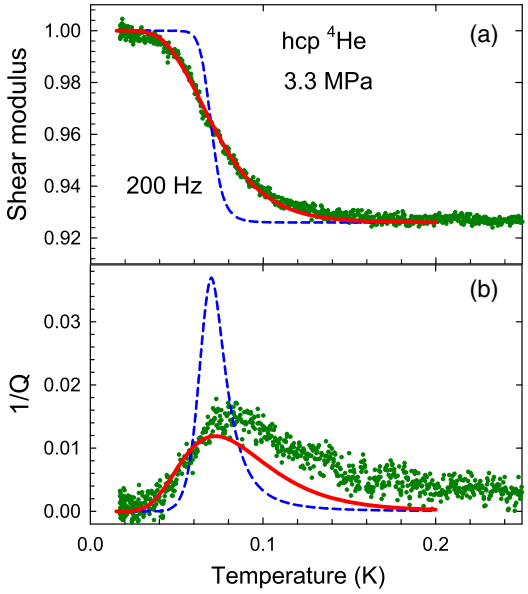

FIG. 30. Debye relaxation fits of (a) the normalized shear modulus and (b) the dissipation at 200 Hz in the 3.3 MPa ^{4}He sample of Fig. 29. The dashed blue line is the fit for a single activation energy $E_B = 0.73$ K. The solid red line is a fit using a distribution of activation energies.

(for a dislocation density $R\Lambda = 2 \times 10^{-6}$ cm^{-2} and network length $L = 5$ μm) agree well with the data. The ^{3}He binding energy used to fit the data $E = 0.3$ K was smaller than inferred from the frequency dependence in Figs. 22 and 29 but is based on data at a single frequency. Their model does not include a distribution of activation energies, which broadens the modulus crossover and the dissipation peak, mimicking a smaller activation energy.

As shown in Figs. 22–24, the shear modulus changes are similar in the hcp phases of ^{3}He and ^{4}He. However, the dynamics of dislocation motion were significantly different in hcp ^{3}He (Cheng and Beamish, 2017). In contrast to ^{4}He, the shear softening in hcp ^{3}He was independent of frequency, as shown in Fig. 32(a). This suggests that in hcp ^{3}He, the ^{4}He impurities act as static pinning sites over the full frequency range 22–5402 Hz. This is different from the dynamic impurity behavior in hcp ^{4}He, where ^{3}He impurities appear to move with dislocations, damping their motion and producing the strong frequency dependence seen in the shear modulus and dissipation of Fig. 32(b). However, the shear modulus in hcp ^{4}He single crystals is also frequency independent at high frequencies, when dislocation speeds exceed about 45 μm/s (Haziot, Fefferman, Souris *et al.*, 2013) and the ^{3}He impurities cannot move fast enough to follow the dislocations. The essentially static nature of impurity pinning in hcp ^{3}He at frequencies as low as 22 Hz is consistent with the lower mobility of impurities in hcp ^{3}He, where disorder in the ^{3}He spins prevents impurities from propagating ballistically. At sufficiently low frequencies and strains, diffusive motion of ^{4}He impurities should allow them to move with the dislocations in solid ^{3}He, like the dragging of the Cottrell atmosphere

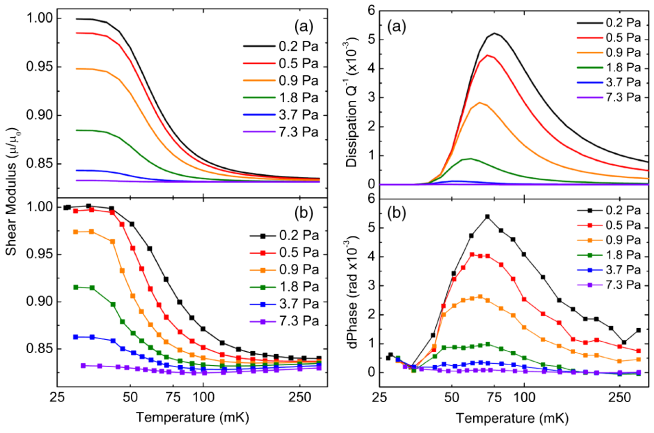

FIG. 31. Shear modulus (left panels) and dissipation (right panels) for a hcp ^{4}He polycrystal at 3.9 MPa, measured at 1000 Hz and stresses between 0.2 and 7.3 Pa. (a) Values calculated using an impurity binding energy distribution as described in the text. (b) Measured values. Curves are ordered top to bottom as in the corresponding legends for each panel. From Kang, Yoon, and Kim, 2015.

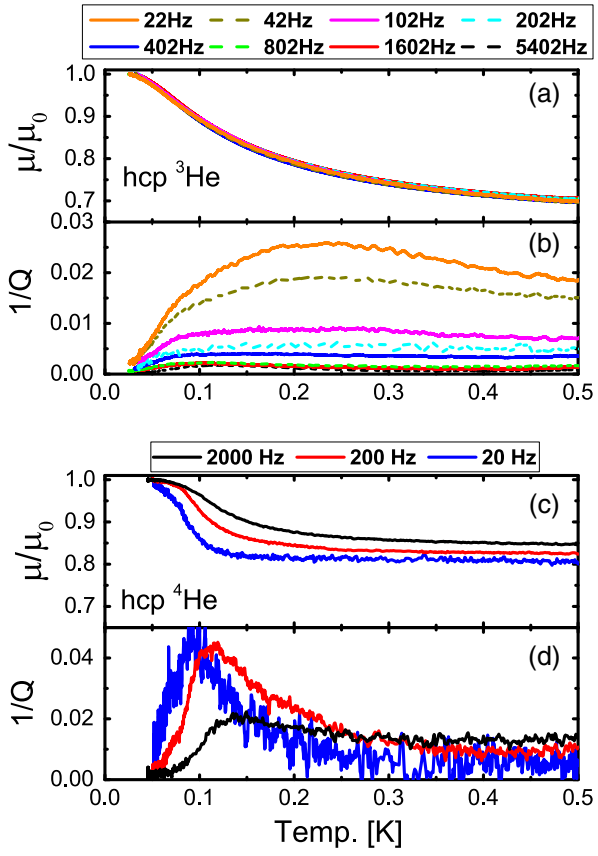

FIG. 32. Frequency dependence of the normalized shear modulus μ/μ_0 and dissipation $1/Q$ in helium polycrystals. (a),(b) hcp ^{3}He at 11.9 MPa. The magnitude of the dissipation in hcp ^{3}He decreases monotonically as the frequency increases from 22 Hz (upper orange curve) to 5402 Hz (lowest dashed black curve). (c), (d) hcp ^{4}He at 3.8 MPa. The shear modulus crossover and the corresponding dissipation peak in hcp ^{4}He shifts to higher temperatures as the frequency increases from 20 to 2000 Hz. From Cheng and Beamish, 2017.

of impurities around dislocations in classical crystals (Takeuchi and Argon, 1979). The expected frequency dependence would occur in a regime below that shown in Fig. 32(a).

The dissipation in hcp ^{3}He shown in Fig. 32(b) was also quite different from that in hcp ^{4}He. As expected for static pinning, the thermally activated dissipation peak associated with impurity unpinning in hcp ^{4}He is absent in hcp ^{3}He, or at least greatly reduced. Instead, the dissipation in ^{3}He extended over a broad temperature region. When the frequency was lowered, the magnitude of the dissipation increased rapidly and its broad maximum shifted to higher temperatures, the opposite direction to that of thermally activated relaxation peaks like those in hcp ^{4}He. This behavior suggests that the dissipation in hcp ^{3}He is not due to a damping force proportional to the dislocation speed, as in the Granato-Lücke equation (5). Instead, Cheng and Beamish (2017) proposed that the dissipation may be due to a velocity-independent, frictionlike energy loss associated with rearrangements of spin configurations when a dislocation moves through ^{3}He. However, initial measurements on bcc ^{3}He polycrystals (Cheng, Souris, and Beamish, 2016) show frequency-dependent shear modulus changes and dissipation peaks that resemble those in hcp ^{4}He. This suggests that ^{4}He impurities are much more mobile in the bcc phase, despite the much larger spin exchange energies in bcc ^{3}He (Ceperley and Jacucci, 1987). However, dislocation structures and mobilities in bcc structures are significantly different than those of hcp crystals, e.g., they are usually not split into partials and often have significant Peierls barriers to gliding. The narrow temperature range for the bcc phase of ^{4}He means that there is no way to directly compare the low temperature behavior of dislocations in bcc ^{3}He to that in bcc ^{4}He.

Although many features of dislocation motion in helium are clear from these experiments on polycrystals, more detailed and quantitative information can be obtained from similar measurements on single crystals.

C. Dislocations and giant plasticity in single crystals

The low frequency experiments described in Sec. V.B involved polycrystalline samples grown using the blocked capillary technique. There was little control of sample quality and the measured shear moduli were averages over different crystallite orientations. Although dislocation behavior has been studied in ultrasonic and elastic experiments on single crystals grown at constant pressure, the crystal quality varied and their orientations were not known. Measurements on oriented single crystals can provide information on individual elastic constants. If the sample cell and refrigerator have windows for optical access, crystal orientations can be determined from the facets seen during growth, and there can be more control of crystal growth and quality by melting and regrowing from small seed crystals. Rojas *et al.* (2010) used an acoustic resonance technique in such a cell to study the elastic behavior of oriented single crystals of hcp ^{4}He. However, measurements were limited to the solid helium's acoustic resonance around 18 kHz and depended in a complicated way on all the crystal's elastic constants.

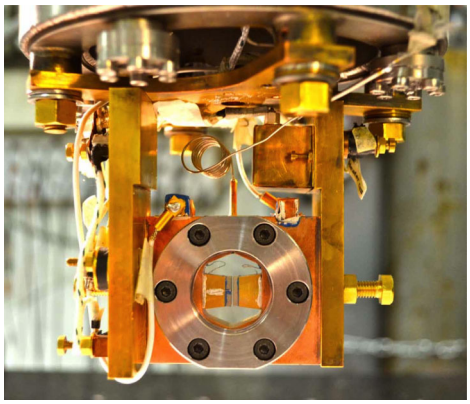

FIG. 33. The experimental cell used to measure mechanical properties of ^{4}He crystals at ENS (Paris). Single crystals are grown from the bottom up, inside the 0.7 mm slit between two vertical transducers in the center of the cell. Crystal orientations are obtained from photographs of facets when they begin growing in the bottom part of the cell (see Fig. 35). From Haziot, Fefferman, Beamish, and Balibar, 2013.

To measure the shear modulus of ^{4}He single crystals, Haziot *et al.* (2013a) used the transparent cell shown in Fig. 33. It was made from a copper plate with an approximately hexagonal hole in which the helium crystals were grown, closed by two sapphire windows. The cell was attached to a dilution refrigerator whose base temperature was 15 mK, even with the windows that provide the optical access for the external camera used to record crystals' growth shapes (Balibar, Alles, and Parshin, 2005; Sasaki, Caupin, and Balibar, 2008; Haziot *et al.*, 2013a). The cell contains two parallel, transversely polarized lead zirconate titanate (PZT) piezoelectric transducers, mounted with their piezoelectric shear axes vertical. Oriented single crystals of ^{4}He were grown in a 0.7 mm wide vertical slit between the two transducers and their shear modulus is measured using the same technique as described in Sec. V.B. The sensitivity and the stability of this setup allow measurements to be made for strains ϵ in the range 10^{-10} to 10^{-6} and for stresses as small as 10^{-9} bar. The transducers were carefully calibrated to give an absolute measurement of the shear modulus in the crystallographic direction perpendicular to the transducer polarization. Using a lock-in amplifier, both the amplitude of the shear modulus and the dissipation can be measured at frequencies between 1 Hz and 20 kHz.

1. Elastic constants and basal glide of dislocations

Figure 34 shows measurements by Haziot *et al.* (2013a) of the shear modulus for a crystal oriented with its sixfold symmetry axis (the c axis of the hcp structure) nearly vertical. This particular crystal was grown using isotopically purified ^{4}He with a ^{3}He concentration of 0.4 ppb. Around 0.2 K, dislocation motion reduces the elastic modulus by 43% from its intrinsic value of 127 bar (calculated from the ultrasonically measured high temperature elastic constants in Table I). The large shear modulus reductions like that seen around 0.2 K were referred to as "giant plasticity" but, despite their dislocation origin, they had most of the features of elasticity. The softening occurred at strains as small as $\epsilon \sim 2 \times 10^{-11}$ (corresponding to stress $\sigma \sim$ nbar) and the response was

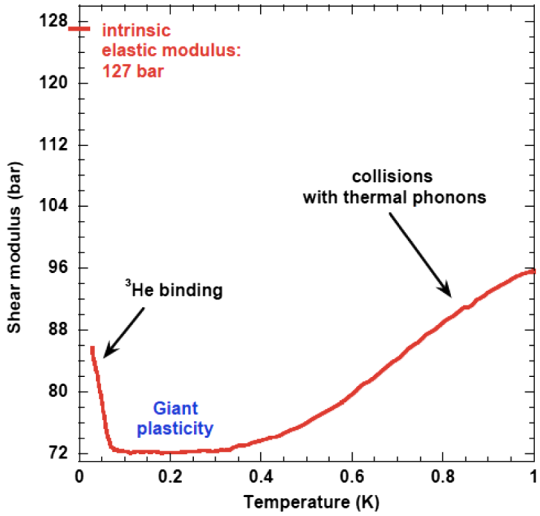

FIG. 34. In a temperature domain of around 0.2 K, this isotopically pure crystal shows giant plasticity: its shear modulus (measured at a frequency of 9 kHz) is highly reduced with respect to its intrinsic value (127 bar, indicated by the red bar on the vertical axis).

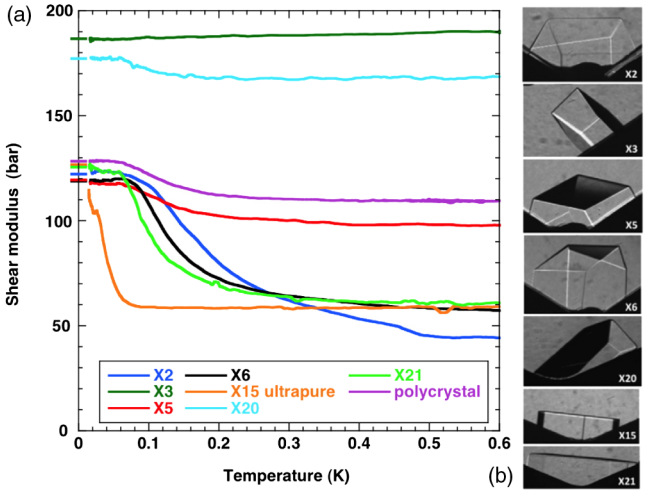

FIG. 35. Shear modulus for hcp ^{4}He single crystals. The photographs on the right show the orientations (from top to bottom) of crystals X2, X3, X5, X6, X20, X15, and X21. The top green curve that shows no softening is for crystal X3. Data from crystal X20 lie directly below this (light blue line) and show a small softening. The next curve below (purple line) is for a polycrystalline sample and shows similar softening to crystal X20 and to crystal X5 immediately below it (red line). Crystal X2 (dark blue line) has the largest high temperature softening. Two other crystals X6 (black) and X21 (green) have intermediate, nearly identical softening. The final curve, for which softening occurs at much lower temperature, is for crystal X15, which was grown from ^{4}He with a ^{3}He concentration of 4×10^{-10}. The other crystals were all grown from natural ^{4}He gas containing 2.5×10^{-8} of ^{3}He impurities. From Haziot *et al.*, 2013a.

essentially linear and reversible. This indicates that the Peierls barrier for dislocation motion is extremely small, perhaps zero, for the dislocations responsible for shear softening in hcp ^{4}He. The modulus increase below 0.1 K was due to ^{3}He impurities binding to dislocations and limiting their motion. Above 0.3 K, dislocation motion was damped by collisions with thermal phonons. These processes introduce frequency dependence and dissipation into the crystal's mechanical response, behavior that is sometimes referred to as "anelasticity" (Nowick and Berry, 1972). The macroscopic irreversibility and hysteresis that are commonly associated with plasticity occur at much larger strains where new dislocations are created.

This behavior can be compared to that of classical crystals, where dislocations move only at high enough temperature and under sufficiently large stress. This is because dislocation lines can overcome the periodic lattice's Peierls barriers only by thermal activation of point defects (kinks or jogs) or at large stresses that reduce the barrier height. Dislocation motion in classical crystals induces only a small softening that is highly dependent on temperature and stress amplitude, in contrast to ^{4}He, where the softening is large and, in the absence of impurities, independent of temperature below 0.3 K.

Figure 35 shows the measured shear modulus for a number of crystals with different orientations. Crystal X15 was grown from the same isotopically purified ^{4}He ($x_3 = 0.4$ ppb) as the crystal in Fig. 34, but the others were grown from commercial ^{4}He gas with a ^{3}He concentration of 25 ppb. In the isotopically purified crystals, the remaining 0.4 ppb of ^{3}He impurities was not sufficient to completely pin the dislocations, even at the lowest temperature of 15 mK. For the other crystals, there were enough ^{3}He impurities to immobilize all the dislocations and recover the crystal's intrinsic elastic modulus below 60 mK. The intrinsic shear modulus depends strongly on the crystal orientation since it is a function of all the elastic constants C_{ij}, but it could be calculated explicitly since the crystal's orientation with respect to the deformation direction was known from the growth facets shown at the right of Fig. 35. The colored ticks on the left vertical axis indicate these intrinsic values, which agree with the low temperature values for the crystals grown from commercial ^{4}He gas, confirming that 25 ppb of ^{3}He is sufficient to completely pin the dislocations. Note that the crystal X3, whose c axis was tilted by 45° from the vertical, had the intrinsic shear modulus value with no measurable temperature dependence and was used by Haziot *et al.* (2013a) to calibrate their transducers.

The elasticity tensor of hexagonal crystals like hcp ^{4}He contains five independent elastic coefficients. Among these, the coefficient C_{66} is associated with deformations of the hexagonal symmetry in these basal planes [shown in Fig. 36(a)], while the coefficient C_{44} relates the shear stress and strain associated with basal planes gliding past each other [the deformations shown in Figs. 36(b) and 36(b′)]. For crystals like X3 that are oriented at 45°, the measured shear modulus is essentially independent of both C_{44} and C_{66}, so the temperature-independent modulus shown in Fig. 35 suggests that one of these coefficients is responsible for the softening seen in other crystals. By analyzing the shear modulus changes for other crystal orientations, Haziot *et al.* (2013a) showed that it is C_{44}, not C_{66}, that changes. The data for all the single crystals was consistent with C_{44} softening by approximately 60%, as shown in Fig. 37, and all other elastic constants remaining constant. This behavior was attributed to

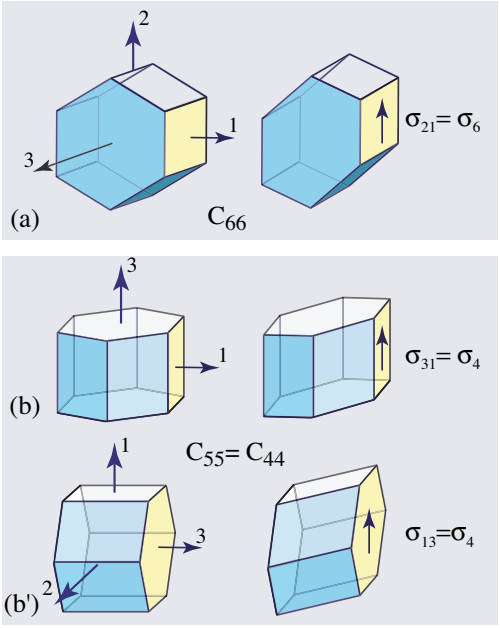

FIG. 36. Stresses and strains for shear deformations in hexagonal crystals. (a) Deformation of the hexagons in the basal planes, with stress σ given by the corresponding elastic constant C_{66}. (b), (b′) Cases that occur when the hexagonal basal planes slide past each other, with stress given by the elastic constant C_{44}. From Balibar *et al.*, 2016.

the fact that dislocations have preferential glide directions. A reduction in C_{44} means that the dislocations responsible for the softening must glide either parallel to the basal planes or along the prismatic planes parallel to the c axis. In close-packed hexagonal materials, dislocations usually glide most easily in the basal plane (Hull and Bacon, 2011). Legrand (1984) explained that this is due to the splitting of edge dislocations into two partial dislocations because the stacking fault energy is extremely small for the close-packed basal planes. Such split dislocations are really "atomic ribbons" rather than 1D lines, and they glide easily parallel to the ribbon plane. This easy basal glide is observed in many hexagonal metals (Be, Mg, Co, Zn), although in some others (Zr, Ti) glide occurs along prismatic planes. Such conventional crystals do show behavior associated with dislocation glide at high temperatures, but dislocation effects are complicated by many other phenomena. The elastic changes due to dislocations are much clearer in ^{4}He crystals. The softening can be extremely large: Souris *et al.* (2015) observed reductions in C_{44} of up to 90% in some cases.

Another unique feature of solid helium is the possibility of removing all impurities from ^{4}He crystals. Even isotopic impurities (^{3}He) can be removed using a method reminiscent of the classical "zone melting" used to purify metals and semiconductors. It is based on the fact that impurities are usually more soluble in the liquid than in the solid, where the strain field around each impurity adds elastic energy. In the case of ^{4}He, the difference in potential energy between the liquid and the solid has been calculated as −1.359 K per ^{3}He atom (Edwards and Balibar, 1989; Pantalei *et al.*, 2010), so in equilibrium all the ^{3}He impurities are trapped in the liquid phase if the temperature is low enough. During cooling, gently shaking the dislocations by applying an oscillating stress helps prevent ^{3}He impurities from binding to dislocations so that they are free to diffuse out of the solid. Figure 38 shows that when impurities were initially bound to dislocations at low temperature (crystals X2, X5, and X6), applying an oscillating strain larger than a few microbars detached the impurities, allowing dislocations to move and reducing the shear modulus. This stress threshold is larger when increasing the stress than when decreasing it, leading to hysteresis when the stress amplitude was cycled. For crystal X4, where the impurities were detached before cooling, the shear modulus was reduced by 80% from its intrinsic value and stayed at this low value

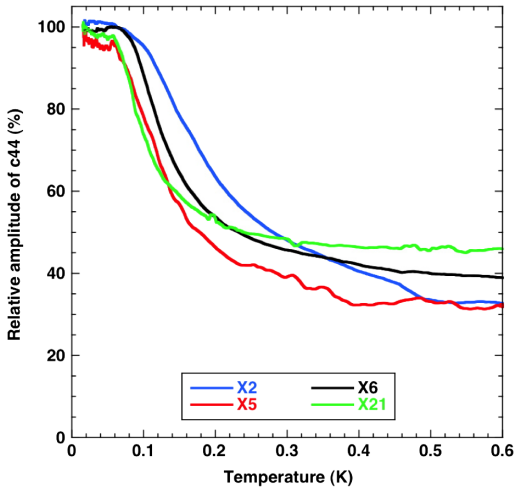

FIG. 37. Variation of C_{44} for four of the single crystals whose shear modulus is shown in Fig. 35, calculated from the data using the known crystal orientations and assuming that all other elastic constants remain constant.

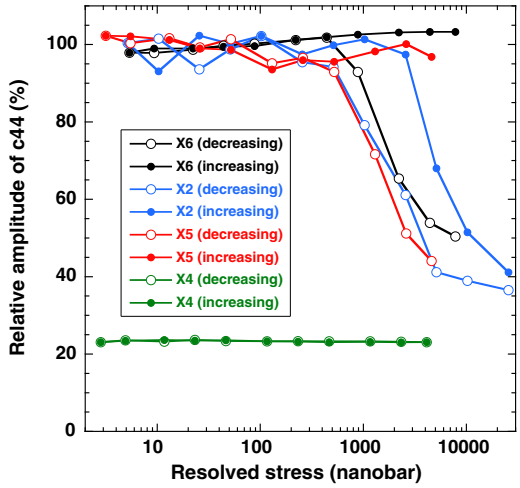

FIG. 38. Normalized shear elastic constant C_{44} for four single crystals at 20 mK as a function of the resolved stress projected on the basal plane. Above a threshold stress of a few microbars, dislocations break away from ^{3}He impurities. Crystal X4 (the lowest green curves) was free of ^{3}He impurities, since they were detached prior to cooling, and thus remained soft over the entire range of stress, with no hysteresis. From Haziot *et al.*, 2013a.

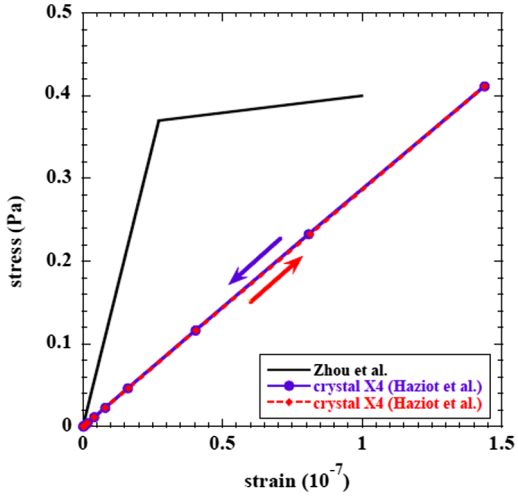

FIG. 39. Stress-strain diagram for crystal X4 (the same data as in Fig. 38), showing reversible linear behavior with a slope corresponding to a shear modulus reduced by 80%. The black line illustrates the nonlinear elastic or plastic behavior expected for classical crystals. From Haziot *et al.*, 2013b.

when the applied stress was cycled. Figure 39 shows the linear stress versus strain curve for this impurity-free crystal, with a slope corresponding to the reduced shear modulus with high mobility dislocations. This contrasts with the nonlinear plastic behavior of classical crystals, which retain their intrinsic defect-free elasticity at low stresses and have a reduced modulus when the stress exceeds the Peierls stress for dislocation motion.

The low temperature softening of crystal X4 in Figs. 38 and 39 shows that, in the absence of ^{3}He impurity pinning, dislocations glide freely in the basal plane down to the lowest applied shear strains ($\sim 3 \times 10^{-11}$). This corresponds to an extraordinarily small Peierls stress (the minimum shear stress for dislocation glide at zero temperature) of less than ~0.3 mPa (3 nbar). Small yield stresses are often observed in hcp and fcc metals, where they are due to dissociated dislocations gliding in close-packed directions (Suzuki, Takeuchi, and Yoshinaga, 2013). However, only upper limits could be placed on the Peierls stresses in those materials since impurity pinning immobilized the dislocations at low temperatures. The smallest observed yield stress (in copper crystals) was 0.28 MPa, corresponding to $\sigma_P/\mu < 7 \times 10^{-6}$ (Kamimura, Edagawa, and Takeuchi, 2013), although some dislocation motion, often referred to as "preyield microplasticity," was seen at slightly lower stresses (Suzuki, Takeuchi, and Yoshinaga, 2013). For the high purity hcp ^{4}He crystal X4, the measurements put an upper limit on the Peierls stress that is 9 orders of magnitude smaller than the experimental limits for metals. Part of the difference is due to helium's smaller elastic constants, but even when the Peierls stress is scaled by the shear modulus, σ_P/μ is still less than 2×10^{-11} for hcp ^{4}He, more than 5 orders of magnitude smaller than the corresponding upper limit for metals.

PIMC simulations (Borda, Cai, and Koning, 2016) confirm that the dislocations that glide in the basal plane of hcp ^{4}He split into partials with rather large core widths (about four lattice spacings for the edge dislocation partials). They found that both the edge and screw dislocations glide easily but the simulations involved much larger effective stresses than those shown in Figs. 38 and 39 and thus could not confirm the extraordinarily small Peierls stresses extracted from shear modulus experiments. The measured Peierls stress limit of 0.3 mPa corresponds to an energy barrier (Peierls energy per unit length) $E_P = (b^2/2\pi)\sigma_P \approx 5 \times 10^{-24}$ J/m (Hull and Bacon, 2011). This suggests that a 100 μm long dislocation segment would be thermally excited over the Peierls barrier even at microkelvin temperatures. Of course, glide is expected to occur via motion of geometric or thermally excited kinks along the dislocation, not by moving an entire dislocation over the Peierls barrier. The observed mobility of dislocations at low stresses presumably corresponds to the much smaller Peierls barrier for kink motion. Since the experimental values of the Peierls stress in solid helium are only upper limits, it is possible that quantum effects completely delocalize kinks and dislocations, i.e., reduce the Peierls barrier to zero.

2. Phonon damping, dislocation lengths, and impurity motion

To better understand the dislocation motion, Haziot *et al.* (2013a), Haziot, Fefferman, Souris *et al.* (2013), Fefferman *et al.* (2014), and Souris *et al.* (2015) measured the dissipation $1/Q$ of hcp ^{4}He crystals as functions of temperature, frequency, and strain amplitude. The shear modulus increase seen in Fig. 34 at temperatures above 0.3 K was attributed to the damping of dislocations due to scattering of thermal phonons, which introduces a dislocation relaxation time $\tau = BL^2/\pi^2 C$ in the expressions for both the modulus and the dissipation [Eqs. (15) and (16)]. The dominant fluttering mechanism for phonon scattering gives a damping force $B = gT^3$, so for the elastic constant C_{44} the low frequency shear modulus expression of Eq. (13) is

$$\frac{\delta C_{44}}{C_{44}^0} = \frac{\alpha \Lambda L^2}{1 + \alpha \Lambda L^2}, \tag{17}$$

and the corresponding dissipation of Eq. (14) becomes

$$\frac{1}{Q} = \frac{\alpha \Lambda L^2}{1 + \alpha \Lambda L^2} g L^2 \omega T^3. \tag{18}$$

As usual, Λ is the density of dislocation lines per unit volume and L is a typical length between nodes in the dislocation network, while $\alpha = 0.019$ and $g = 905\ \mathrm{s\,m^{-2}\,K^{-3}}$ are the calculated values for hcp ^{4}He at low densities (Souris *et al.*, 2014).

Figure 40 shows the measured dissipation in a hcp ^{4}He crystal at temperatures above 0.3 K and frequencies of 1.5, 3, and 9 kHz (Haziot, Fefferman, Beamish, and Balibar, 2013). The measurements were made at relatively large strains ($\epsilon = 10^{-7}$) to suppress the effects of ^{3}He impurity pinning. The initial slopes agreed remarkably well with the predicted ωT^3 behavior, clear confirmation of the phonon scattering mechanism for dislocation damping in helium. Deviations from linear behavior, like those above $\omega T^3 \gtrsim 10^4\ \mathrm{K^4\,rad/s}$, reflect the breakdown of the low frequency approximation

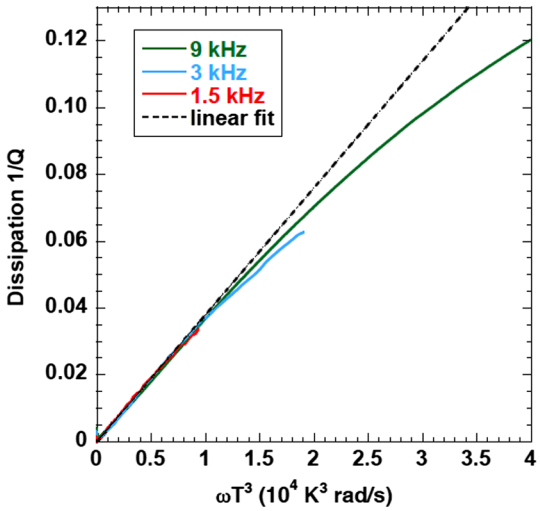

FIG. 40. Dissipation $1/Q$ in hcp ^{4}He, at a strain $\epsilon = 10^{-7}$ vs ωT^3. The frequency-independent linear region for small ωT^3 is the expected behavior for dislocation damping by scattering of thermal phonons via the fluttering mechanism; the dashed black line is a linear fit to the small ωT^3 data. The 9 kHz data (green line) extend over the full range of the graph; the 3 kHz (blue line) and 1.5 kHz (red line) data extend to about 2×10^4 and 0.9×10^4 K^3 rad/s, respectively.

$\omega\tau \ll 1$. Fefferman *et al.* (2014) were able to fit the entire dissipation and shear modulus curves by using the full expressions [Eqs. (15) and (16)] and integrating over a distribution of dislocation lengths L. However, even when we assume a single dislocation length L, the initial linear region gives important information about the dislocation network. Because the modulus softening and the dissipation have different dependences on the dislocation length (L^2 and L^4, respectively) and the phonon damping is known, the dislocation network's density Λ and length L can be determined separately, something not possible from low frequency modulus measurements alone. Haziot, Fefferman, Beamish, and Balibar (2013), Haziot, Fefferman, Souris *et al.* (2013), Fefferman *et al.* (2014), and Souris *et al.* (2015) found dislocation densities Λ between 10^4 and 10^6 per cm^2, rather small values that confirm the high quality of their single crystals. Their dislocation lengths L were extremely large, between 63 and 230 μm. These values are nearly macroscopic and are much larger than expected for a simple three-dimensional network of dislocations. For example, if dislocations form a regular cubic lattice, Λ and L are related by the simple relation $\Lambda L^2 = 3$. For any three-dimensional lattice of dislocations, the dislocation density Λ should be of the order of $1/L^2$. The experiments of Haziot, Fefferman, Souris *et al.* (2013) showed that this is not the case. In their 2013 experiment the product ΛL^2 ranged from 17 to 57. When Souris *et al.* (2015) tried to grow even better quality crystals, they found ΛL^2 values up to 471.

These extremely large values of ΛL^2 imply that the dislocations do not form a simple 3D network. They must avoid intersections by forming 2D arrays of parallel lines called "sub-boundaries." Friedel (1964) explained that the formation of such sub-boundaries can produce a large softening since the aligned dislocations in sub-boundaries can glide in the basal planes in a cooperative way. For 3D dislocation networks, on the other hand, the maximum softening is ~10%, much smaller than the 90% changes seen by Souris *et al.* (2015).

The shear softening in the direction parallel to the hcp basal planes is analogous to that of a stack of sheets of paper, which is easy to deform in directions where the sheets slide past each other, but stiff in other directions in which the individual sheets would have to deform. Of course, in hcp crystals the entire atomic planes do not slide, but instead the movement occurs near dislocations. Furthermore, between paper sheets or in classical crystals, there is friction so that the deformation in response to stress is nonlinear but, as shown in Fig. 40, in the absence of impurities the dissipation associated with the shear deformation in ^{4}He approaches zero at low temperature. One possible explanation of this nonclassical behavior is that quantum fluctuations make the kink energy vanish so that dislocation lines can move freely despite the periodic lattice potential. Another possibility is that kinks have a nonzero energy but the grown-in "geometric kinks" move along dislocations by quantum tunneling through an extremely small Peierls barriers. It would be hard to distinguish experimentally between the two possibilities.

We discussed the dissipation above 0.3 K, where it is a consequence of dislocations' interactions with thermal phonons. Below 0.2 K, a different dissipation mechanism becomes important when ^{3}He impurities are present. These progressively bind to dislocations as the temperature decreases. In single crystals, there is a clear dissipation associated with ^{3}He, as shown in Fig. 41 (Haziot, Fefferman, Souris *et al.*, 2013). When impurities start binding, the dislocation motion decreases, stiffening the crystal, and the dissipation increases. It reaches a peak at a temperature T_p near the midpoint of the modulus stiffening, and it vanishes at lower temperatures where the dislocations are fully immobilized.

Knowing the density and typical length of dislocations in their crystals, Haziot, Fefferman, Souris *et al.* (2013) could determine the dislocations' displacements and maximum speeds at their midpoints for a given strain amplitude and frequency. The semilog plot of Fig. 42 shows the maximum speeds versus the inverse of the dissipation peak temperatures T_p. There are two different regimes. At high speeds, the peak temperature is independent of speed, behavior that is also seen at high frequencies in the shear modulus data of Fig. 41. This is the expected behavior if impurities act as static pinning points: they cannot move fast enough to follow the dislocations' motion, so they anchor the dislocations, giving a frequency-independent shear modulus softening and a reduced dissipation peak. However, at low speeds below 45 μm/s, the constant slope on this Arrhenius plot reflects a thermally activated regime in which the dislocation motion decreases exponentially as impurities bind at low temperatures. This means that ^{3}He atoms are dragged along with dislocations but the motion of the dislocations dressed with impurities is damped. Assuming that this damping force is proportional to the density of bound ^{3}He, the slopes of the semilog plots of Fig. 42 give the binding energy E_B of ^{3}He

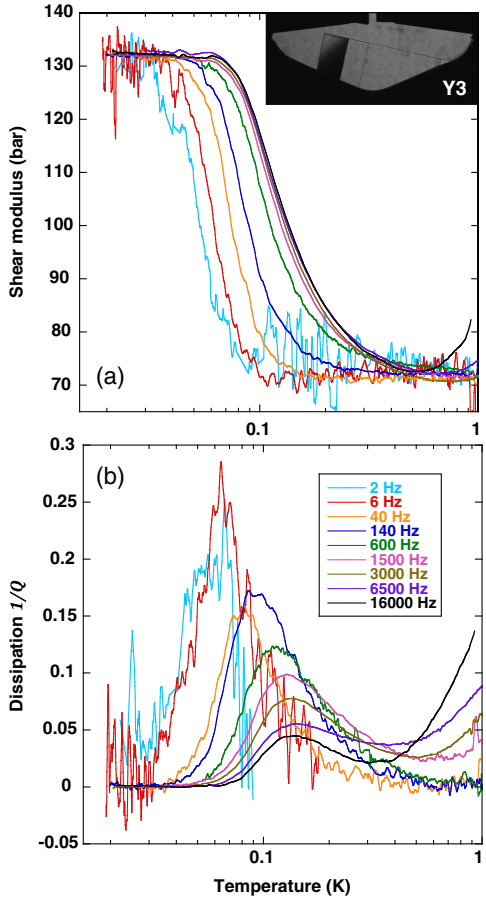

FIG. 41. Temperature variation of the low amplitude (a) shear modulus and (b) dissipation in hcp ^{4}He at the frequencies from 2 Hz to 16 kHz indicated in the inset. The transition from stiff (at low T) to soft (at higher T) and the accompanying dissipation peaks are associated with binding of ^{3}He impurities to dislocations. The shear softening and the associated dissipation peaks shift monotonically to higher temperatures as the frequency increases. From Haziot, Fefferman, Souris *et al.*, 2013.

impurities to the dislocation lines, $E_B = 0.67$ K for this crystal. The same binding energy was found in subsequent measurements by Fefferman *et al.* (2014). In a more detailed study, Souris *et al.* (2014) confirmed that the dissipation was proportional to the ^{3}He concentration by comparing the behavior of crystals grown from ^{4}He gas with three different impurity concentrations, with x_3 equal to 2.5×10^{-8}, 3.8×10^{-7}, and 2.32×10^{-6}, respectively. Figure 43 shows the relaxation times determined at the dissipation peak temperatures, where $\omega\tau = \sqrt{1 + \alpha\Lambda L^2}$ (Fefferman *et al.*, 2014). The ^{3}He binding energies from the slopes for different crystals vary from 0.6 to 0.71 K, which is consistent with previous values. The ~0.1 K scatter in the slopes that can be seen in Fig. 43 is within the width of the binding energy distribution found in experiments on polycrystalline ^{4}He (Syshchenko, Day, and Beamish, 2010; Mukharsky and Penzev, 2012).

Fefferman *et al.* (2014) determined the distribution of network lengths in a single crystal by measuring the strain dependence of the shear modulus at low temperature.

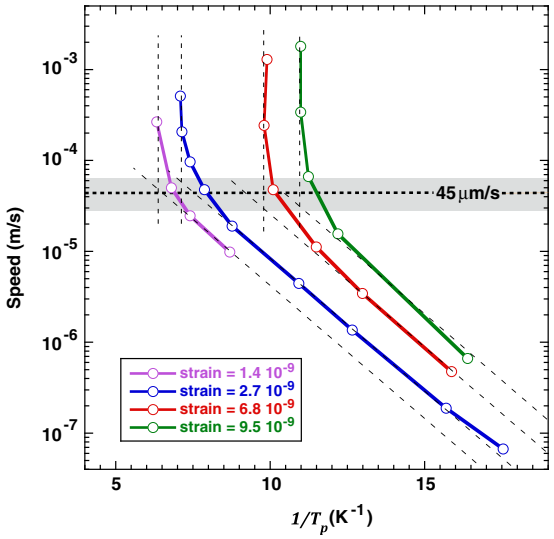

FIG. 42. Maximum dislocation speeds for dislocations, calculated from the length between nodes of their network and the strain amplitude and frequency. From left to right, the curves correspond to strains of 1.4×10^{-9} (purple), 2.7×10^{-9} (blue), 6.8×10^{-9} (red), and 9.5×10^{-9} (green). Two regimes appear: below 45 μm/s, the bound ^{3}He impurities move with the dislocations; above this critical speed, ^{3}He impurities cannot follow the dislocations and act as static pinning sites (see the text).

By applying a large oscillating strain ($\epsilon = 10^{-6}$) while cooling from 0.5 K, they prevented the ^{3}He impurities from binding to dislocations. When the strain amplitude was then reduced at 25 mK, ^{3}He impurities began to bind, increasing the shear modulus as shown in Fig. 44. If there were a single network pinning length, there would be a precise value of the applied strain at which all dislocations would get pinned and the shear modulus would suddenly increase to the intrinsic value. However, short dislocations move less than long ones and their breakaway stress is larger, so ^{3}He impurities

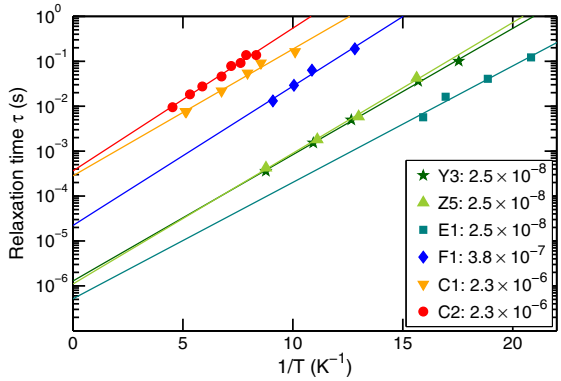

FIG. 43. Arrhenius semilog plot of the relaxation time τ of dislocations vs the inverse temperature $1/T$ for crystals with different orientations and with the impurity concentrations indicated in the inset. Slight variations in slope show that there is a narrow distribution in the binding energy E_B of ^{3}He impurities to dislocations (see the text). From Haziot, Fefferman, Souris *et al.*, 2013

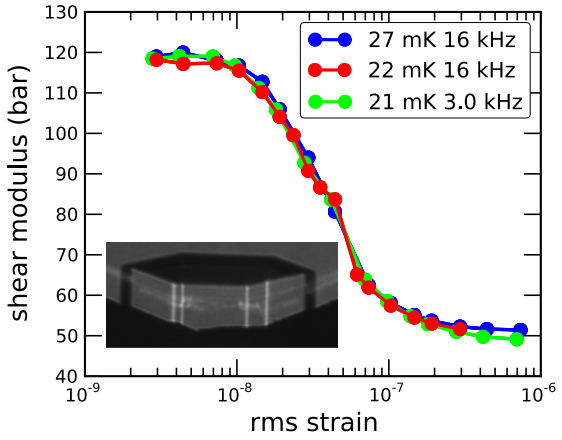

FIG. 44. Shear modulus of a hcp ^{4}He single crystal near 25 mK, measured while decreasing the driving strain. The distribution of dislocation lengths between nodes of the network is determined by analysis of the transition between the unpinned soft state at large strain and the stiff intrinsic state at low strain. From Fefferman *et al.*, 2014.

progressively bind to and pin dislocations as the driving strain is reduced, beginning with the shortest ones. The smooth transition from soft to stiff that one sees in Fig. 44 is evidence that there is a distribution of lengths. From the shape of the transition Fefferman *et al.* (2014) found a broad distribution of network lengths, extending at least from 20 to 300 μm in this crystal. However, since a dislocation's contribution to the shear modulus is proportional to L^2, elastic measurements are not sensitive to shorter dislocations and there may be significant numbers of dislocations shorter than 20 μm.

When Fefferman *et al.* (2014) tried to fit low amplitude modulus and dissipation datasets like those shown in Fig. 41, using their measured distribution of network lengths they found that they also had to include a distribution of ^{3}He binding energies. To achieve good fits, they needed a width of the order of 0.1 K around the average value (about 0.7 K), which is consistent with the distribution of binding energies from Fig. 43 (Souris *et al.*, 2014). A distribution of binding energies is expected because dislocations rarely have purely edge or purely screw character. Depending on their orientation in the lattice, they can have a mixed character and the binding energy can vary between the value for an edge dislocation and that for a screw dislocation, which is expected to be smaller.

VI. PLASTIC DEFORMATION AND FLOW

The previously described shear modulus behavior occurs at extremely small stresses and strains, where conventional solids normally deform elastically, but it involves the motion of dislocations, which are normally associated with plastic deformation. Although the large modulus changes were described as giant plasticity, the dislocation strain is proportional to the applied stress and returns to zero when the stress is removed. Such linear reversible behavior is more typical of elastic deformations. However, dislocation damping and pinning affects the dislocations' mobility and introduces dissipation and frequency dependence in the response. Such behavior is sometimes referred to as "anelastic," reserving the term "plastic deformation" for much larger deformations above the solid's yield point, where the crystal does not return to its original configuration when the stress is removed. This irreversible behavior involves the creation, multiplication, and interaction of dislocations, not just the dislocation glide used to describe the shear modulus softening (giant plasticity) in solid helium. Zhou *et al.* (2013) included these features in a model for solid helium to describe its plastic deformation in this regime. There can also be an intermediate region below the macroscopic yield point, often referred to as "microplasticity" (Maass and Derlet, 2018), in which the existing dislocations move but not reversibly because they intersect with nearby dislocations and create jogs or other pinning points, without creation of significant numbers of new dislocations. In this section, we describe experiments on plastic deformation and flow of solid helium at large strains.

Dislocation glide and plastic deformation are responses to shear stresses. Purely hydrostatic pressure changes do not produce shear strains and therefore do not result in plastic deformation. The measurements on single crystals described in Sec. V.C involved uniform simple shear, but shear deformations are also generated by pressure gradients, by tensile strains in Young's modulus measurements, and by uniaxial compression in longitudinal sound waves. For solid helium confined at constant density in a rigid cell, thermal expansion increases the pressure when a sample is heated, but if the thermal expansion is isotropic, as in cubic crystals, the pressure change is hydrostatic and no plastic deformation is expected. In hexagonal crystals, the thermal expansion coefficients parallel and perpendicular to the c axis are different, so warming or cooling a confined hcp helium crystal produces shear stresses that can plastically deform it. These stresses are small in hcp ^{4}He since its c/a ratio is nearly independent of pressure, i.e., its thermal expansion is nearly isotropic (Franck and Wanner, 1970). However, in imperfect crystals there are microscopic regions of shear stress around defects and, even in cubic crystals, temperature changes can create prismatic dislocation loops if thermal vacancies precipitate into platelets (Hull and Bacon, 2011).

The first attempt to observe macroscopic plastic flow in solid helium involved growing a hcp ^{4}He crystal around a magnetically levitated metal sphere (Andreev *et al.*, 1969), which was then subjected to a magnetic force of up to 250 times its weight. The ball's position was measured using an optical technique with a resolution of 20 μm. At 0.5 K no displacement was seen, putting an upper limit of 2 nm/s on the ball's velocity. Subsequent measurements using larger forces and more sensitive displacement measurements succeeded in detecting the plastic deformation of solid helium. Beginning in the 1970s, several groups applied metallurgists' standard techniques (stress-strain curves, hysteresis loops, yield stresses, and rate-dependent creep) to the study of the plastic deformation and flow of solid helium at higher temperatures.

A. High temperature plastic flow and creep

Suzuki (1973, 1977) made the first systematic measurements of plastic deformation of solid helium. A ball or cylinder was embedded in the helium and an attached wire

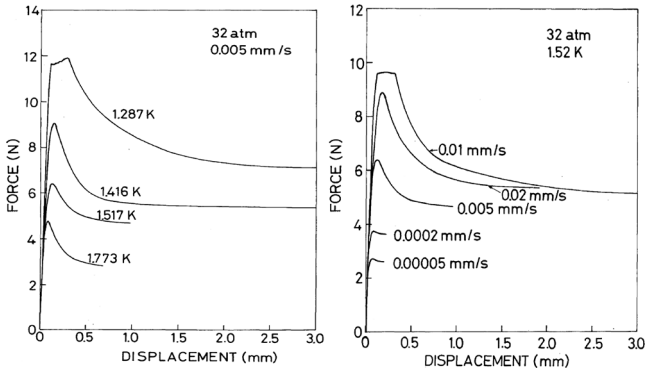

FIG. 45. Stress-strain (force-displacement) curves for hcp ^{4}He at a pressure of 3.2 MPa. Left panel: temperature dependence at a shear strain rate $\dot{\epsilon} \sim 2 \times 10^{-3}/\mathrm{s}$. Right panel: strain rate dependence at a temperature of 1.52 K. From Suzuki, 1977.

was used to pull it through the helium while measuring the displacement and applied force. Figure 45 shows typical force-displacement curves for hcp ^{4}He. The corresponding shear stresses and strains can be roughly estimated from the geometry of the cell. The force (stress) initially increases, with a slope corresponding to elastic deformation of the helium, then drops by as much as 40% above the helium's yield point. The solid then continues to deform at lower stress. The yield stress and the magnitude of the yield drop are smaller at higher temperatures and for smaller strain rates $\dot{\epsilon}$. At a shear strain rate $\dot{\epsilon} \sim 2 \times 10^{-3}/\mathrm{s}$ (corresponding to a displacement of the cylinder at 0.005 mm/s) and a temperature of 1.5 K, yield begins at a shear stress (strain) $\sigma \sim 13$ kPa ($\epsilon \sim 0.04$). Above its yield point, the helium continues to deform, at roughly constant flow stress ($\sigma \sim 10$ kPa at $T = 1.5$ K for $\dot{\epsilon} \sim 2 \times 10^{-3}/\mathrm{s}$), with no indication of work hardening even when the helium is deformed by 100%. This suggests that the steady flow involves dislocations being created, piling up at grain boundaries and walls and then being annihilated via climb. Suzuki found that the creep rate at small stresses was thermally activated, as expected since this process, known as Weertman creep, is controlled by the vacancy diffusion required for dislocation climb (Weertman, 1955; Poirier, 1985). For samples at 3.2 MPa (molar volume 20.5 cm^3), Suzuki found an activation energy of 19.5 K, which is consistent with activation energies for vacancy diffusion in hcp ^{4}He measured with other techniques (Fraass, Granfors, and Simmons, 1989). The pronounced yield drops were attributed to high Peierls stresses for dislocations with Burgers vectors not lying in the hcp basal plane. Plastic deformation in complex geometries, or in polycrystalline samples, requires slip in multiple directions and is controlled by the slip system with the largest Peierls stress.

The same technique was used to study plastic deformation in bcc ^{3}He (Sakai, Nishioka, and Suzuki, 1979). Flow stresses were smaller in low density crystals, e.g., $\sigma \sim 1$ kPa at $T = 0.6$ K for $\dot{\epsilon} \sim 2 \times 10^{-3}$ in crystals at pressures around 3.5 MPa. This is consistent with the smaller vacancy activation energies in bcc ^{3}He. In addition, plastic flow around an embedded object should be easier for bcc crystals since dislocations can move in multiple slip planes, in contrast to hcp crystals, where slip is confined to the basal plane.

Sanders *et al.* (1977) used a somewhat different technique in which a piston driven by a pressurized bellows was used to compress and deform single crystals of solid ^{4}He. A thin surface layer could be melted, largely eliminating the need for multiple slip systems since such unconstrained crystals were free to shear at the cell walls. Figure 46 shows stress-strain curves for a hcp ^{4}He crystal at a compressional strain rate $\dot{\epsilon} = 10^{-4}/\mathrm{s}$. For the unconstrained crystal (solid circles), the flow stress was too small to measure, less than 5 kPa. For the constrained crystal (open circles), flow occurred at a uniaxial stress of about 60 kPa. In contrast to the measurements of Suzuki (1973, 1977), these experiments showed no evidence of a yield drop. After the deformation ended, the stress relaxed (open triangles) but a residual stress of about 20 kPa remained for at least 20 min. Given the complicated deformation geometry, which involved compression of the solid as well as complex flow around the piston, it is difficult to convert these uniaxial stresses to the corresponding shear stresses relevant for plastic deformation. The experimental cell included ultrasonic transducers, which allowed Sanders *et al.* (1977) to monitor the density of dislocations via their contribution to the sound attenuation. In both the constrained and unconstrained crystals, the attenuation increased rapidly when deformation began, indicating that plastic deformation was accompanied by the expected dislocation multiplication.

Experiments on bcc ^{4}He crystals (Sanders *et al.*, 1978) showed somewhat different behavior. The deformation of constrained samples was similar to that for hcp ^{4}He, although the flow stresses were several times smaller. For unconstrained samples the flow stress was again too small to measure. However, there was essentially no increase in ultrasonic attenuation associated with deformation of bcc crystals. This suggests either that bcc crystals deform via mechanisms that do not involve dislocation multiplication or that any dislocations created do not contribute to ultrasonic attenuation. The difference between hcp and bcc crystals was

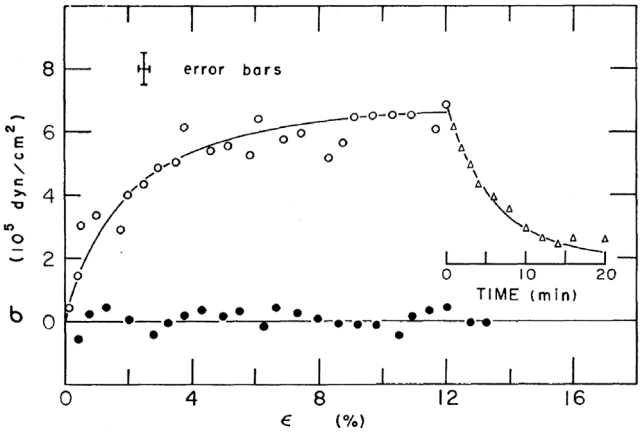

FIG. 46. Stress-strain curves for constrained (open circles) and unconstrained (solid circles) crystals of hcp ^{4}He at a pressure of 3.2 MPa and a temperature of 1.8 K. Open triangles show the stress relaxation when the strain is held constant. From Sanders *et al.*, 1977.

confirmed in measurements on bcc ^{3}He (Manning, Moelter, and Elbaum, 1986), which also deformed easily, without significant sound attenuation changes in most of the crystal.

Plastic deformation has also been studied by electromagnetically pulling a 80 μm diameter superconducting wire through bcc ^{4}He (Berent and Polturak, 1998). For stresses below about 0.6 kPa, the wire's velocity was linear in applied stress and its temperature dependence was consistent with the activation energy of thermal vacancies. This suggests that the flow was due to vacancy diffusion (Nabarro-Herring creep). For larger forces, the velocity depended nonlinearly on stress and appeared to involve dislocation motion controlled by thermally activated climb. This technique has been extended to temperatures as low as 10 mK, but the stresses were not large enough to generate motion below 1 K (Ahlstrom *et al.*, 2014). In hcp ^{4}He above 1 K, the 55 μm diameter wire moved in a series of apparently random jumps. These involved large displacements ($\sim$0.1 mm) at speeds up to $\sim$1 mm/s. In the bcc phase at high temperature, the wire moved much more slowly ($\sim$ nm/s), but smoothly, as in the earlier experiments of Sanders *et al.* (1978).

The previously described plastic deformation measurements were made near samples' melting points, where thermal processes control plastic deformation. Recent experiments (Cheng and Beamish, 2018b) have extended the piezoelectric techniques developed for low frequency shear modulus measurements to much larger strains. The large strains required for plastic deformation were achieved by using a stack of 18 transducers and increasing the drive voltage from millivolts to hundreds of volts. Uniform shear strains of up to 0.4% could be produced, at constant strain rates generated by applying a linear voltage ramp to the transducer stack. The shear stress in the helium was measured *in situ* with a piezoelectric transducer, giving a sensitivity orders of magnitude higher than was possible with the mechanical systems used in earlier plastic deformation experiments. The uniform shear strains in this simple geometry allowed stress-strain curves to be quantitatively interpreted and the method could be used at much lower temperatures, so plastic deformation of solid helium could be studied in the nonthermal regime.

Figure 47 shows measured stress-strain loops for polycrystalline hcp ^{4}He at 3.4 MPa, at temperatures of 25 (solid lines) and 900 mK (dashed lines). Starting at zero deformation, the strain was ramped at a constant rate $\dot{\epsilon} = 8 \times 10^{-6}$ s^{-1} to a maximum value $\epsilon = 0.065\%$. It was then ramped in the opposite direction at the same rate, to $\epsilon = -0.065\%$, and finally back to zero. At 25 mK (solid lines), the stress-strain response was essentially linear and reversible and the stress returned to zero, the behavior of an elastic solid. At 900 mK (dashed lines), the stress deviated from the elastic value for strains larger than 0.01% and followed a different path when the strain was ramped down. The resulting stress-strain loop did not close at its starting point, the irreversible and hysteretic behavior that characterizes plastic flow.

Figure 48 gives an overview of high temperature plastic flow (creep) in a polycrystalline hcp ^{4}He sample. Figure 48(a) shows the helium's differential shear modulus $\mu_{\rm diff} = d\sigma/d\epsilon$ at temperatures of 0.5 and 0.9 K. Integrating $\mu_{\rm diff}$ gives the corresponding stress σ shown in Fig. 48(b). Figures 48(c) and 48(d) show the corresponding behavior at 1.2 K. For small strains, the stress is proportional to the strain, so $\mu_{\rm diff}$ is constant. At 0.5 K, the elastic regime extends to $\epsilon \approx 0.08\%$, where the helium begins to deform plastically. At 0.9 K, plastic flow begins at smaller strains of around 0.02%, and the flow stresses are much smaller. The flow stresses increase with strain ϵ and with strain rate $\dot{\epsilon}$. At 1.2 K, the flow stresses are essentially constant and are much smaller, less than 0.4 kPa at the lowest strain rate $\dot{\epsilon} = 8 \times 10^{-6}$ s^{-1}. Extrapolating to the sample's melting point, 1.55 K, gives flow stresses of less than 100 Pa. This is about 4 orders of magnitude smaller than the yield stress of an extremely ductile metal like indium near its melting point. It is also much smaller than the flow stresses in earlier measurements on hcp ^{4}He at similar temperatures, such as those shown in Figs. 45 and 46 (Sanders *et al.*, 1977; Suzuki, 1977). The differences may be due to the larger strain rates used in those experiments, their crystals' higher pressures (3.2 versus 2.64 MPa), and their complex flow geometries requiring multiple slip systems.

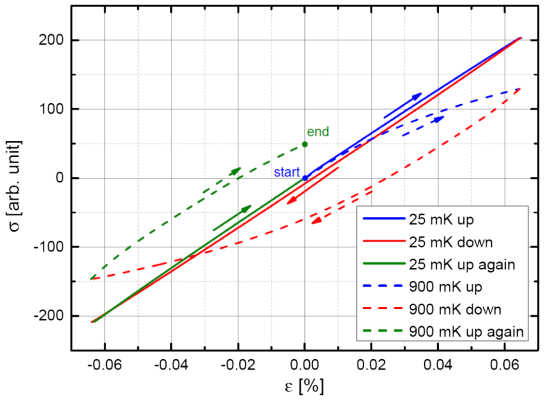

FIG. 47. Stress-strain loops for polycrystalline hcp ^{4}He at 3.4 MPa and temperatures of 25 (solid lines) and 900 mK (dashed lines). The corresponding solid and dashed arrows show the directions of increasing or decreasing strain, starting and ending at zero strain. From Cheng and Beamish, 2018b.

The variation of flow stress with strain rate depends on the creep mechanism but is often described by a power law $\dot{\epsilon} \propto \sigma^n$. Vacancy diffusion gives a creep rate proportional to the pressure gradient and resulting stress $\dot{\epsilon} \propto \sigma$, i.e., $n = 1$, but the creep rates in Fig. 48(d) depend much more strongly on stress, with $n \approx 3.4$, as shown in the inset. Previous measurements gave similar exponents, with n ranging from 3 to 5 in hcp ^{4}He (Tsymbalenko, 1976; Suzuki, 1977), $\sim$3.5 in bcc ^{4}He (Berent and Polturak, 1998), and $\sim$4 in bcc ^{3}He (Sakai, Nishioka, and Suzuki, 1979; Manning, Moelter, and Elbaum, 1986). Exponents between 3 and 4 are characteristic of dislocation mechanisms like Weertman creep (Weertman, 1955; Poirier, 1985), where creep rates are controlled by depinning of dislocations via vacancy diffusion and climb.

B. Low temperature slip and dislocation avalanches

The previously described plasticity involved measurements above about half the samples' melting temperatures. Plastic deformation is quite different at low temperatures where thermally activated processes freeze out. This regime is

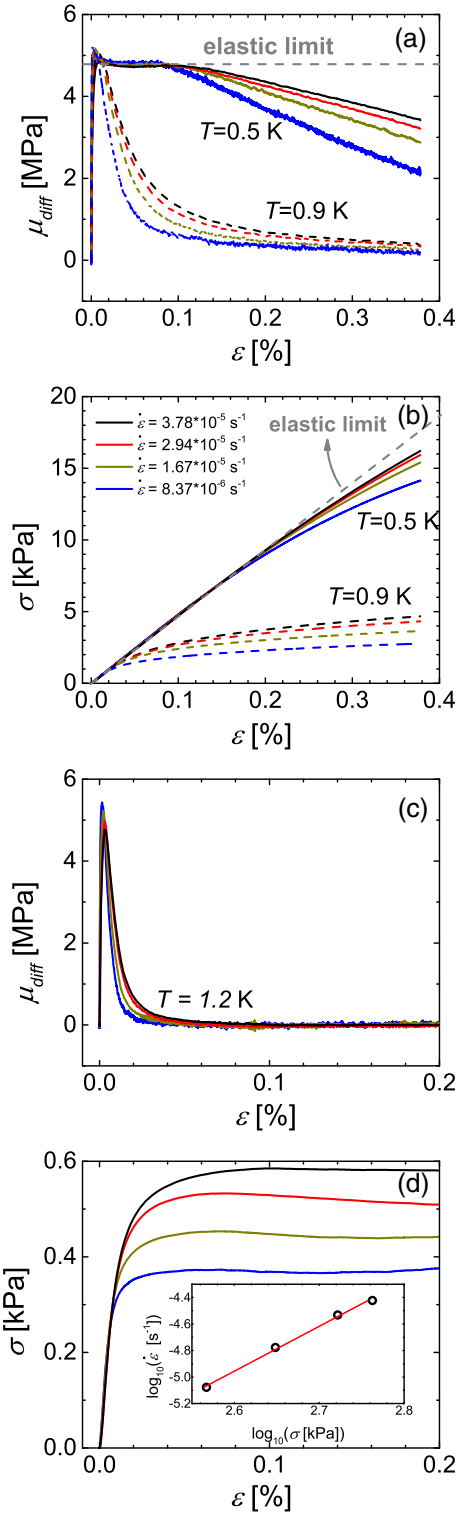

FIG. 48. Plastic creep in a 2.64 MPa hcp ^{4}He sample. (a) Differential shear modulus and (b) corresponding stress measured for different strain rates, at temperatures of 0.5 and 0.9 K. (c), (d) Corresponding data at 1.2 K. The strain rates are given in the inset of (b). In each panel, the lowest (blue) curve corresponds to the lowest strain rate 8.37×10^{-6} s^{-1}, and the higher curves correspond to successively larger strain rates. The inset in (d) shows the relationship between shear stress σ and strain rate $\dot{\epsilon}$. From Cheng and Beamish, 2018b.

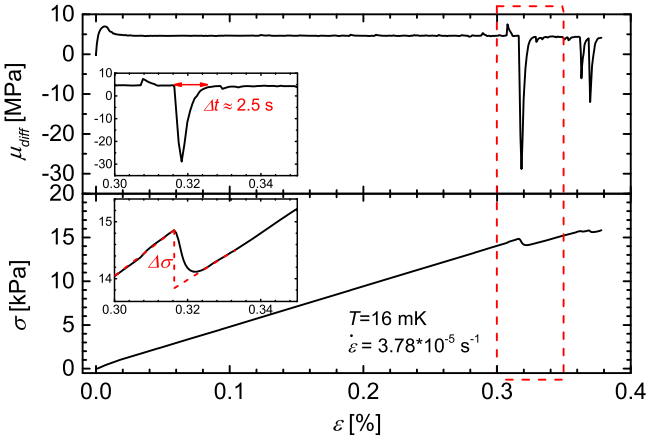

FIG. 49. Differential shear modulus and stress in hcp ^{4}He at 16 mK. Insets: large slip event at $\epsilon = 0.32\%$ on expanded scales.

particularly interesting in a quantum solid like helium where zero point motion dominates, tunneling allows defects like vacancies and impurities to propagate ballistically, and dislocations can move freely. To study nonthermally activated deformation mechanisms, much lower temperatures were required. Although there were a few early experiments below 0.5 K (Levchenko and Mezhov-Deglin, 1982, 1984), their plastic deformation measurements were indirect. Crystals of hcp ^{4}He were grown in a 1 mm diameter capillary and deformed by bending the capillary at temperatures as low as 0.45 K. This reduced the crystals' thermal conductivity, an effect that was attributed to the scattering of thermal phonons from dislocations created during deformation.

The stress-strain measurements of Fig. 48 were extended to temperatures below 400 mK, where thermal creep is negligible. Figure 49 shows $\mu_{\rm diff}$ (upper panel) and σ (lower panel) for the same sample at 16 mK, for a strain rate $\dot{\epsilon} = 3.8 \times 10^{-5}$ s^{-1}. The linear elastic region extended to $\epsilon \approx 0.3\%$, much higher than the 0.08% strain at which plastic deformation began at 0.5 K. At higher strains, plastic deformation involved abrupt stress drops of as much as 5%.

The time over which the stress dropped appeared to be about 2.5 s, but this is essentially the response time of the current amplifier, so faster amplifiers and data acquistion were used to resolve the slip events. A typical strain ramp is shown in Fig. 50(a), with the corresponding stress current i (proportional to $\mu_{\rm diff}$) shown in Fig. 50(b). A typical slip event, which was much faster than the stress drops in Fig. 49, is shown on expanded timescales in Figs. 49(c) and 49(d). The event consisted of a negative current pulse, followed by a 10 kHz oscillation that decayed over about 40 ms. The oscillation was an acoustic resonance (Day and Beamish, 2012) of the solid helium filling the cell, triggered by the sudden stress release in the helium. The actual slip corresponded to the initial negative current, with a duration of about 25 μs.

Similar behavior has been seen in metals, where the slip events were identified as dislocation avalanches that begin when dislocations break away from pinning sites, then move and multiply. A dislocation's motion is driven by the force $b\sigma$

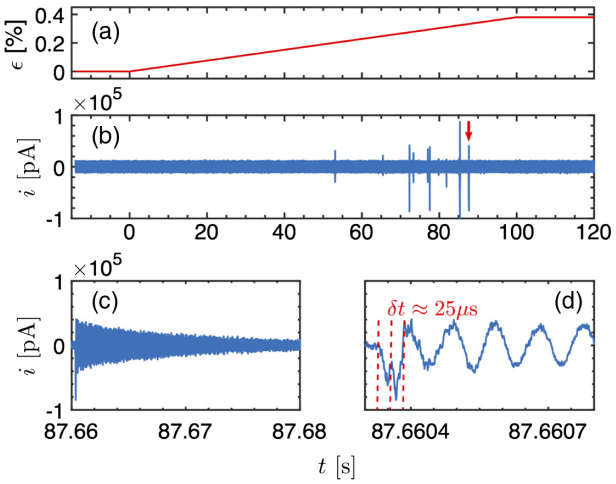

FIG. 50. Dislocation avalanches and acoustic ringing in hcp ^{4}He at 16 mK. (a) Strain. (b) Measured current (proportional to stress). (c) Acoustic ringing over 20 ms following a typical slip event. (d) First 3 ms of the slip event showing the initial negative stress change.

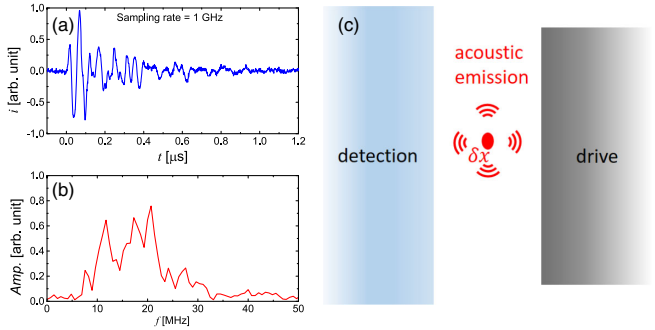

FIG. 51. Acoustic emission from a localized slip event in hcp ^{4}He at 16 mK. (a) Acoustic signal. (b) Frequency spectrum of acoustic signal. (c) Schematic showing the localized event in the gap containing solid helium and the acoustic emission that is detected by the piezoelectric transducer.

proportional to the shear stress and is opposed by the damping force B proportional to its speed. This limits the dislocation's speed to $v_f = b\sigma/B$. In metals, the damping is due to electrons and limits v_f to ∼10 m/s for megapascal applied stresses (Gorman, Wood, and Vreeland, 1969; Schaarwachter and Ebener, 1990). Even at the extremely high strain rates in shock experiments, typical dislocation speeds are much less than the sound speed (Richeton, Weiss, and Louchet, 2005); Lebyodkin *et al.*, 2009; Shashkov, Lebyodkin, and Lebedkina, 2012). In contrast, dislocations in helium move freely at low temperatures since the only damping is due to thermal phonons, with $B \approx 1.5 \times 10^{-8} T^3$ Pa s (Haziot, Fefferman, Beamish, and Balibar, 2013). For a shear stress of 15 kPa, this limits dislocation speeds in ^{4}He to about 30 m/s near the melting temperature ($T_m = 1.55$ K). At 16 mK, however, the phonon damping force is negligible, even for dislocations moving at the speed of sound ($v_t \approx 200$ m/s). Even though solid helium has sound speeds an order of magnitude slower than typical metals, its dislocations can move and avalanches can propagate much faster, at close to the speed of sound.

Dislocation avalanches are usually detected from the sound waves generated by the sudden slip. In the helium deformation experiments, this acoustic emission could be captured with a digital oscilloscope, even for events much faster than that shown in Fig. 50(d). A typical example is shown in Fig. 51(a). The entire event occurs in less than a microsecond and generates a sound pulse with the spectrum shown in Fig. 51(b), centered around 20 MHz. Since elastic deformations (including dislocations) cannot move faster than the speed of sound, the acoustic emission frequencies provide an upper limit on the size of the slip events. This is less than 5 μm for the event in Fig. 51, much smaller than the dimensions of the solid helium sample (which was grown in a 170 μm gap between the transducers). Dislocation avalanches can occur inside the helium, away from the walls. The event in Fig. 49 is much larger, involving at least 5% of the gap area, so it must have a dimension of several millimeters. The size of the slip regions in these low temperature deformation experiments spans many orders of magnitude.

C. Pressure gradients, yield stress, and annealing

In many applications the use of materials is determined by their yield stress σ_c, the threshold at which plastic deformation begins. In solid helium, the yield stress limits the pressure differences that can be maintained within solid helium, for example, during freezing of helium using the blocked capillary method. Although helium's yield stress is small, in some geometries the pressure differences can be large. For example, a pressure difference ΔP between the ends of a cylindrical cell (of length L and radius R) generates a net force $\pi R^2 \Delta P$ on the helium, which must be balanced by the force exerted by the sidewalls $2\pi RL\sigma_w$. If the shear stress at the wall σ_w exceeds the yield stress, the helium deforms plastically and flows, as in the extrusion process used to make wires. The pressure at which this begins $\Delta P_{\max} = 2\sigma_c L/R$ depends on the aspect ratio L/R of the cylinder. For solid helium with a low temperature yield strength $\sigma_c \approx 15$ kPa, a cylinder with an L/R ratio of 250 (e.g., a 3 mm long channel with a diameter of 25 μm, or a 5 cm long capillary with inner diameter 0.4 mm) could sustain pressure differences up to 7.5 MPa (75 bar) before slipping. This is the basis of the standard blocked capillary technique for freezing helium. Note that large pressure differences can occur not just in blocked capillaries but in any cell with a large aspect ratio (Suhel and Beamish, 2011). Examples include long cylinders (Ray and Hallock, 2008), thin disks (Tsymbalenko, 1977; Rittner and Reppy, 2009; Degtyarev *et al.*, 2010), and narrow annular gaps (Rittner and Reppy, 2007).

At high temperatures, or in open cells with $L/R \sim 1$, pressure differences are much smaller but may still be significant. For example, Suhel and Beamish (2011) used rapid thermal quenching to generate pressure gradients in a cylindrical cell with length 30 mm and radius 15 mm ($L/R = 4$). A short current pulse was applied to a heater embedded near one end of a solid ^{4}He sample at 50 mK, partially melting it. The helium refroze and cooled rapidly, reaching temperatures below 400 mK in as little as 20 s. This produced pressure differences as large as 35 kPa between *in situ* gauges at opposite

ends of the cell. This corresponds to $\sigma_c \approx 4.4$ kPa, smaller than the 15 kPa yield stress from Fig. 49, which suggests that some of the initial pressure gradients relaxed at the higher temperatures during the initial thermal quench. Similar pressure differences have been observed in other helium experiments using cells with multiple pressure gauges (Ray and Hallock, 2009; Birchenko *et al.*, 2018).

Annealing at high temperatures can remove some defects and reduce internal stresses in crystals, as shown in the experiments by Suhel and Beamish (2011). For a 3.1 MPa polycrystalline hcp ^{4}He sample (melting temperature of 1.79 K), the initial pressure difference between opposite ends of the cell (≈26 kPa) was stable at temperatures below 400 mK. When the temperature was raised above 500 mK, the pressure difference decreased at a rate that increased with temperature. The data were consistent with a thermally activated annealing process with an activation energy of about 5 K. However, annealing above 500 mK did not completely eliminate pressure differences. When the temperature was held constant at 0.9 K, the pressure difference stabilized at 4.3 kPa after 9 h. This corresponds to a static shear stress of ∼0.5 kPa, similar to the yield stress (∼1 kPa) at which creep begins at 0.9 K in Fig. 48. When the sample was warmed above 0.9 K, the pressure difference decreased further, to less than 1 kPa at 1.5 K. This is consistent with the decrease in yield stress at high temperatures (e.g., to ∼300 Pa at 1.2 K in Fig. 48).

Solid helium can support significant pressure differences, which can be eliminated only by warming the sample close to its melting temperature.

D. Flow in solid helium

1. Vacancy diffusion flow

Vacancies enable dislocations to climb and thus play an important role in plastic deformation by allowing dislocations to move around obstacles or to annihilate. At high temperatures, vacancies can also eliminate stresses via Nabarro-Herring vacancy creep, which transports mass directly, as discussed in Sec. III.A. In contrast to dislocations, which move in response to shear stresses, vacancies diffuse in pressure gradients but do not respond directly to shear deformations. The equilibrium vacancy concentration given by Eq. (2) is proportional to $e^{-[(E_v+Pv_v)/k_BT]}$, so at temperatures high enough to create thermal vacancies a gradient in the pressure P creates a gradient in the vacancy concentration gradient x_v. Vacancies diffusing from low to high pressure regions produce a mass flow that reduces the pressure gradient.

However, the timescale for diffusive processes scales with the square of the sample dimension, so pressure relaxation via vacancy diffusion is extremely slow over large distances. For example, the blocked capillary technique relies on the flow of solid helium being negligible under the pressure gradients along the capillary. An early experiment searching for supersolidity in hcp ^{4}He (Greywall, 1977b) detected no flow and established extremely low limits on pressure-induced flow at temperatures down to 30 mK. Diffusive vacancy flow is much more important in small samples and at high temperatures. For helium confined in the nanoscale pores of Vycor glass, ultrasonic measurements (Beamish *et al.*, 1991) showed that vacancy diffusion relaxed stresses within a pore on microsecond timescales at temperatures above 1 K. When external pressure was applied to a Vycor sample containing solid helium (Day, Herman, and Beamish, 2005), mass flowed macroscopic distances into the pores at high temperatures, but no flow was seen below 500 mK. In a similar experiment in which a pressure difference of about 10 kPa was applied across solid ^{4}He in 3 mm long, 25 μm diameter channels, mass flow through the channels equilibrated the pressures at temperatures near melting (Day and Beamish, 2007a). Below 1 K there was no evidence of flow (Day and Beamish, 2006), which is not surprising, given helium's yield stress and the channels' large aspect ratio ($L/R = 240$).

One experiment involving hcp ^{4}He in a high aspect ratio cell (a disk-shaped chamber of thickness 0.1 mm and radius 8.6 mm) did detect a slow pressure relaxation at temperatures as low as 19 mK (Rittner and Reppy, 2009). The relaxation rate was compatible with a thermal activation process but the activation energy ∼28 mK was extremely small and the flow mechanism was not clear.

The absence of nonactivated flow at low temperatures is consistent with the consensus that there are no zero point vacancies in hcp ^{4}He. However, thermal vacancies cannot simply vanish when a solid is cooled. To disappear, they must diffuse to a vacancy sink, i.e., to a crystal surface or to internal defects like dislocations and grain boundaries. Vacancies in helium might also phase separate into clusters (Boninsegni *et al.*, 2006), in which case they would collapse to create prismatic dislocation loops (Hull and Bacon, 2011). If thermal quenching is fast enough, larger nonequilibrium vacancy concentrations might survive. Unusual features in experiments involving solid helium flow through a nozzle have been interpreted in terms of flow of vacancies at large nonequilibrium concentrations (Benedek *et al.*, 2016).

Since the vacancy flow rate is directly proportional to the pressure gradient, more sensitive measurements can be made by applying pressure differences across shorter channels. Zhuchkov *et al.* (2015) used a capacitative technique in which a pressure difference was generated across 6–8 μm diameter channels through a 10 μm thick polymer membrane ($L/R \sim 3$) embedded in solid ^{4}He. Flow velocities through the channels, determined from the displacement of the membrane, are shown in the upper panel of Fig. 52. At high temperatures they observed thermally activated flow with activation energies between 6.5 and 13.9 K, which is consistent with vacancy activation energies in ^{4}He. Below 500 mK the temperature dependence was much weaker, corresponding to activation energies ∼0.5–0.7 K. They attributed the high temperature flow to thermally activated vacancy diffusion, but the origin of the slow creep at low temperatures was unclear, although it might involve the motion of the dislocation kinks.

Lisunov *et al.* (2015, 2016) made similar measurements on bcc ^{3}He, shown in the lower panels of Fig. 52. Above 200 mK they saw thermally activated flow, with activation energies between 2.3 and 3.1 K. These energies are smaller than for hcp ^{4}He but are similar to vacancy energies in bcc ^{3}He [e.g., 4.25 K at 35 bar (Heald, Baer, and Simmons, 1984)]. However, the flow rate for ^{3}He did not continue to drop below 200 mK, instead approaching a constant value at the lowest temperature

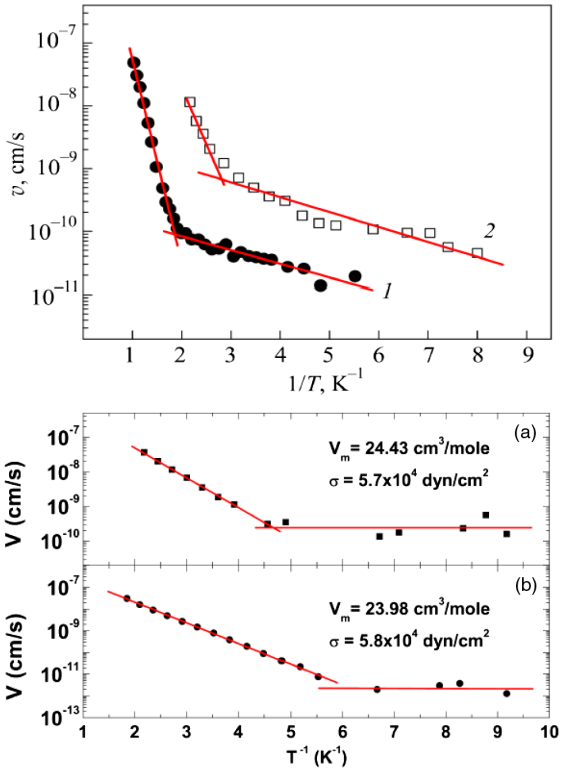

FIG. 52. Flow velocity for solid helium in 6 to 8 μm diameter channels through a membrane. Upper panel: data for two polycrystalline hcp ^{4}He samples (labeled 1 and 2) with molar volume 21.05 cm^3/mol. From Zhuchkov *et al.*, 2015. Lower panel: data for polycrystalline bcc ^{3}He at samples with molar volumes (a) 24.43 and (b) 23.98 cm^3/mol. From Lisunov *et al.*, 2015.

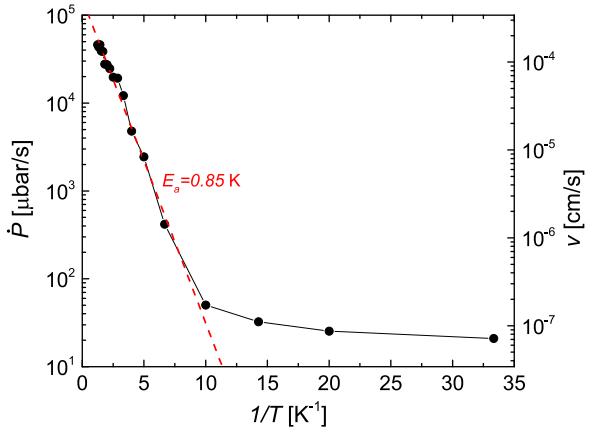

FIG. 53. Flow velocity (right axis) and rate of pressure change (left axis) for polycrystalline bcc ^{3}He in a 3 mm diameter channel, at a pressure of 3.6 MPa. The dashed line corresponds to a thermally activated process with activation energy 0.85 K. From Cheng and Beamish, 2018a.

(100 mK). Lisunov *et al.* suggested that the high temperature flow involved motion of dislocations via the thermally activated creation of kink pairs. The temperature-independent flow below 200 mK indicated a quantum mechanism of mass transport, but the mechanism was unclear.

A recent experiment on bcc ^{3}He confined in a much larger channel (3 mm diameter, with $L/R \approx 6$) gave similar results, which are shown in Fig. 53 (Cheng and Beamish, 2018a). A pressure difference applied between the ends of the channel generated flow that was thermally activated above 100 mK but approached a constant rate at the lowest temperature (30 mK). However, the activation energy was smaller (~0.85 K) and the flow rates were much larger than in the experiments of Lisunov *et al.* (2015, 2016). This suggests that both the thermally activated and the temperature-independent flow shown in Fig. 53 involve dislocations, which would be more mobile in this bulk geometry than in the small channels of Lisunov *et al.*, where they are expected to be pinned at the walls.

2. Low temperature superflow in solid ^{4}He

In addition to the previously described creep and plastic flow, recent experiments showed intriguing low temperature mass flow through cells filled with hcp ^{4}He (Ray and Hallock, 2008; Hallock, 2015, 2019). This flow appeared below 0.6 K, with flow rates that were nearly independent of the pressure difference across the solid and that increased at lower temperatures. These features are not associated with thermally activated flows like those described earlier, but they are typical of superfluids. The low temperature flow was sensitive to ^{3}He impurities, with concentrations x_3 as small as 10^{-6} blocking the flow below 100 mK (Vekhov, Mullin, and Hallock, 2014; Cheng and Beamish, 2016). This suggests that the flow occurs along low-dimensional channels, for example, superflow in a network of one-dimensional dislocations (Vekhov and Hallock, 2012; Shin *et al.*, 2017), a possibility raised by PIMC simulations (Boninsegni *et al.*, 2007) that indicated that some types of dislocations in hcp ^{4}He have superfluid cores. This topic was recently reviewed by Hallock (2019).

VII. OPEN QUESTIONS AND FUTURE DIRECTIONS

The work discussed in this review makes it clear that defects like vacancies, impurities, and dislocations have dramatic but well-understood effects on the mechanical behavior of quantum solids like helium. However, it is important to note that essentially all the experiments upon which this understanding is based involve mobile dislocations, primarily those gliding in the basal plane of hcp ^{4}He. There is no direct experimental evidence of the properties (or even the existence) of other types of dislocations in helium, despite their importance in plastic deformation and flow. This contrasts with the situation in metals and other conventional materials, where TEM and x-ray techniques have been used to directly confirm the properties of different types of dislocations, and to determine their densities and network structures.

Although the high pressures required to grow helium crystals rule out TEM imaging, it is possible that modern synchrotron x-ray sources and techniques could provide microscopic information about the structure of dislocations, stacking faults, and grain boundaries. It might also be possible to take advantage of advances in "matrix isolation" spectroscopy of atoms embedded in solid helium to image or probe

extended defects, in analogy to the impurity decoration techniques that have been used to image vortices in superfluid droplets (Gomez *et al.*, 2014; Gessner and Vilesov, 2019).

In the absence of direct imaging of dislocations, experiments can determine only average properties associated with networks having unknown distributions of orientations and loop lengths. Recent low frequency shear modulus measurements on optically oriented single crystals have provided detailed and consistent information about dislocation networks in hcp ^{4}He. However, there are significant discrepancies with, for example, the dislocation densities and lengths inferred less directly from high frequency ultrasonic measurements.

One possible approach to extract information about specific dislocations would be to probe mechanical properties on a microscopic scale. Given the low dislocation densities ($\Lambda \sim 10^4/\mathrm{cm}^2$) and the loop lengths ($L \sim 100$ μm) inferred from shear modulus measurements in high quality ^{4}He crystals, it seems likely that there are dislocation-free regions with dimensions of tens of micrometers. There have been a few experiments involving solid helium confined on this scale, including flow measurements across an 8 μm gap (Shin *et al.*, 2017) or along 25 μm cylindrical channels (Day and Beamish, 2006), and shear modulus measurements on helium in an 11 μm gap (Aoki *et al.*, 2016). The smallest avalanches detected in hcp ^{4}He polycrystals (Cheng and Beamish, 2018b) at low temperatures were of comparable sizes and may have been initiated at a single dislocation. Submicron cavities have been used to probe superfluid helium (Souris *et al.*, 2017), and it may be possible to apply micromechanical or optomechanical techniques to study solid helium samples small enough to be free of dislocations or other defects. Such measurements could test predictions (Borda, Cai, and Koning, 2014) of the ultimate shear strength of perfect helium crystals or allow dislocations to be introduced into perfect crystals to test dislocation models of superflow.

Numerical simulations have provided a great deal of information about dislocations and their networks in conventional solids. In quantum solids, PIMC simulations have made remarkable advances, but they are still limited to relatively small numbers of atoms and thus cannot provide the same level of detailed information about extended defects and dislocation networks in helium crystals.

Neither PIMC simulations nor experiments provide evidence for the existence of equilibrium zero point vacancies in solid helium, but they may exist in regions of large elastic strain (Pollet *et al.*, 2008). It is also possible that nonequilibrium vacancies could be introduced into solid helium by rapid deformation or flow (Benedek *et al.*, 2016). Rapid thermal quenching could also produce a finite concentration of vacancies at low temperatures, given the large equilibrium vacancy concentration (∼0.3%) near melting. Since these vacancies can disappear only by migrating to a surface or a defect like an edge dislocation or by phase separating, a finite concentration might survive rapid cooling to low temperatures, particularly in ^{3}He, where they are expected to be less mobile than in ^{4}He.

One of the most intriguing phenomena in solid ^{4}He is the low temperature flow that appears around 0.6 K in low pressure crystals (Hallock, 2019). The flow increases upon cooling but is blocked at around 100 mK by small concentrations of ^{3}He impurities. It has characteristics of superflow but the nature and the location of the flow channels are not yet certain (Cheng and Beamish, 2016). However, recent experiments with partially blocked channels do not appear to be consistent with flow in 2D films (Rubanskyi and Hallock, 2019; Shin and Chan, 2019). One-dimensional flow along superfluid dislocation cores, as predicted in PIMC simulations, is an exciting possibility but experiments have not yet provided a "smoking gun" to confirm this scenario. This is largely because there is no direct experimental evidence for the types of dislocations that are predicted to have superfluid cores (screw dislocations aligned along the hcp c axis; edge dislocations lying in the basal plane and Burgers vectors along the hcp c axis). The superfluidity predicted for these dislocations appears to be due to the fact that they do not disassociate into partials and thus have large strains near their cores. This also results in large Peierls barriers, which immobilizes them. The mobile dislocations that can be detected in elastic measurements (edge or screw dislocations gliding in the basal plane) have essentially the opposite properties. They dissociate into widely separated partials with small strains and have no measurable Peierls barrier to their motion.

A number of experiments have recently been proposed to more clearly distinguish the flow or superclimb associated with superfluid dislocations from other possible deformation or flow mechanisms (Kuklov, 2019). However, clear confirmation of superfluid dislocations would require oriented single crystals that can be compressed or sheared in specific crystallographic directions. Although challenging, this could be done by using the optical orientation and crystal growth techniques that were used so successfully in the low frequency shear modulus experiments to provide detailed information on the properties of mobile basal dislocations in ^{4}He. Measurements with optically oriented single crystals would have similar advantages for many other measurements, including plastic deformation experiments.

The recent plastic deformation experiments by Cheng and Beamish (2018b) showed that at temperatures below 0.4 K large-scale deformation in hcp ^{4}He occurs via dislocation avalanches. The avalanches had a wide range of sizes and their accompanying acoustic emission provides opportunities to study the scaling laws that have been observed in conventional solids, but in nonthermal and quantum regimes. Similar experiments on bcc crystals, with their differing dislocation structures, multiple slip systems, and expected Peierls barriers, would be valuable. Although elastic measurements on bcc ^{4}He and ^{3}He have shown some signatures of mobile dislocations, there is presently much less information about their properties than for the hcp phases of helium.

Vacancies appear to play a more important role in the bcc phase of ^{4}He, where plastic deformation occurs smoothly (Ahlstrom *et al.*, 2014) and does not seem to involve the creation of dislocations (Sanders *et al.*, 1977). To better understand the role of vacancies and dislocations in the deformation of bcc helium, measurements should be made over a wide range, extending to low temperatures where vacancies freeze out. This is not possible in ^{4}He since the bcc

phase does not exist below 1.5 K, but it can be done in the bcc phase of ^{3}He, which is even more quantum mechanical than the more thoroughly studied hcp ^{4}He.

Solid ^{3}He also provides a unique opportunity to study the effects of spin on dislocation motion. Low frequency shear modulus measurements on hcp ^{3}He (Cheng and Beamish, 2017) were interpreted in terms of a new "spin friction" mechanism of dislocation damping, an addition to the known phonon and electron damping mechanisms in other materials. Measurements at lower temperatures, particularly in the spin-ordered magnetic phases below 1 mK, would confirm this and might provide insight into dislocation motion in conventional magnetic solids.

ACKNOWLEDGMENTS

We want to express our appreciation to our students, postdoctoral fellows, and collaborators on the work described in this review, and to Pawel Pieranski for providing Fig. 36. We also want to thank our colleagues in the field of helium solids, who have generously shared their expertise and ideas over many years. This work was supported by grants from the Natural Sciences and Engineering Council of Canada (NSERC), the University of Alberta, and the ERC (AdG 247258-SUPERSOLID).

REFERENCES

Abel, W. R., A. C. Anderson, and J. C. Wheatley, 1961, "Propagation of Sound in ^{3}He," Phys. Rev. Lett. **7**, 299.

Adams, E. D., Y. H. Tang, K. Uhlig, and G. E. Haas, 1987, "Thermodynamics of freezing and melting of ^{4}He in Vycor," J. Low Temp. Phys. **66**, 85–98.

Adams, E. Dwight, 2004, "Solid helium-3," J. Low Temp. Phys. **135**, 695–721.

Adams, M. A., J. Mayers, O. Kirichek, and R. B. E. Down, 2007, "Measurement of the Kinetic Energy and Lattice Constant in hcp Solid Helium at Temperatures 0.07–0.4 K," Phys. Rev. Lett. **98**, 085301.

Ahlstrom, S. L., *et al.*, 2014, "Plastic properties of solid ^{4}He probed by a moving wire: Viscoelastic and stochastic behavior under high stress," J. Low Temp. Phys. **175**, 147–153.

Alers, G. A., and J. E. Zimmerman, 1965, "Dislocation mobility in fcc metals below 1 K," Phys. Rev. **139**, A414.

Allen, Alastair Robert, M. G. Richards, and J. Schratter, 1982, "Anomalous temperature dependence of D and T_2 for dilute solutions of ^{3}He in solid ^{4}He," J. Low Temp. Phys. **47**, 289–320.

Alles, H., V. Tsepelin, A. Babkin, R. Jochemsen, A. Ya. Parshin, and I. Todoschenko, 2001, "Observations on faceting of ^{3}He crystals at T = 0.55 mK," J. Low Temp. Phys. **124**, 189–196.

Amidon, William H., and Kenneth A. Farley, 2010, "Mass spectrometric ^{3}He measurement in ^{4}He-rich phases: Techniques and limitations for cosmogenic ^{3}He dating of zircon, apatite, and titanite," Geochem. Geophys. Geosyst. **11**.

Andreev, A. F., 1982, "Quantum crystals," Prog. Low Temp. Phys. **8**, 67–131.

Andreev, A. F., K. Keshishev, L. Mezhov-Deglin, and A. Shal'nikov, 1969, "Attempt at observing vacancions in ^{4}He crystals," Zh. Eksp. Teor. Fiz. Pis'ma Red. **9**, 507–510 [JETP Lett. **9**, 306–309 (1969)].

Andreev, A. F., and I. M. Lifshits, 1969, "Quantum theory of defects in crystals," Zh. Eksp. Teor. Fiz. **56**, 2057–2068 [Sov. Phys. JETP **29**, 1107–1113 (1969)].

Andreev, Aleksandr F., 1976, "Diffusion in quantum crystals," Sov. Phys. Usp. **19**, 137.

Andreeva, O. A., K. O. Keshishev, and S. Yu. Osip'yan, 1989, "Anisotropy of growth coefficient and surface hardness of the ^{4}He crystals," JETP Lett. **49**, 759–762.

Andreeva, O. A, and K. O Keshishev, 1991, "Solid-superfluid ^{4}He interface," Phys. Scr. **T39**, 352.

Andronikashivili, E. L., 1946, "A direct observation of two kinds of motion in helium II," Zh. Eksp. Teor. Fiz. **16**, 780.

Aoki, Yuki, Izumi Iwasa, Takeru Miura, Akira Yamaguchi, and Yuichi Okuda, 2016, "Shear modulus of solid helium-4 confined in a 10 μm gap," Physica (Amsterdam) **482B**, 19–23.

Arms, D. A., R. S. Shah, and R. O. Simmons, 2003, "X-ray Debye-Waller factor measurements of solid ^{3}He and ^{4}He," Phys. Rev. B **67**, 094303.

Babkin, A. V., H. Alles, Pertti J. Hakonen, A. Ya. Parshin, J. P. Ruutu, and J. P. Saramaki, 1995, "Observation of a New Surface State on ^{4}He Crystal Interfaces," Phys. Rev. Lett. **75**, 3324.

Balibar, S., and B. Castaing, 1985, "Helium: Solid-liquid interfaces," Surf. Sci. Rep. **5**, 87–143.

Balibar, S., B. Castaing, and C. Laroche, 1980, "Nucleation and orientation of ^{4}He crystals," J. Phys. (Paris), Lett. **41**, 283–285.

Balibar, S., D. O. Edwards, and C. Laroche, 1979, "Surface tension of solid ^{4}He," Phys. Rev. Lett. **42**, 782.

Balibar, S., T. Mizusaki, and Y. Sasaki, 2000, "Comments on heterogeneous nucleation in helium," J. Low Temp. Phys. **120**, 293–314.

Balibar, S., and P. Nozières, 1994, "Helium crystals as a probe in materials science," Solid State Commun. **92**, 19–29.

Balibar, Sébastien, Harry Alles, and Alexander Ya. Parshin, 2005, "The surface of helium crystals," Rev. Mod. Phys. **77**, 317–370.

Balibar, Sébastien, John Beamish, Andrew Fefferman, Ariel Haziot, and Xavier Royas, 2016, "Dislocations in a quantum crystal: Solid helium: A model and an exception," C.R. Phys. **17**, 264–275.

Bauer, Charles L., and Robert B. Gordon, 1962, "Mechanism for dislocation pinning in the alkali halides," J. Appl. Phys. **33**, 672–682.

Beamish, J. R., 2001, "Elastic properties of solid inert gases," in *Handbook of Elastic Properties of Solids, Liquids, and Gases*, Vol. 2, edited by M. Levy, H. Bass, and R. Stern (Academic Press, New York), p. 77.

Beamish, J. R., 2019, "Plastic deformation and creep in solid helium," J. Low Temp. Phys. **197**, 187–207.

Beamish, J. R., A. D. Fefferman, A. Haziot, X. Rojas, and S. Balibar, 2012, "Elastic effects in torsional oscillators containing solid helium," Phys. Rev. B **85**, 180501.

Beamish, J. R., and J. P. Franck, 1982, "Sound propagation at frequencies from 3 to 21 MHz in hcp and bcc ^{3}He and its interaction with dislocations," Phys. Rev. B **26**, 6104.

Beamish, J. R., and J. P. Franck, 1983, "Pinning of dislocations in hcp and bcc ^{3}He by stress waves and by ^{4}He impurities," Phys. Rev. B **28**, 1419.

Beamish, J. R., A. Hikata, L. Tell, and C. Elbaum, 1983, "Solidification and Superfluidity of ^{4}He in Porous Vycor Glass," Phys. Rev. Lett. **50**, 425.

Beamish, J. R., N. Mulders, A. Hikata, and C. Elbaum, 1991, "Vacancy diffusion and stress relaxation in ^{4}He freezing in porous Vycor," Phys. Rev. B **44**, 9314.

Benedek, Giorgio, Anton Kalinin, Pablo Nieto, and J. Peter Toennies, 2016, "Vacancy-induced flow of solid helium," Phys. Rev. B **93**, 104505.

Bennemann, Karl Heinz, and John Boyd Ketterson, 1976, *Physics of Liquid and Solid Helium: Part I*, Interscience Monographs and Texts in Physics and Astronomy Vol. 25 (Wiley, New York).

Berberich, P., P. Leiderer, and S. Hunklinger, 1976, "Investigation of the lifetime of longitudinal phonons at GHz frequencies in liquid and solid ^{4}He," J. Low Temp. Phys. **22**, 61–84.

Berent, Inon, and Emil Polturak, 1998, "Critical Behavior of the Shear Resistance of Solid ^{4}He near a Structural Phase Transition," Phys. Rev. Lett. **81**, 846.

Bernier, M. E., and J. H. Hetherington, 1989, "Vacancies in solid ^{3}He," Phys. Rev. B **39**, 11285.

Bernu, B., and D. M. Ceperley, 2005, "Path integral calculations of exchange in solid ^{4}He," J. Phys. Chem. Solids **66**, 1462–1466.

Birchenko, A. P., N. P. Mikhin, E. Ya. Rudavskii, S. N. Smirnov, and Ya. Yu. Fysun, 2018, "Pressure relaxation and diffusion of vacancies in rapidly grown helium crystals," Low Temp. Phys. **44**, 304–316.

Blackburn, E., J. M. Goodkind, S. K. Sinha, J. Hudis, C. Broholm, J. van Duijn, C. D. Frost, O. Kirichek, and R. B. E. Down, 2007, "Absence of a low-temperature anomaly in the Debye-Waller factor of solid ^{4}He down to 140 mK," Phys. Rev. B **76**, 024523.

Bodensohn, Joachim, Klaus Nicolai, and Paul Leiderer, 1986, "The growth of atomically rough ^{4}He crystals," Z. Phys. B **64**, 55–64.

Bonfait, G., H. Godfrin, and B. Castaing, 1989, "Solid ^{4}He: Search for superfluidity," J. Phys. (Paris) **50**, 1997–2002.

Boninsegni, M., A. B. Kuklov, L. Pollet, N. V. Prokofev, B. V. Svistunov, and M. Troyer, 2007, "Luttinger Liquid in the Core of a Screw Dislocation in Helium-4," Phys. Rev. Lett. **99**, 035301.

Boninsegni, Massimo, A. B. Kuklov, Lode Pollet, N. V. Prokofev, B. V. Svistunov, and Matthias Troyer, 2006, "Fate of Vacancy-Induced Supersolidity in ^{4}He," Phys. Rev. Lett. **97**, 080401.

Boninsegni, Massimo, Nikolay Prokofev, and Boris Svistunov, 2006, "Worm Algorithm for Continuous-Space Path Integral Monte Carlo Simulations," Phys. Rev. Lett. **96**, 070601.

Borda, Edgar Josué Landinez, Wei Cai, and Maurice de Koning, 2014, "Ideal Shear Strength of a Quantum Crystal," Phys. Rev. Lett. **112**, 155303.

Borda, Edgar Josué Landinez, Wei Cai, and Maurice de Koning, 2016, "Dislocation Structure and Mobility in hcp ^{4}He," Phys. Rev. Lett. **117**, 045301.

Bukhari, Syed, Md Islam, Ariel Haziot, and John Beamish, 2014, "Shear piezoelectric coefficients of PZT, $LiNbO_3$ and PMN-PT at cryogenic temperatures," J. Phys. Conf. Ser. **568**, 032004.

Burns, C. A., N. Mulders, L. Lurio, M. H. W. Chan, A. Said, C. N. Kodituwakku, and P. M. Platzman, 2008, "X-ray studies of low-temperature solid ^{4}He," Phys. Rev. B **78**, 224305.

Burns, Clement A., and John M. Goodkind, 1994, "Vacancies in solid ^{4}He: Conflicting experimental evidence," J. Low Temp. Phys. **95**, 695–714.

Cai, Wei, and William D. Nix, 2016, *Imperfections in crystalline solids* (Cambridge University Press, Cambridge, England).

Cazorla, C., Y. Lutsyshyn, and J. Boronat, 2012, "Elastic constants of solid ^{4}He under pressure: Diffusion Monte Carlo study," Phys. Rev. B **85**, 024101.

Ceperley, D. M., and G. Jacucci, 1987, "Calculation of Exchange Frequencies in bcc ^{3}He with the Path-Integral Monte Carlo Method," Phys. Rev. Lett. **58**, 1648.

Ceperley, David M., 1995, "Path integrals in the theory of condensed helium," Rev. Mod. Phys. **67**, 279.

Ceperley, David M., and E. L. Pollock, 1986, "Path-Integral Computation of the Low-Temperature Properties of Liquid ^{4}He," Phys. Rev. Lett. **56**, 351.

Cheng, Zhi Gang, and John Beamish, 2016, "Compression-Driven Mass Flow in Bulk Solid ^{4}He," Phys. Rev. Lett. **117**, 025301.

Cheng, Zhi Gang, and John Beamish, 2017, "Defect motion in a quantum solid with spin: hcp ^{3}He," Phys. Rev. B **95**, 180103.

Cheng, Zhi Gang, and John Beamish, 2018a, "Mass Flow through Solid ^{3}He in the bcc Phase," Phys. Rev. Lett. **121**, 225304.

Cheng, Zhi Gang, and John Beamish, 2018b, "Plastic Deformation in a Quantum Solid: Dislocation Avalanches and Creep in Helium," Phys. Rev. Lett. **121**, 055301.

Cheng, Zhi Gang, Fabien Souris, and John Beamish, 2016, "Shear modulus and dislocations in bcc solid ^{3}He," J. Low Temp. Phys. **183**, 99–105.

Chester, G. V., 1970, "Speculations on Bose-Einstein condensation and quantum crystals," Phys. Rev. A **2**, 256.

Choi, Jaewon, Jaeho Shin, and Eunseong Kim, 2015, "Frequency-dependent study of solid ^{4}He contained in a rigid double-torus torsional oscillator," Phys. Rev. B **92**, 144505.

Clark, Bryan K., and David M. Ceperley, 2008, "Path integral calculations of vacancies in solid helium," Comput. Phys. Commun. **179**, 82–88.

Corboz, P., L. Pollet, N. V. Prokofev, and M. Troyer, 2008, "Binding of a ^{3}He Impurity to a Screw Dislocation in Solid ^{4}He," Phys. Rev. Lett. **101**, 155302.

Crepeau, Richard Hanes, O. Heybey, D. M. Lee, and Stanley A Strauss, 1971, "Sound propagation in hcp solid helium crystals of known orientation," Phys. Rev. A **3**, 1162.

Dash, J. G., and J. S. Wettlaufer, 2005, "Classical Rotational Inertia of Solid ^{4}He," Phys. Rev. Lett. **94**, 235301.

Day, James, and John Beamish, 2006, "Pressure-Driven Flow of Solid Helium," Phys. Rev. Lett. **96**, 105304.

Day, James, and John Beamish, 2007a, "Flow of solid ^{4}He near melting," J. Low Temp. Phys. **148**, 683–687.

Day, James, and John Beamish, 2007b, "Low-temperature shear modulus changes in solid ^{4}He and connection to supersolidity," Nature (London) **450**, 853.

Day, James, and John Beamish, 2012, "Acoustic resonances and nonlinearity in solid ^{4}He," J. Low Temp. Phys. **166**, 33–48.

Day, James, Tobias Herman, and John Beamish, 2005, "Freezing and Pressure-Driven Flow of Solid Helium in Vycor," Phys. Rev. Lett. **95**, 035301.

Day, James, Oleksandr Syshchenko, and John Beamish, 2009, "Intrinsic and dislocation-induced elastic behavior of solid helium," Phys. Rev. B **79**, 214524.

Day, James, Oleksandr Syshchenko, and John Beamish, 2010, "Nonlinear Elastic Response in Solid Helium: Critical Velocity or Strain?," Phys. Rev. Lett. **104**, 075302.

Degtyarev, I. A., A. A. Lisunov, V. A. Maidanov, V. Yu. Rubanskiy, S. P. Rubets, E. Ya. Rudavskii, A. S. Rybalko, and V. A. Tikhii, 2010, "Formation of a disordered (glassy) phase in deformed solid ^{4}He in the region of supersolid state," J. Exp. Theor. Phys. **111**, 619–626.

Dobbs, E. R., 2000, *Helium Three* (Oxford University Press, New York).

Eckert, J., W. Thomlinson, and G. Shirane, 1977, "Lattice dynamics of fcc helium at high pressure," Phys. Rev. B **16**, 1057.

Eckert, J., W. Thomlinson, and G. Shirane, 1978, "Lattice dynamics of hcp ^{4}He at high pressure," Phys. Rev. B **18**, 3074–3081.

Eckstein, Y., J. Landau, S. G. Lipson, and Z. Olami, 1980, "Role of Substrate Symmetry in Nucleating Solid Helium," Phys. Rev. Lett. **45**, 1805–1808.

Edwards, D. O., and S. Balibar, 1989, "Calculation of the phase diagram of ^{3}He-^{4}He solid and liquid mixtures," Phys. Rev. B **39**, 4083–4097.

Edwards, D. O., A. S. McWilliams, and J. G. Daunt, 1962, "Phase Separation in Solid ^{3}He-^{4}He Mixtures, as Shown by Specific Heat Measurements," Phys. Rev. Lett. **9**, 195.

Edwards, D. O., S. Mukherjee, and M. S. Pettersen, 1990, "Quantum Kinks and the Growth Resistance of Atomically Rough ^{4}He Crystals," Phys. Rev. Lett. **64**, 902.

Edwards, D. O, M. S. Pettersen, and H. Baddar, 1991, "The inertia of the ^{4}He crystal surface and the calculation of the phonon transmission," in *Excitations in Two-Dimensional and Three-Dimensional Quantum Fluids*, edited by A. F. G. Wyatt and H. J. Lauter (Springer, New York), pp. 361–374.

Fartash, Arjang, and John M. Goodkind, 1986, "Acoustic Properties of Solid ^{3}He at Low Temperatures," Phys. Rev. Lett. **56**, 1389.

Fefferman, A. D., Fabien Souris, Ariel Haziot, J. R. Beamish, and Sebastien Balibar, 2014, "Dislocation networks in ^{4}He crystals," Phys. Rev. B **89**, 014105.

Fraass, B. A., P. R. Granfors, and R. O. Simmons, 1989, "X-ray measurements of thermal vacancies in hcp ^{4}He," Phys. Rev. B **39**, 124.

Franck, J. P., 1980, "Calorimetric study of the transition between the close-packed phases of ^{4}He from the triple point to 3.9 kbar," Phys. Rev. B **22**, 4315.

Franck, J. P., K. E. Kornelsen, and J. R. Manuel, 1983, "Wetting of fcc ^{4}He Grain Boundaries by Fluid ^{4}He," Phys. Rev. Lett. **50**, 1463.

Franck, J. P., and R. Wanner, 1970, "Elastic Constants of hcp ^{4}He," Phys. Rev. Lett. **25**, 345.

Friedel, J., 1964, *Dislocations* (Pergamon Press, New York).

Gallet, F., P. E. Wolf, and S. Balibar, 1984, "Liquid-Solid ^{4}He Interfacial Tension: Temperature Variation near the Superfluid Transition," Phys. Rev. Lett. **52**, 2253.

Gardner, W. R., J. K. Hoffer, and N. E. Phillips, 1973, "Thermodynamic properties of ^{4}He. the hcp phase at low densities," Phys. Rev. A **7**, 1029.

Gessner, Oliver, and Andrey F. Vilesov, 2019, "Imaging quantum vortices in superfluid helium droplets," Annu. Rev. Phys. Chem. **70**, 173–198.

Glyde, H. R., 1976, in *Rare Gas Solids*, Vol. 7, edited by M. L. Klein and J. A. Venables (Academic Press, New York).

Gomez, Luis F., *et al.*, 2014, "Shapes and vorticities of superfluid helium nanodroplets," Science **345**, 906–909.

Gorman, J. A., D. S. Wood, and T. Vreeland, Jr., 1969, "Mobility of dislocations in aluminum," J. Appl. Phys. **40**, 833–841.

Granato, A. V., and Kurt Lücke, 1981, "Temperature dependence of amplitude-dependent dislocation damping," J. Appl. Phys. **52**, 7136–7142.

Granato, A. V., and Kurt Lücke, 1956, "Theory of mechanical damping due to dislocations," J. Appl. Phys. **27**, 583–593.

Granfors, P. R., B. A. Fraass, and R. O. Simmons, 1987, "Direct measurements of thermal vacancies in bcc ^{4}He," J. Low Temp. Phys. **67**, 353–375.

Greywall, D. S., 1975, "Elastic constants and Debye temperature of bcc ^{3}He," Phys. Rev. B **11**, 1070.

Greywall, D. S., 1976, "Elastic constants of bcc ^{4}He," Phys. Rev. B **13**, 1056.

Greywall, D. S., 1977a, "Elastic constants of hcp ^{4}He," Phys. Rev. B **16**, 5127.

Greywall, D. S., 1977b, "Search for superfluidity in solid ^{4}He," Phys. Rev. B **16**, 1291.

Greywall, D. S., 1977c, "Specific heat of bcc ^{3}He," Phys. Rev. B **15**, 2604.

Greywall, Dennis Stanley, 1971, "Sound propagation in x-ray-oriented single crystals of hcp helium-4 and bcc helium-3," Phys. Rev. A **3**, 2106.

Grigorev, V. N., 1997, "Diffusion in solid helium (a review)," Low Temp. Phys. **23**, 3–14.

Grilly, E. R., 1971, "Pressure-volume-temperature relations in liquid and solid ^{3}He," J. Low Temp. Phys. **4**, 615–635.

Grilly, E. R., 1973, "Pressure-volume-temperature relations in liquid and solid ^{4}He," J. Low Temp. Phys. **11**, 33–52.

Grilly, E. R., and R. L. Mills, 1962, "PVT relations in ^{4}He near the melting curve and the λ-line," Ann. Phys. (N.Y.) **18**, 250–263.

Guyer, R. A., R. C. Richardson, and L. I. Zane, 1971, "Excitations in quantum crystals (a survey of NMR experiments in solid helium)," Rev. Mod. Phys. **43**, 532.

Hallock, R. B., 2015, "Solid ^{4}He: Progress, status, and outlook for mass flux measurements," J. Low Temp. Phys. **180**, 6–19.

Hallock, R. B., 2019, "Mass flux experiments in solid ^{4}He: Some history, recent work and the current status," J. Low Temp. Phys. **197**, 167–186.

Haziot, Ariel, Andrew D. Fefferman, John R. Beamish, and Sébastien Balibar, 2013, "Dislocation densities and lengths in solid ^{4}He from elasticity measurements," Phys. Rev. B **87**, 060509.

Haziot, Ariel, Andrew D. Fefferman, Fabien Souris, John R. Beamish, Humphrey J. Maris, and Sébastien Balibar, 2013, "Critical dislocation speed in helium-4 crystals," Phys. Rev. B **88**, 014106.

Haziot, Ariel, Xavier Rojas, Andrew D. Fefferman, John R. Beamish, and Sébastien Balibar, 2013a, "Giant Plasticity of a Quantum Crystal," Phys. Rev. Lett. **110**, 035301.

Haziot, Ariel, Xavier Rojas, Andrew D. Fefferman, John R. Beamish, and Sébastien Balibar, 2013b, "Haziot *et al.* Reply:," Phys. Rev. Lett. **111**, 119602.

Heald, S. M., D. R. Baer, and R. O. Simmons, 1983, "X-ray diffraction study of thermal vacancies in solid helium-3," Solid State Commun. **47**, 807–810.

Heald, S. M., D. R. Baer, and R. O. Simmons, 1984, "Thermal vacancies in solid ^{3}He," Phys. Rev. B **30**, 2531.

Hendry, P. C., and Peter V. E. McClintock, 1987, "Continuous flow apparatus for preparing isotopically pure ^{4}He," Cryogenics **27**, 131–138.

Heybey, O. W., and D. M. Lee, 1967, "Optical Birefringence and Crystal Growth of Hexagonal-Close-Packed ^{4}He from Superfluid Helium," Phys. Rev. Lett. **19**, 106.

Hirth, J. P., and J. Lothe, 1982, *Theory of Dislocations*, 2nd ed. (Wiley, New York).

Hoffer, J. K., W. R. Gardner, C. G. Waterfield, and N. E. Phillips, 1976, "Thermodynamic properties of ^{4}He. II. The bcc phase and the *P-T* and *V-T* phase diagrams below 2 K," J. Low Temp. Phys. **23**, 63–102.

Hull, Derek, and David J. Bacon, 2011, *Introduction to Dislocations* (Elsevier, New York).

Islam, Md Shahidul, and John Beamish, 2019, "Shear piezoelectric and dielectric properties of $LiNbO_3$, PMN-PT and PZT-5A at low temperatures," J. Low Temp. Phys. **194**, 285–301.

Iwasa, I., 2013, "Dislocation-pinning mechanism for the hysteresis of torsional-oscillator experiments on solid helium," J. Low Temp. Phys. **171**, 287–294.

Iwasa, Izumi, 2002, "Dislocation image on x-ray topographs within kinematical theory," Phys. Rev. B **66**, 144111.

Iwasa, Izumi, Keisuke Araki, and Hideji Suzuki, 1979, "Temperature and frequency dependence of the sound velocity in hcp ^{4}He crystals," J. Phys. Soc. Jpn. **46**, 1119–1126.

Iwasa, Izumi, and Harry Kojima, 2017, "Nonlinear ultrasound propagation in solid ^{4}He compared with shear modulus experiments," J. Low Temp. Phys. **187**, 459–467.

Iwasa, Izumi, and Hideji Suzuki, 1980, "Sound velocity and attenuation in hcp ^{4}He crystals containing ^{3}He impurities," J. Phys. Soc. Jpn. **49**, 1722–1730.

Iwasa, Izumi, and Hideji Suzuki, 1982, "Temperature dependence of the sound velocity in bcc ^{3}He crystals," J. Phys. Soc. Jpn. **51**, 2116–2122.

Iwasa, Izumi, Hideji Suzuki, Tetsuo Nakajima, Shigeo Suzuki, Masami Ando, Ichiro Yonenaga, Masahiro Takebe, and Koji Sumino, 1987, "Observation of lattice defects in solid helium by SR X-ray topography," J. Phys. Soc. Jpn. **56**, 4225–4228.

Iwasa, Izumi, Hideji Suzuki, Takayoshi Suzuki, Tetsuo Nakajima, Ichiro Yonenaga, Haruhiko Suzuki, Hirokazu Koizumi, Yuji Nishio, and Joji Ota, 1995, "Subboundaries in hcp ^{4}He crystals studied by SR X-ray topography," J. Low Temp. Phys. **100**, 147–165.

Kamimura, Y., K. Edagawa, and S. Takeuchi, 2013, "Experimental evaluation of the Peierls stresses in a variety of crystals and their relation to the crystal structure," Acta Mater. **61**, 294–309.

Kang, Evan S. H., Duk Y. Kim, Hyoung Chan Kim, and Eunseong Kim, 2013, "Stress-and temperature-dependent hysteresis of the shear modulus of solid helium," Phys. Rev. B **87**, 094512.

Kang, Evan S. H., Hongkee Yoon, and Eunseong Kim, 2015, "Modified Granato-Lucke theory with pinning length distribution in solid ^{4}He," J. Phys. Soc. Jpn. **84**, 034602.

Keesom, W. H., and K. W. Taconis, 1938, "On the structure of solid helium," Physica (Amsterdam) **5**, 161–169.

Keesom, W. H, 1942, "Helium," Commun. Kamerlingh Onnes Lab. Univ. Leiden **184b**, 180.

Keller, William E., 1969, *Helium-3 and Helium-4* (Plenum, New York).

Keshishev, K. O., A. Ya. Parshin, and A. V. Babkin, 1981, "Crystallization waves in ^{4}He," Sov. Phys. JETP **53**, 362–369.

Keshishev, K. O., A. Ya. Parshin, and A. V. Babkin, 1979, "Experimental detection of crystallization waves in ^{4}He," JETP Lett. **30**, 56–59.

Keshishev, Konstantin, and Olga Andreeva, 1991, "Anisotropy of surface stiffness, growth kinetics and roughening transition in ^{4}He," in *Excitations in Two-Dimensional and Three-Dimensional Quantum Fluids*, edited by A. F. G. Wyatt and H. J. Lauter, NATO ASI, Ser. B, Vol. 257 (Plenum Press, New York), pp. 387–395.

Keyse, R. J., and J. A. Venables, 1985, "Stacking fault energy and crystal stability of solid krypton and xenon," J. Phys. C **18**, 4435.

Kim, D. Y., Hyoungsoon Choi, W. Choi, S. Kwon, Eunseong Kim, and H. C. Kim, 2011, "Unaffected nonclassical response of solid ^{4}He under elastic modulus variation," Phys. Rev. B **83**, 052503.

Kim, Duk Y., and Moses H. W. Chan, 2012, "Absence of Supersolidity in Solid Helium in Porous Vycor Glass," Phys. Rev. Lett. **109**, 155301.

Kim, Eunseong, and M. H. W. Chan, 2004a, "Probable observation of a supersolid helium phase," Nature (London) **427**, 225.

Kim, Eunseong, and Moses H. W. Chan, 2004b, "Observation of superflow in solid helium," Science **305**, 1941–1944.

Kim, S. S., C. Huan, L. Yin, J. S. Xia, D. Candela, and N. S. Sullivan, 2013, "NMR investigation of the low-temperature dynamics of solid ^{4}He doped with ^{3}He impurities," Phys. Rev. B **87**, 224303.

Klein, M. L., and G. K. Horton, 1972, "The rise of self-consistent phonon theory," J. Low Temp. Phys. **9**, 151–166.

Kuklov, A. B., 2019, "Plasticity induced superclimb in solid He-4: Direct and inverse effects," Phys. Rev. B **100**, 014513.

Landau, J., S. G. Lipson, L. M. Määttänen, L. S. Balfour, and D. O. Edwards, 1980, "Interface between Superfluid and Solid ^{4}He," Phys. Rev. Lett. **45**, 31.

Lebyodkin, M. A., T. A. Lebedkina, F. Chmelík, T. T. Lamark, Y. Estrin, C. Fressengeas, and J. Weiss, 2009, "Intrinsic structure of acoustic emission events during jerky flow in an Al alloy," Phys. Rev. B **79**, 174114.

Leggett, Anthony J., 1970, "Can a Solid be 'Superfluid'?," Phys. Rev. Lett. **25**, 1543.

Legrand, Par B., 1984, "Relations between the electronic structure and the ease of glide in hexagonal compact metals," Philos. Mag. B **49**, 171–184.

Lengua, Gabriel A., and John M. Goodkind, 1990, "Elementary excitations and a collective mode in hcp ^{4}He," J. Low Temp. Phys. **79**, 251–287.

Levchenko, A. A., and L. P. Mezhov-Deglin, 1982, "Thermal conductivity of perfect and plastically deformed ^{4}He crystals grown in a narrow bent capillary," Sov. Phys. JETP **55**, 166–174.

Levchenko, A. A., and L. P. Mezhov-Deglin, 1984, "The annealing of freshly induced defects in ^{4}He crystals," Sov. Phys. JETP **59**, 1234–1240.

Lipschultz, F. P., and D. M. Lee, 1965, "Shear Waves in Solid ^{4}He," Phys. Rev. Lett. **14**, 1017.

Lisunov, A., V. Maidanov, N. Mikhin, A. Neoneta, V. Rubanskyi, S. Rubets, E. Rudavskii, and V. Zhuchkov, 2014, "The plastic flow of solid ^{4}He through a porous membrane," J. Low Temp. Phys. **175**, 113–119.

Lisunov, A., V. Maidanov, V. Rubanskyi, S. Rubets, E. Rudavskii, S. Smirnov, and V. Zhuchkov, 2015, "Thermally activated and quantum plasticity of solid ^{3}He at temperatures below 0.5 K," Phys. Rev. B **92**, 140505.

Lisunov, A. A., V. A. Maidanov, V. Yu. Rubanskyi, S. P. Rubets, E. Ya. Rudavskii, and S. N. Smirnov, 2016, "Plastic flow of solid ^{3}He through a porous elastic film," J. Low Temp. Phys. **42**, 1075–1093.

Lücke, K., A. V. Granato, and L. J. Teutonico, 1968, "Thermally assisted unpinning of a dislocation double loop," J. Appl. Phys. **39**, 5181–5191.

Maass, R., and P. M. Derlet, 2018, "Micro-plasticity and recent insights from intermittent and small-scale plasticity," Acta Mater. **143**, 338–363.

Manninen, A. J., J. P. Pekola, G. M. Kira, J. P. Ruutu, A. V. Babkin, H. Alles, and O. V. Lounasmaa, 1992, "First Optical Observations of Superfluid ^{3}He," Phys. Rev. Lett. **69**, 2392–2395.

Manning, M. B., M. J. Moelter, and C. Elbaum, 1986, "Plastic deformation, vacancy diffusion, and vacancy delocalization in bcc ^{3}He," Phys. Rev. B **33**, 1634.

Maris, Humphrey J., 1971, "Interaction of sound waves with thermal phonons in dielectric crystals," in *Physical Acoustics*, Vol. 8, edited by W. P. Mason and R. N. Thurston (Academic Press, New York), pp. 279–345.

Maris, Humphrey J., 2012, "Effect of elasticity on torsional oscillator experiments probing the possible supersolidity of helium," Phys. Rev. B **86**, 020502.

Maris, Humphrey J., and Sebastien Balibar, 2010, "Elastic properties of polycrystalline solid helium," J. Low Temp. Phys. **160**, 5–11.

Maris, Humphrey J., and Sebastien Balibar, 2011, "Effect of helium elasticity on torsional oscillator measurements," J. Low Temp. Phys. **162**, 12–22.

McGreer, K., and J. P. Franck, 1990, "Temperature dependence of elastic constants: A material-independent parameter and data in hcp ^{4}He," Phys. Rev. B **41**, 162.

Mezhov-Deglin, L. P., 1966, "Measurement of the thermal conductivity of crystalline ^{4}He," Sov. Phys. JETP **22**, 47–56.

Miura, Y., K. Mori, and T. Mamiya, 2000, "Dislocation damping in bcc solid ^{3}He at small strain amplitude," Physica (Amsterdam) **284B–288B**, 357–358.

Miura, Y., K. Ogawa, K. Mori, and T. Mamiya, 2000, "Pinning mechanism of the dislocation lines in bcc solid ^{3}He," J. Low Temp. Phys. **121**, 689–693.

Miura, Yuichi, Tetsumasa Nakayasu, Takayoshi Mamiya, and Hideharu Kato, 1998, "Dislocation motion in bcc solid ^{3}He," J. Low Temp. Phys. **110**, 115–119.

Molz, Eric B., and John R. Beamish, 1995, "Freezing and melting of helium in different porous media," J. Low Temp. Phys. **101**, 1055–1077.

Mukharsky, Y., and A. Penzev, 2012, "Elastic and acoustic measurements in solid ^{4}He," J. Low Temp. Phys. **169**, 197–207.

Mukharsky, Yu., A. Penzev, and E. Varoquaux, 2009, "Low-frequency acoustics in solid ^{4}He at low temperature," Phys. Rev. B **80**, 140504.

Mumm, H. P., *et al.*, 2016, "High-sensitivity measurement of ^{3}He-^{4}He isotopic ratios for ultracold neutron experiments," Phys. Rev. C **93**, 065502.

Ninomiya, Toshiyuki, 1974, "Frictional force acting on a dislocation-fluttering mechanism," J. Phys. Soc. Jpn. **36**, 399–405.

Nomura, R., M. Yamaguchi, K. Takaoka, X. Xu, Y. Sasaki, and T. Mizusaki, 2000, "Sound Velocity Measurements of Nuclear-Ordered Solid ^{3}He along the Melting Curve," Phys. Rev. Lett. **85**, 2977–2980.

Nowick, Arthur S., and B. S. Berry, 1972, *Anelastic relaxation in crystalline solids* (Academic Press, New York).

Osborne, D. W., B. M. Abraham, and B. Weinstock, 1951, "Solidification of ^{3}He," Phys. Rev. **82**, 263.

Osborne, D. W., B. Weinstock, and B. Abraham, 1949, "Comparison of flow of isotopically pure liquid ^{3}He and ^{4}He," Phys. Rev. **75**, 988.

Osheroff, D. D., 1992, "Nuclear magnetic order in solid ^{3}He," J. Low Temp. Phys. **87**, 297–342.

Oxburgh, E. R., R. K. O'Nions, and R. I. Hill, 1986, "Helium isotopes in sedimentary basins," Nature (London) **324**, 632.

Paalanen, M. A., D. J. Bishop, and H. W. Dail, 1981, "Dislocation Motion in hcp ^{4}He," Phys. Rev. Lett. **46**, 664.

Pantalei, Claudia, Xavier Rojas, David O. Edwards, Humphrey J. Maris, and Sébastien Balibar, 2010, "How to prepare an ideal helium 4 crystal," J. Low Temp. Phys. **159**, 452–461.

Pelleg, O., M. Shay, S. G. Lipson, E. Polturak, J. Bossy, J. C. Marmeggi, K. Horibe, E. Farhi, and A. Stunault, 2006, "Observation of macroscopic structural fluctuations in bcc solid ^{4}He," Phys. Rev. B **73**, 024301.

Pessoa, Renato, M. de Koning, and S. A. Vitiello, 2012, "Elastic constants and supersolidity in solid hcp ^{4}He," arXiv:1203.0456.

Poirier, Jean-Paul, 1985, *Creep of Crystals: High-Temperature Deformation Processes in Metals, Ceramics and Minerals* (Cambridge University Press, Cambridge, England).

Pollet, L., M. Boninsegni, A. B. Kuklov, N. V. Prokofev, B. V. Svistunov, and M. Troyer, 2007, "Superfluidity of Grain Boundaries in Solid ^{4}He," Phys. Rev. Lett. **98**, 135301.

Pollet, L., M. Boninsegni, A. B. Kuklov, N. V. Prokofev, B. V. Svistunov, and M. Troyer, 2008, "Local Stress and Superfluid Properties of Solid ^{4}He," Phys. Rev. Lett. **101**, 097202.

Pollock, E. L., and David M. Ceperley, 1987, "Path-integral computation of superfluid densities," Phys. Rev. B **36**, 8343.

Pratt, E. J., B. Hunt, V. Gadagkar, M. Yamashita, M. J. Graf, A. V. Balatsky, and J. C. Davis, 2011, "Interplay of rotational, relaxational, and shear dynamics in solid ^{4}He," Science **332**, 821–824.

Prokofev, Nikolay, and Boris Svistunov, 2005, "Supersolid State of Matter," Phys. Rev. Lett. **94**, 155302.

Ramesh, S., Q. Zhang, G. Torzo, and J. D. Maynard, 1984, "Experimental Observation of the Increase of the Two-Dimensional Critical Temperature in Multilayer Adsorption," Phys. Rev. Lett. **52**, 2375–2378.

Ray, M. W., and R. B. Hallock, 2008, "Observation of Unusual Mass Transport in Solid hcp ^{4}He," Phys. Rev. Lett. **100**, 235301.

Ray, M. W., and R. B. Hallock, 2009, "Observation of mass flux through hcp ^{4}He off the melting curve," J. Phys. Conf. Ser. **150**, 032087.

Reese, R. A, S. K. Sinha, T. O. Brun, and C. R. Tilford, 1971, "Phonon dispersion relations for hcp ^{4}He at a molar volume of 16 cm^3," Phys. Rev. A **3**, 1688.

Reppy, John D., Xiao Mi, Alexander Justin, and Erich J. Mueller, 2012, "Interpreting torsional oscillator measurements: Effect of shear modulus and supersolidity," J. Low Temp. Phys. **168**, 175–193.

Richeton, Thiebaud, Jerome Weiss, and Francois Louchet, 2005, "Dislocation avalanches: Role of temperature, grain size and strain hardening," Acta Mater. **53**, 4463–4471.

Rittner, Ann Sophie C., and John D. Reppy, 2007, "Disorder and the Supersolid State of Solid ^{4}He," Phys. Rev. Lett. **98**, 175302.

Rittner, Ann Sophie C., and John D. Reppy, 2009, "Pressure relaxations in solid helium-4," J. Phys. Conf. Ser. **150**, 032089.

Rojas, Xavier, Ariel Haziot, Victor Bapst, Sébastien Balibar, and Humphrey J. Maris, 2010, "Anomalous Softening of ^{4}He Crystals," Phys. Rev. Lett. **105**, 145302.

Rolley, E., S. Balibar, and F. Gallet, 1986, "The first roughening transition of ^{3}He crystals," Europhys. Lett. **2**, 247.

Rolley, E., S. Balibar, F. Gallet, F. Graner, and C. Guthmann, 1989, "The surface tension of bcc ^{3}He crystals," Europhys. Lett. **8**, 523.

Rolley, E., S. Balibar, C. Guthmann, and P. Nozieres, 1995, "Adsorption of ^{3}He on ^{4}He crystal surfaces," Physica (Amsterdam) **210B**, 397–402.

Rolley, E., C. Guthmann, E. Chevalier, and S. Balibar, 1995, "The static and dynamic properties of vicinal surfaces on helium 4 crystals," J. Low Temp. Phys. **99**, 851–886.

Rolley, Etienne, Sébastien Balibar, and Franćois Graner, 1994, "Growth shape of ^{3}He needle crystals," Phys. Rev. E **49**, 1500.

Rolley, Etienne, Eric Chevalier, Claude Guthmann, and Sébastien Balibar, 1994, "Stepped Surfaces of hcp Helium-4 Crystals," Phys. Rev. Lett. **72**, 872–875.

Rubanskyi, Valentyn, and Robert Hallock, 2019, "Mass flux measurements in solid ^{4}He," in Bull. Am. Phys. Soc. **64**, V06.004.

Ruutu, J. P., P. J. Hakonen, and A. V. Babkin, 1998, "Growth of ^{4}He crystals at mK temperatures," J. Low Temp. Phys. **112**, 117–164.

Ruutu, J. P., P. J. Hakonen, J. S. Penttila, A. V. Babkin, J. P. Saramaki, and E. B. Sonin, 1996, "Evidence of ^{4}He Crystallization via Quantum Tunneling at mK Temperatures," Phys. Rev. Lett. **77**, 2514–2517.

Sakai, Akira, Yasushiro Nishioka, and Hideji Suzuki, 1979, "Plastic flow in bcc ^{3}He," J. Phys. Soc. Jpn. **46**, 881–888.

Sanders, D. J., H. Kwun, A. Hikata, and C Elbaum, 1977, "Plastic Deformation of Free-Standing Crystals of hcp ^{4}He," Phys. Rev. Lett. **39**, 815.

Sanders, D. J., H. Kwun, A. Hikata, and C. Elbaum, 1978, "Plastic Deformation of bcc ^{4}He," Phys. Rev. Lett. **40**, 458.

Sasaki, S., F. Caupin, and S. Balibar, 2008, "Optical observations of disorder in solid helium 4," J. Low Temp. Phys. **153**, 43–76.

Sasaki, Satoshi, Frédéric Caupin, and Sébastien Balibar, 2007, "Wetting Properties of Grain Boundaries in Solid ^{4}He," Phys. Rev. Lett. **99**, 205302.

Schaarwachter, W., and H. Ebener, 1990, "Acoustic emission: A probe into dislocation dynamics in plasticity," Acta Metall. Mater. **38**, 195–205.

Schoffel, P., and M. H. Muser, 2001, "Elastic constants of quantum solids by path integral simulations," Phys. Rev. B **63**, 224108.

Schuch, A. F., E. R. Grilly, and R. L. Mills, 1958, "Structure of the α and β forms of solid ^{3}He," Phys. Rev. **110**, 775.

Shal'nikov, A. I., 1962, "Measurement of the thermal conductivity of crystalline ^{4}He," Sov. Phys. JETP **14**, 753–754.

Shashkov, I. V., M. A. Lebyodkin, and T. A. Lebedkina, 2012, "Multiscale study of acoustic emission during smooth and jerky flow in an AlMg alloy," Acta Mater. **60**, 6842–6850.

Shin, Jaeho, and Moses H. W. Chan, 2019, "Mass transport through dislocation network in solid ^{4}He," Phys. Rev. B **99**, 140502.
Shin, Jaeho, Jaewon Choi, Keiya Shirahama, and Eunseong Kim, 2016, "Simultaneous investigation of shear modulus and torsional resonance of solid ^{4}He," Phys. Rev. B **93**, 214512.
Shin, Jaeho, Duk Y. Kim, Ariel Haziot, and Moses H. W. Chan, 2017, "Superfluidlike Mass Flow through 8 μm Thick Solid ^{4}He Samples," Phys. Rev. Lett. **118**, 235301.
Simmons, R. O., 1994, "Thermal vacancies in quantum solid heliums," J. Phys. Chem. Solids **55**, 895–906.
Souris, F., A. D. Fefferman, A. Haziot, N. Garroum, J. R. Beamish, and S. Balibar, 2015, "Search for dislocation free helium crystals," J. Low Temp. Phys. **178**, 149–161.
Souris, Fabien, Andrew D. Fefferman, Humphrey J. Maris, Vincent Dauvois, Philippe Jean-Baptiste, John R. Beamish, and Sébastien Balibar, 2014, "Movement of dislocations dressed with ^{3}He impurities in ^{4}He crystals," Phys. Rev. B **90**, 180103.
Souris, Fabien, Xavier Rojas, Paul H. Kim, and John P. Davis, 2017, "Ultralow-Dissipation Superfluid Micromechanical Resonator," Phys. Rev. Applied **7**, 044008.
Straty, G. C., and E. D. Adams, 1966a, "^{4}He Melting Curve below 1 K," Phys. Rev. Lett. **17**, 290–292.
Straty, G. C., and E. D. Adams, 1966b, "PVT measurements of the hcp-bcc phase transition in solid ^{3}He," Phys. Rev. **150**, 123.
Suhel, A., and J. R. Beamish, 2011, "Pressure gradients in solid ^{4}He: Thermal quenching and annealing," Phys. Rev. B **84**, 094512.
Suzuki, Hideji, 1973, "Plastic flow in solid helium," J. Phys. Soc. Jpn. **35**, 1472–1479.
Suzuki, Hideji, 1977, "Plastic flow in hcp ^{4}He: II," J. Phys. Soc. Jpn. **42**, 1865–1872.
Suzuki, Taira, Shin Takeuchi, and Hideo Yoshinaga, 2013, *Dislocation Dynamics and Plasticity*, Vol. 12 (Springer Science+Business Media, New York).
Syshchenko, Oleksandr, James Day, and John Beamish, 2010, "Frequency Dependence and Dissipation in the Dynamics of Solid Helium," Phys. Rev. Lett. **104**, 195301.
Takeuchi, Shin, and Ali S. Argon, 1979, "Glide and climb resistance to the motion of an edge dislocation due to dragging a Cottrell atmosphere," Philos. Mag. A **40**, 65–75.
Thomlinson, W., J. Eckert, and G. Shirane, 1978, "Inelastic neutron scattering from high-density fcc ^{4}He," Phys. Rev. B **18**, 1120.
Thompson, D. O., and D. K. Holmes, 1959, "Dislocation contribution to the temperature dependence of the internal friction and Young's modulus of copper," J. Appl. Phys. **30**, 525–541.
Todoshchenko, Igor A., Harry Alles, Heikki J. Junes, Alexander Ya. Parshin, and Viktor Tsepelin, 2005, "Measurements on the surface tension of ^{3}He crystals near 100 mK," J. Low Temp. Phys. **138**, 811–816.
Treiner, J., 1993, "Helium mixtures on weak binding substrates," J. Low Temp. Phys. **92**, 1–9.
Trickey, S. B., W. P. Kirk, and E. D. Adams, 1972, "Thermodynamic, elastic, and magnetic properties of solid helium," Rev. Mod. Phys. **44**, 668.
Tsepelin, Viktor, Harry Alles, A. Babkin, J. P. H. Härme, Reyer Jochemsen, A. Ya. Parshin, and G. Tvalashvili, 2001, "Observation of Higher Order Facets on ^{3}He Crystals," Phys. Rev. Lett. **86**, 1042.
Tsepelin, Viktor, Harry Alles, Alexei Babkin, Reyer Jochemsen, Alexander Ya. Parshin, and Igor A. Todoshchenko, 2002, "Morphology and growth kinetics of ^{3}He crystals below 1 mK," J. Low Temp. Phys. **129**, 489–530.
Tsuruoka, Fujio, and Yosio Hiki, 1979, "Ultrasonic attenuation and dislocation damping in helium crystals," Phys. Rev. B **20**, 2702.
Tsymbalenko, V. L., 1976, "Plastic flow of crystalline ^{4}He," JETP Lett. **23**, 653–656.
Tsymbalenko, V. L., 1977, "Measurements of the yield strength for crystalline," Sov. Phys. JETP **45**, 989–992.
Tsymbalenko, V. L., 1978, "Measurement of internal friction in solid ^{4}He," Sov. Phys. JETP **47**, 787–792.
Tsymbalenko, V. L., 1979, "Effect of plastic deformation and impurities on internal friction in solid ^{4}He," Sov. Phys. JETP **49**, 859–864.
Tsymbalenko, V. L., 1984, "Measurement of the temperature dependence of the shear modulus of solid ^{4}He," Sov. Phys. JETP **60**, 537–541.
Tsymbalenko, V. L., 1986, "Effect of ^{3}He impurities on the internal friction in crystalline ^{4}He," Sov. Phys. JETP **64**, 549–553.
Tsymbalenko, V. L., 1992, "A possible observation of quantum nucleation in superfluid ^{4}He near crystallization," J. Low Temp. Phys. **88**, 55–71.
Tsymbalenko, V. L., 1995, "Study of the growth kinetics of facets in a free-growing ^{4}He crystal," J. Low Temp. Phys. **21**, 120–128.
Vekhov, Ye, and Robert B. Hallock, 2012, "Mass Flux Characteristics in Solid ^{4}He for $T > 100$ mK: Evidence for Bosonic Luttinger-Liquid Behavior," Phys. Rev. Lett. **109**, 045303.
Vekhov, Ye, W. J. Mullin, and Robert B. Hallock, 2014, "Universal Temperature Dependence, Flux Extinction, and the Role of ^{3}He Impurities in Superfluid Mass Transport through Solid ^{4}He," Phys. Rev. Lett. **113**, 035302.
Vignos, James H., and Henry A. Fairbank, 1961, "New Solid Phase in ^{4}He," Phys. Rev. Lett. **6**, 265.
Wagner, Raymond, Stephen C. Steel, Olga A. Andreeva, Reyer Jochemsen, and Giorgio Frossati, 1996, "First Observation of (100) and (211) Facets on ^{3}He Crystals," Phys. Rev. Lett. **76**, 263–266.
Wang, Chia-Lai, and Glenn Agnolet, 1992, "Effects of ^{3}He impurities on the ^{4}He solid-liquid interface," J. Low Temp. Phys. **89**, 759–762.
Wanner, R., 1971, "Elastic constants of bcc ^{3}He from measurements of sound velocity, Debye temperature, and compressibility," Phys. Rev. A **3**, 448.
Wanner, R., I. Iwasa, and S. Wales, 1976, "Evidence for dislocations in solid hcp helium-4 from sound velocity experiments," Solid State Commun. **18**, 853–856.
Wanner, R., K. H. Mueller, and H. A. Fairbank, 1973, "Temperature dependence of the sound velocities and elastic constants of bcc ^{3}He," J. Low Temp. Phys. **13**, 153–173.
Wanner, R., and K. H. Mueller, Jr., 1974, "The temperature dependence of the longitudinal sound velocity in solid ^{4}He," Phys. Lett. **49A**, 209–210.
Weertman, J., 1955, "Theory of steady-state creep based on dislocation climb," J. Appl. Phys. **26**, 1213–1217.
Werthamer, N. R., 1969, "Theory of quantum crystals," Am. J. Phys. **37**, 763–782.
West, Joshua T., Oleksandr Syshchenko, John Beamish, and Moses H. W. Chan, 2009, "Role of shear modulus and statistics in the supersolidity of helium," Nat. Phys. **5**, 598.
Wilks, John, 1967, *The Properties of Liquid and Solid Helium* (Clarendon Press, Oxford).
Wolf, P. E., F. Gallet, S. Balibar, E. Rolley, and Ph Nozieres, 1985, "Crystal growth and crystal curvature near roughening transitions in hcp ^{4}He," J. Phys. (Paris) **46**, 1987–2007.
Zhou, Caizhi, Jung-Jung Su, Matthias J. Graf, Charles Reichhardt, Alexander V. Balatsky, and Irene J. Beyerlein, 2013, "Plastic response of dislocation glide in solid helium under dc strain-rate loading," Phys. Rev. B **88**, 024513.
Zhuchkov, V. A., A. A. Lisunov, V. A. Maidanov, A. S. Neoneta, V. Yu. Rubanskyi, S. P. Rubets, E. Ya. Rudavskii, and S. N. Smirnov, 2015, "Creep in solid ^{4}He at temperatures below 1 K," Low Temp. Phys. **41**, 169–176.